

AD-A138 558

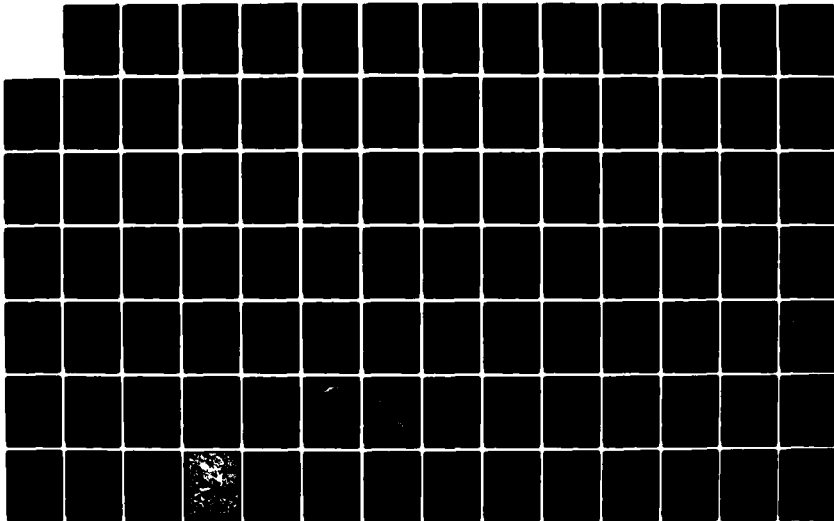
INVESTIGATION OF ICE DYNAMICS IN THE MARGINAL ZONE(U)
MARINE RESEARCH INST HELSINKI (FINLAND)
M LEPPAERANTA ET AL. DEC 83 DAJA45-83-C-0034

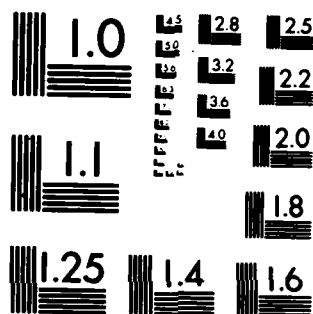
1/2

UNCLASSIFIED

F/G 8/12

NL





MICROCOPY RESOLUTION TEST CHART
NATIONAL BUREAU OF STANDARDS-1963-A

AD

(9)
(10)

INVESTIGATION OF ICE DYNAMICS IN THE MARGINAL ZONE

Final Technical Report
by

Matti Leppäranta
Institute of Marine Research
Helsinki, Finland

and William D. Hibler III
U.S. Army Cold Regions Research
and Engineering Laboratory
Hanover, N.H.

January 1984

United States Army

EUROPEAN RESEARCH OFFICE OF THE U.S. ARMY

London England

CONTRACT NUMBER DAJA45-83-C-0034

Institute of Marine Research

SEARCHED
SERIALIZED
MAR 6 1984
A

Approved for Public Release; distribution unlimited

AD A 138558

DTIC FILE COPY

84 03 06 007

CONTENTS

Report Documentation Page	i
Foreward	1
1. Introduction	2
2. Marginal Ice Zone (MIZ)	4
2.1. General	4
2.2. Summer MIZ in the Fram Strait	10
3. Modeling ice dynamics in the MIZ	13
3.1. System of equations	13
3.2. Free drift	17
3.3. Analytic linear viscous model	21
3.4. General viscous plastic model	27
4. Field study on MIZ ice kinematics	34
4.1. MIZEX-83 experiment in the Greenland Sea	34
4.2. General features of MIZ ice kinematics	37
4.3. Ice velocity fluctuations in the MIZ	42
4.4. Rate of deformation in the MIZ	44
5. Discussion	47
6. Acknowledgements	52
7. References	53
Figures (43)	58



Accession For	
SEA	<input checked="" type="checkbox"/>
TAR	<input type="checkbox"/>
INDEXED	<input type="checkbox"/>
ABSTRACTED	<input type="checkbox"/>
Distribution/	
Availability Codes	
Dist	Avail and/or Special
A-1	.

Unclassified

SECURITY CLASSIFICATION OF THIS PAGE (When Data Entered)

REPORT DOCUMENTATION PAGE		READ INSTRUCTIONS BEFORE COMPLETING FORM
1. REPORT NUMBER	2. GOVT ACCESSION NO. AD-A238558	3. RECIPIENT'S CATALOG NUMBER
4. TITLE (and Subtitle) Investigation of Ice Dynamics in the Marginal Ice Zone		5. TYPE OF REPORT & PERIOD COVERED Final Technical Report Jan 83 - Dec 83
7. AUTHOR(s) Dr. Matti Lepparanta and Dr. William D. Hibler III		6. PERFORMING ORG. REPORT NUMBER
9. PERFORMING ORGANIZATION NAME AND ADDRESS Institute of Marine Research P.O. Box 33 SF-00931 Helsinki, Finland		8. CONTRACT OR GRANT NUMBER(s) DAJA45-83-C-0034
11. CONTROLLING OFFICE NAME AND ADDRESS USARDSG-UK Box 65, FPO NY 09510		10. PROGRAM ELEMENT, PROJECT, TASK AREA & WORK UNIT NUMBERS Reimbursable agreement (ONR-CRREL) #N000148 WRM3005
14. MONITORING AGENCY NAME & ADDRESS (if different from Controlling Office)		12. REPORT DATE Dec 83
		13. NUMBER OF PAGES 102
		15. SECURITY CLASS. (of this report) Unclassified
		15a. DECLASSIFICATION/DOWNGRADING SCHEDULE
16. DISTRIBUTION STATEMENT (of this Report) Approved for public release; distribution unlimited.		
17. DISTRIBUTION STATEMENT (of the abstract entered in Block 20, if different from Report)		
18. SUPPLEMENTARY NOTES		
19. KEY WORDS (Continue on reverse side if necessary and identify by block number) Marginal Ice Zone Kinematics Greenland Sea Models Sea Ice Field observations Dynamics		
20. ABSTRACT (Continue on reverse side if necessary and identify by block number) The dynamics of sea ice in the marginal ice zone (MIZ) are considered both from theoretical and from experimental point of view. Modeling studies are carried through with three types of ice rheologies: free drift, linear viscosity, and plasticity. It is suggested that ice thickness variations may be important to the dispersion of ice edge and lead to e.g. clustering of ice floes. Analytic linear viscous solutions show that variable ice		

Unclassified

SECURITY CLASSIFICATION OF THIS PAGE(When Data Entered)

strength rather than variable forcing is likely to produce sharp changes in ice velocity near the ice edge. Steady state ideal plastic solutions give a constant ice flow under constant forcing in the MIZ. In general, ice interaction has a rectifying effect on the flow pattern. Ice kinematics measurements were made with the Del Norte microwave transponder system in MIZEX-83 Greenland Sea experiment. Differential ice motion was measured with four stations on the ice in the scale of 5 km at three-minute intervals. On several occasions, a rapid slip occurred in measured distances. Ice velocity fluctuations were typically of the order of 1 cm/s and large deformation rates a few per cent per hour. Various spectra of differential ice drift showed a moderate inertial peak and a red noise character at higher frequencies, up to about half-hour period. The maximum rate of shear was about twice as large as divergence from 12-h to about 2-h period.

Unclassified

SECURITY CLASSIFICATION OF THIS PAGE(When Data Entered)

Foreward

The research and development work "Investigation of ice dynamics in the marginal ice zone" was commenced by Dr. Matti Lepparanta on January 24, 1983, at the U.S. Army Cold Regions Research and Engineering Laboratory, Hanover, N.H. The work has been done in cooperation with Dr. William D. Hibler III from USACRREL and consequently this report is co-authored by Dr. Hibler.

This work consists of a theoretical and an experimental part. The former involves dynamic modeling of the iceflow in the marginal sea ice zone and the latter ice kinematics measurements in MIZEX-83 experiment in the Greenland Sea.

1. Introduction

The marginal ice zone (MIZ) is defined as that part of the sea ice cover which is close enough to the open ocean to be affected by its presence (Wadhams, 1980). It is a region of complex atmosphere-ice-ocean interaction extending to 100-200 km from the ice edge. Well-defined MIZ's are typically found in the European sector of the Arctic ice pack (Fig. 1) and along the northern edge of the Antarctic ice cover. The location of the ice margin has a significant role in the world climate system and hence the MIZ has recently become a region of intensive research.

International scientific program called Marginal Ice Zone Experiment (MIZEX) was established in 1981 (Wadhams et al., 1981). Its objective is to understand, in the mesoscale, the physical processes by which ocean, ice and atmosphere interact in the region of the ice edge. The main field effort of the MIZEX program takes place in the Greenland Sea because most of the heat and water exchange between the Arctic Ocean and the rest of the world ocean occurs through Fram Strait, the channel between Greenland and Svalbard (Johannessen et al., 1983a). A summer experiment will be carried through in 1984 and it was preceded by a pilot study in 1983.

A sea ice cover modifies the air-sea energy exchange, penetration of solar radiation into the sea and the salt budget of the upper ocean. Ice dynamics deals directly with the kinetic energy exchange but also affects the thermodynamics indirectly through opening and closing of leads and advection. In turn, freezing and melting change the strength of the ice which determines its resistance to differential motion. Thus dynamics and thermodynamics are coupled. However, on short time-scales sea ice drift can be treated as a purely dynamical problem.

The viscous-plastic sea ice model of Hibler (1979) can simulate the large scale drift of the Arctic ice pack quite

well (Hibler, 1979, 1980b; Hibler and Walsh, 1982) but the model resolution has been too coarse for the characteristic scales in the marginal ice zone. The model has been applied to the East Greenland area on a finer (40 km) scale (Tucker, 1982) and to sea ice in the Bay of Bothnia on a finer scale (18.5 km) yet (Hibler et al., 1983). Although these scales are still a bit coarse for the MIZ, the results indicate that the model works well when its scale goes down. Ice velocities near the ice edge were not well simulated which was considered to be at least partly due to an improper wind field and improper current fields. However, in the MIZ the ice is more fragmented than in the central pack, with substantial variations in compactness, and the validity of the particular viscous-plastic rheology needs to be examined.

In this work the dynamics of the pack ice in the MIZ are considered both from theoretical and experimental point of view. Emphasis is laid on the kinematic properties of ice and on the role of ice interaction. Modeling studies are carried through to examine how various standard-type pack ice rheologies may modify the MIZ flow. Field data on ice kinematics are presented and analyzed. They were obtained in June-July 1983 during the MIZEX Greenland Sea Summer Pilot Study in which both authors participated on Norwegian research vessel Polarbjorn. This experiment is referred to as "MIZEX-83."

2. MARGINAL ICE ZONE (MIZ)

2.1. General

The vicinity of the open ocean gives the marginal ice zone its peculiar properties. Heat is transported to the MIZ from the warm sea through currents, the drift of the ice itself and via the atmosphere. Penetration of swell into the MIZ tends to break ice floes into small pieces. Due to the presence of the open boundary the ice has more freedom of motion than in the central pack. Specifically it is easy to diffuse the ice edge since pack ice has a very small, if any, tensile strength. On the other hand both the atmosphere and the ocean feel a sharp change in their boundary surface at the ice edge from which arise a number of phenomena typical to this region. The characteristic scale of the MIZ width is 100 km which is also representative to atmospheric and oceanic processes at the ice edge.

a. MIZ ice features

Three sub-zones can be distinguished in the MIZ (Bauer and Martin, 1980): edge zone, transition zone and interior zone (Fig. 2). This structure is caused by the gravity waves in the ocean. In the edge zone the ice meets the full wave spectrum and ice blocks may even become piled up on each other. Floes are rectangular and of tens of meters in diameter in the transition zone where waves cause floe breakup and some rafting. Ocean swell can be observed in the interior zone but it has no more the energy to fracture ice floes. Thus waves set up a peculiar floe size distribution in the MIZ although pack ice always does consist of a number of finite separate floes. The division of Bauer and Martin was based on the Bering Sea ice conditions but seems to be generally valid in the qualitative sense.

The mechanism of wave induced ice breakup in the MIZ is explained in Wadhams (1980 and 1984) and Squire (1983). As a normal gravity wave is coupled to an ice sheet it propagates partly as a sinusoidal

flexural-gravity wave in the ice. Fracturing will then occur where the bending stress becomes large enough. Short wavelengths attenuate much more rapidly than the long ones and only the longest ocean swell propagates beyond the edge zone. Finite floes have a rigid-body response to a wave field which relieves the bending stress on a floe, and for a given wave frequency the wave height required to cause fracturing increases as the floe diameter decreases.

The wave-induced breakup would thus tend to produce an increasing floe size with distance from the edge but in reality a discontinuous zone structure is observed. Wadhams (1980) suggested that the disagreement is due to mixing of floes by fluctuating ice motion. He further describes ice margin as a scrapyard which pulverizes any large floes which venture into its sphere of influence. Another significant effect of the ocean waves is that they act to maintain a compact ice edge because diffusion of the edge is opposed by the radiation pressure of the wave field (Wadhams, 1980).

In the MIZ the melting of ice is enhanced. First, there is often a polar front in the ocean near the ice edge and the temperature of the surface water may change by several degrees in a short distance. Eddies develop along the front and transport warm water into the sea beneath the MIZ, and ice may be driven across the front by the eddies or an off-ice wind. Secondly, the presence of a free boundary in the MIZ allows rapid divergence under off-ice forcing. Open patches and leads absorb much more solar radiation than the ice and the heat gain is used to lateral melting of ice floes. This is clearly effective in summer. On the other hand, in winter openings freeze rapidly and thus increase the production of ice. Wadhams et al. (1979) stated that near the ice margin the penetrating swell generates an oscillating shear current at the ice-water interface which further increases the melt rate (when the water temperature is above the freezing point).

The decrease of ice thickness across the MIZ was clearly

shown by Wadhams et al. (1979) (Fig. 3). The mean ice thickness was doubled at the distance of about 100 km from the ice edge. In this particular location the thickness differences are partly due to the difference in ice origin (Wadhams, 1983b). In the Bering Sea MIZ the melt rate may be as high as 1 m per day as the ice drifts across the front (Bauer and Martin, 1980; Josberger, 1983).

Due to the breakup and melting of ice the erosion of deformation features such as pressure ridges is pronounced in the MIZ. The observations of Kozo and Diachok (1973) in the Denmark Strait show a rapid decrease in the frequency and size of ridges across the MIZ (Figs. 4 and 5). They also concluded that the sail height and keel depth distributions are similar and scale by a constant ratio of 1:5 (Fig. 5). As stated by Wadhams (1980) an important consequence of the smoothing of roughness elements is that the form drag coefficients of wind and water become reduced. However, the net effect to ice drift speed is not clear since the free drift velocity is roughly proportional to the ratio of the wind drag coefficient to the water drag coefficient.

Mixing of ice floes is efficient in the MIZ due to the relatively high freedom of motion. As the ice cover opens up, ice floes tend to drift as individuals, and variations in floe form, floe mass and forcing cause large differential velocities. Giant floes and icebergs may enter the MIZ and have a yet unknown effect on the drift pattern.

b. Ice motion in the MIZ

Towards the ice edge the freedom of ice movement increases, and higher magnitude and variability in ice velocity is likely to occur. Due to the presence of the free boundary ice compactness may vary much which means pronounced variations in ice strength since the logarithm of that is proportional to the compactness (Hibler, 1979). In the case of very low strength the ice drift follows the local external forcing. With increasing strength

the drift follows the forcing integral over a scale increasing up to 10^3 km in the Central Arctic.

First a few observed cases are considered. A good illustration of the velocity increase across the MIZ has been presented by Vinje (1977) on the basis of Landsat images (Fig. 6). He gave a wind-driven and an ocean-driven displacement over about two weeks and a general increase over the MIZ is seen in both cases. Johannessen et al. (1983b) showed four cases of daily average MIZ flow where there was a very sharp increase in velocity within about 5 km from the ice edge (Fig. 7). Its cause was uncertain. Lepparanta (1982) gave a daily deformation of the Baltic Sea ice cover and the magnitude increased by a factor of 2 to 3 near the ice edge (Fig. 8). In this case it was seen that the ice pack got more open when approaching the edge.

There are certain features in the MIZ which seem to have a significant influence on its dynamics. They are: 1) Small floe size; 2) Decrease of floe size when approaching the edge; 3) Decrease of ice thickness when approaching the edge; 4) Presence of free boundary; 5) Coupling with atmosphere and ocean which feel a sharp change in their boundary surface; 6) Penetration of ocean swell; 7) Smoothing of roughness elements when approaching the edge. It is a difficult task for the MIZEX-program to try to solve the role of these factors.

Presently a number of qualitative characteristics of the MIZ flow are known and their causes are widely discussed. Hence it is considered important to list and explain them here:

- 1) Edge dispersion. It has been noted often that once the forcing turns off-ice, the ice edge diffuses.
- 2) Banding. It may happen that narrow bands form perpendicular to the wind direction when the wind is off-ice. These bands seem to conserve their form remarkably well. (Zubov, 1945; Martin et al., 1983).
- 3) Edge compaction. For on-ice forcing ice floes drift together and the compactness practically drops from one to zero at the ice edge. This feature is quite frequently noted.

4) Little ridging. It seems that new ridges are not or very seldom formed in the MIZ except for some piling-up of ice blocks due to ocean waves in the edge zone.

5) Ice edge jet. There is some indication that the ice velocity may sharply increase near the ice edge. However, it is not certain what is the main mechanism which may cause the jet. (Johannessen et al., 1983b; Roed and O'Brien, 1981; Lepparanta, 1984; Lepparanta and Hibler, 1984b).

6) Forcing of upwelling at the ice edge. When the surface stress on the ocean is parallel to the ice edge, a discontinuity in it may occur at the edge and cause upwelling. It is an ice dynamics problem to solve whether the discontinuity exists and what is its sign. (Buckley et al., 1979; Clarke, 1978; Roed and O'Brien, 1983).

The first and second points are concerned with a diverging ice edge. The ice offers then little resistance and is more or less a passive tracer of the forcing. Thus these cases are likely to be externally caused. The third and fourth points, on the other hand, are clearly a manifestation of ice interaction. The stress within the MIZ does not get very high because of the free boundary, and the compressive strength of ice prohibits further convergence once the compactness has come close enough to one. The jet is in principle possible due to ice interaction, external forcing or both. Upwelling at the ice edge needs a discontinuity and hence a compact ice edge, which means that the ice interaction then has a significant role in ice motion. It seems likely that the wind stress is greater over the ice than over open water. Due to frictional losses within the ice only a part of the wind stress is transmitted through the ice cover into the ocean. Thus either sign of the ocean forcing discontinuity is possible at the ice edge.

c. MIZ ice rheology

Study of ice rheology is involved with the nature of ice interaction and aims at establishing a law for determining the stress within the ice pack. It can be generally stated that the

ice stress depends on the strain rate and thickness distribution (see, e.g. Hibler, 1979). The dynamical meaning of the rheological law is that it tells how kinetic energy is dissipated and transmitted within the ice. Formally, the divergence of the ice stress appears as a term in the momentum equation.

There are three classical pack ice rheologies: 1) Free drift (Nansen, 1902); 2) Linear viscosity (Laikhtman, 1958; Glen, 1970); 3) Plasticity (Coon et al., 1974; Hibler, 1979). A variation of these cases is a nonlinear viscous model, which is essentially the approach of Hibler (1979). They are illustrated in Fig. 9.

The free drift assumption simply states that there are no stresses within the ice and is valid once the ice pack opens up so that floes do not interact with each other. Such is the case sometimes in summer conditions as has been recently shown by McPhee (1980). Once the ice pack becomes compact the free drift approximation fails since it does not give any resistance to deformation. E.g., an infinite build-up of ice would occur at the coastline during an on-shore wind.

Linear shear viscous rheology was used by Laikhtman (1958) to describe the flow of ice near a fixed boundary and Campbell (1965) could simulate with it the general features of the ice drift in the Arctic Ocean. This original linear model considered only the shear viscosity and Glen (1970) extended it to include the bulk viscosity as well. The linear viscous approach is still being applied to some degree due to its computational easiness. Lepparanta (1981a) has used Glen's extended law in a routine ice forecasting model for the Baltic Sea with some success.

In the 1970s the linear viscous law was highly criticized. The existence of a significant yield strength seemed to be clear and the coastal boundary layer of the ice pack highly nonlinear. The latter feature appears as the well-known shear zone, e.g., off the northern coast of Alaska and Greenland in the Arctic. Additionally, ridging is considered as the dominant dissipation mechanism in the ice (Rothrock, 1975) and in the small scale ridging has a plastic nature (Parmerter and Coon, 1972). Consequently

a plastic rheology was suggested (Coon et al., 1974). Due to mainly computational reasons the plastic ice rheology has been approximated by an elastic-plastic law (Coon et al., 1974) and a viscous plastic law (Hibler, 1979). Both have led to very good results in the Arctic Basin (Hibler, 1979; Pritchard, 1980). An additional important feature of these plastic (or nonlinear viscous) rheologies is that they include a thickness-dependent ice strength and thus describe pack ice as a work-hardening material. This gives a strong restriction to the amount of ice build-up. Hibler (1980b) has got a very good agreement between his model thicknesses and observations.

In the MIZ ice properties and processes have specific characteristic features, and it is not clear which would be a proper rheological model for it. The relevant question is that what is the main dissipation mechanism in the MIZ. Since ridging seems to be ruled out, likely candidates should be friction between floes in contact and floe collisions. This has very interesting implications. In the general theory of flow of granular media the former case is sometimes named slow and the latter rapid flow. It has been shown that the slow granular flow is plastic (e.g., Mandl and Luque, 1970) whereas in the rapid flow the stress depends quadratically on the strain rate (Shen and Ackermann, 1982). The difference between these two laws is illustrated in Fig. 10. It is possible that the MIZ flow may obey either of them depending on the flow characteristics, or even something of mixed type.

2.2 Summer MIZ in the Fram Strait

a. General description

On average at the end of June the coast of Svalbard is open west of 20°E (Fig. 11). The annual variation of the mean monthly position of the ice edge is about 200 km. Short term variation can be comparable to that since a 10m/s-wind may displace

ice by 20 km in a day.

An old description of Koch (1945) says that the ice in the eastern part of the Fram Strait originates from the Eurasian side of the Arctic Ocean and is not very heavy. The western part, on the other hand, contains old and thick ice from the Central and Western Arctic. The idea is based upon assuming a laminar ice outflow from the Arctic Ocean. Satellite images have shown large fluctuations in ice motion which indicates efficient mixing of ice floes but, however, a recent work of Wadhams (1983b) supports Koch's description to some degree.

Wadhams (1983b) presented ice thickness distribution for the Fram Strait showing gradients steeper than 1 m per 100 km (Fig. 12). Our observations at MIZEX-83 drift phase location fit well in his map. In the summer of 1981 Vinje et al. (1983) found heavily ridged ice close to the ice edge but during the proceeding months there had been an unusual east-southeasterly drift of ice north of Fram Strait.

Fram Strait is the main channel of the outflow of ice from the Arctic Ocean. It has been estimated that the average value is about $10^5 \text{ m}^3 \text{ s}^{-1}$ (Vinje, 1976). As the ice leaves the Arctic Ocean it enters the East Greenland current and its speed increases from 6-12 cm/s at 80-81°N to 6-37 cm/s at 76-79°N (Vinje, 1976). The ice velocity tends to increase also across the Fram Strait so that the maximum value occurs at the ice edge (see Fig. 6).

For a more complete discussion of the ice in the northern Greenland Sea the reader is referred to Wadhams (1980), Weeks (1982) and Overgard et al. (1983).

b. Conditions during the MIZEX-83 experiment

In the summer of 1983 the ice conditions seemed to be normal in the northern Greenland Sea (Fig. 13). The present authors participated in the MIZEX-83 experiment on R/V Polarbjorn for carrying through ice kinematics studies. These were done during the so called drift phase, June

28 to July 9, when Polarbjorn was moored to an ice floe in the northern part of the Fram Strait (Fig. 13). However, before the drift phase began the ship sailed in the MIZ for several days in order to deploy instruments on and beneath the ice. Thus notes on the features of the MIZ could be made.

Due to difficulties in navigating in the MIZ Polarbjorn could not go deeper than 20-25 km into the MIZ. The ice edge was usually well defined and the edge zone well developed. The ice was not uniformly distributed but clustering of floes was noted as a typical phenomenon. In places there were open patches and in places closely packed clumps of floes. This is probably important to the initialization of edge dispersion. As an example, visual observations during one transect are illustrated in Fig. 14. During the drift phase Polarbjorn was located at about 20 km from the edge and the ice was there more uniformly distributed with compactness greater than about 0.7.

Ice floes were typically 10 to 100 meters in diameter and there was some average size increase with the distance from the edge. Deeper in the pack large floes appeared. In the drift phase study area the floe size was quite homogeneous, around 50 meters.

The MIZ ice was a mixture of first-year and multi-year ice and the ice thickness ranged from 1 to 4 meters. It seemed that the amount of first-year ice was greater. Quite high, even 3 meters, ice ridge sails were seen. One could definitely say that the ice was much more heavily ridged than reported by Overgaard et al. (1983) for north of Nordaustlandet in the summer of 1980.

On one occasion the efficiency of floe mixing was noted. Two marked ice floes, originally side by side, were found 2 km apart from each other after three days.

3. Modeling ice dynamics in the MIZ

3.1. System of equations

The dynamics of pack ice is governed by the equations of conservation of momentum and mass (e.g. Hibler, 1984):

$$\rho_i \tilde{h} \left[\frac{D\bar{u}}{Dt} + f \hat{k} \times \bar{u} \right] = \nabla \cdot \sigma + \bar{\tau}_w + \bar{\tau}_a + \bar{F}_g, \quad (3.1)$$

$$\frac{DG}{Dt} = -G\nabla \cdot \bar{u} + \psi, \quad (3.2)$$

where ρ_i is the density of ice, \tilde{h} mean ice thickness, D/Dt material time derivative, $\bar{u}=(u,v)$ ice velocity, f Coriolis parameter, \hat{k} the unit vector vertically upward, σ ice stress tensor, $\bar{\tau}_a$ wind stress, $\bar{\tau}_w$ water stress, \bar{F}_g gravitational force due to the sea surface tilt, G ice thickness distribution function and ψ mechanical thickness redistributor. Various forms of Eq.(3.1) have been used for a long time. The continuity equation above was presented by Thorndike et al.(1975); $G(h)$ is the area of ice thinner than h and the function ψ describes the transfer of ice from one thickness category to another due to deformation.

The main ice mechanics problems are to establish a proper formulation for the ice stress and the mechanical redistributor. In general one has

$$\sigma = \sigma(G, \dot{\epsilon}), \quad (3.3)$$

$$\psi = \psi(G, \dot{\epsilon}), \quad (3.4)$$

where $\dot{\epsilon} = 1/2[\nabla\bar{u} + (\nabla\bar{u})^T]$ is the strain rate tensor of the ice. Once explicit expressions are given, the system becomes difficult to solve. Eqs.(3.1-2) are coupled since the ice stress depends on the thickness distribution. Note that there is also a weak coupling even in the absence of ice stress through the appearance of the mean ice thickness in Eq.(3.1).

The forcing terms are expressed as

$$\bar{\tau}_a = \rho_a C_a |\bar{U}_a| \{ \cos \phi \bar{U}_a + \sin \phi \hat{k} \times \bar{U}_a \} , \quad (3.5)$$

$$\bar{\tau}_w = \rho_w C_w |\bar{U}_w - \bar{u}| \{ \cos \theta (\bar{U}_w - \bar{u}) + \sin \theta \hat{k} \times (\bar{U}_w - \bar{u}) \} , \quad (3.6)$$

$$\bar{F}_g = -\rho_i h g \nabla \xi , \quad (3.7)$$

where $\bar{\tau}_a$ and $\bar{\tau}_w$ are the air and water densities, C_a and C_w air and water drag coefficients, \bar{U}_a and \bar{U}_w air and water velocities, ϕ and θ boundary layer turning angles for air and water, g is the gravity acceleration and ξ the dynamic height of the sea surface. In analytic studies it is often convenient to linearize the water stress using the Ekman boundary layer solution modified by the angle of $\pi/4 - \theta$,

$$\bar{\tau}_w = \rho_w \sqrt{\kappa f} \{ \cos \theta (\bar{U}_w - \bar{u}) + \sin \theta \hat{k} \times (\bar{U}_w - \bar{u}) \} , \quad (3.8)$$

where κ is the kinematic eddy viscosity coefficient for water.

When modeling MIZ ice dynamics two meaningful simplifications can be made. First, the MIZ is idealized as a long narrow zone with straight and parallel boundaries (Fig.15), and it is assumed that spatial variations are much larger perpendicular than parallel to the ice edge. Then, aligning the y -axis with the ice edge (Fig.15) we have

$$\frac{\partial}{\partial x} \gg \frac{\partial}{\partial y} . \quad (3.9)$$

This is a similar boundary-layer model to Laikhtman's (1958) and has been applied for the MIZ by Roed and O'Brien (1981) and Leparanta and Hibler (1984b).

Secondly, the thickness distribution can be reduced to two levels: the fraction of open water and the fraction of ice cover represented with one thickness value (in each element). This can be reasoned by the fact that we consider dynamics only and need not worry about the different growth rates of thin ice and thick ice. In addition, the changes in the thickness distribution due to deformation are caused by opening and closing of leads more

than by ridging in the MIZ. The continuity equation in the two-level case can be easily transformed into one for the mean thickness \bar{h} and one for the ice compactness A as has been done by Doronin (1970). Henceforth the tilde is omitted from the notation of mean thickness. The role of the redistributor is now to take care that the conditions $h \geq 0$ and $0 \leq A \leq 1$ are always fulfilled.

Finally, we shall consider time-scales more than one hour or so. The inertial term is known to be small for such conditions and is hence neglected. Then the momentum equation has only one independent variable left. Our MIZ ice dynamics model has now become

$$\frac{\partial}{\partial x}(\sigma_{xx}, \sigma_{xy}) - \rho_i h f k^x \bar{u} + \bar{\tau}_w + \bar{\tau}_a + \bar{F}_g = 0, \quad (3.10)$$

$$\frac{\partial \bar{h}}{\partial t} = -\bar{u} \frac{\partial \bar{h}}{\partial x} - \bar{h} \frac{\partial \bar{u}}{\partial x}, \quad \bar{h} \geq 0, \quad (3.11)$$

$$\frac{\partial A}{\partial t} = -\bar{u} \frac{\partial A}{\partial x} - A \frac{\partial \bar{u}}{\partial x}, \quad 0 \leq A \leq 1. \quad (3.12)$$

Additionally, the assumption (3.9) simplifies the strain rate tensor to the form

$$\dot{\epsilon} = \begin{pmatrix} \frac{\partial \bar{u}}{\partial x} & \frac{1}{2} \frac{\partial \bar{v}}{\partial x} \\ \frac{1}{2} \frac{\partial \bar{v}}{\partial x} & 0 \end{pmatrix}. \quad (3.13)$$

As the initial conditions the distribution of ice compactness and thickness across the MIZ must be specified. The ice edge location, $\ell = \ell(t)$, is initially at $x=0$. The boundary between the MIZ and fast ice (or interior ice) is fixed at $x=L$ and the velocity of ice is there given, $\bar{u} = \bar{u}_L$, i.e. in the case of fast ice $\bar{u}_L = 0$. At the ice edge the ice stress, thickness and compactness vanish. Formally,

$$x=L: \quad \bar{u} = \bar{u}_L, \quad (3.14.a)$$

$$x=\ell: \quad \sigma = 0, \quad h = 0, \quad A = 0. \quad (3.14.b)$$

The use of a fixed boundary is reasonable when there is land or fast ice within a few hundred kilometers from the ice edge as in the Greenland Sea. On the other hand if such is not the case the model represents a two-layer approximation to the MIZ - interior ice system where stress is allowed to occur at the layer boundary. The two-layer structure might be caused by a rapid change in ice characteristics or forcing. An other possibility would be to replace the condition (3.14.a) by an infinite boundary condition.

The no stress condition at the ice edge might be replaced by equating the normal stress to the radiation pressure of the ocean waves. The directional spectrum of the wave field just outside the ice edge is directed towards the ice, and the pressure force per unit length on the ice edge is (Longuet-Higgins, 1977; Wadhams, 1980)

$$F_w = \frac{1}{4} \rho_w g (a^2 - a_r^2 + a_t^2) , \quad (3.15)$$

where a , a_r and a_t are the incident, reflected and transmitted wave amplitudes, respectively. This force varies between zero and $\rho_w g a^2 / 2$.

Let us now write Eq. (3.10) in component form:

$$\begin{aligned} \frac{\partial}{\partial x} \sigma_{xx} + \rho_i h f v - \rho_w C_w |\bar{U}_w - \bar{u}| (\cos \theta u - \sin \theta v) \\ + \rho_w C_w |\bar{U}_w - \bar{u}| (\cos \theta U_w - \sin \theta V_w) + \tau_{ax} + F_{gx} = 0 , \end{aligned} \quad (3.16.a)$$

$$\begin{aligned} \frac{\partial}{\partial x} \sigma_{xy} - \rho_i h f u - \rho_w C_w |\bar{U}_w - \bar{u}| (\cos \theta v + \sin \theta u) \\ + \rho_w C_w |\bar{U}_w - \bar{u}| (\cos \theta V_w + \sin \theta U_w) + \tau_{ay} = 0 . \end{aligned} \quad (3.16.b)$$

Note that the linear form (Eq. 3.8) for the water stress would separate it into independent damping and forcing terms. The solution of Eq. (3.16) is the steady state solution of ice velocity for a given mass distribution and is valid in time scales from one hour up to perhaps a day depending on the con-

ditions in each case. In longer time scales the adjustment between the mass and velocity distribution may significantly modify the flow. To obtain the steady state solution for the adjusted case Eq.(3.16) must be satisfied together with

$$\frac{\partial h}{\partial t} = 0 , \quad \frac{\partial A}{\partial t} = 0 . \quad (3.17)$$

It follows directly from Eqs.(3.11-12) and from the presence of the ice edge that the condition (3.17) is equivalent to

$$u \equiv 0 . \quad (3.18)$$

Thus to solve the adjusted case we only need to delete u-velocity in Eq.(3.16).

The standard parameters for the modeling studies are shown in Table 1. The atmospheric and oceanic parameters correspond to geostrophic motion beyond the layers of frictional influence of the ice. The eddy viscosity coefficient for water has been selected so that the linear and quadratic stress laws coincide at $|\bar{U}_w - \bar{u}| = 10$ cm/s.

Table 1. Standard modeling parameters.

$g = 9.8 \text{ ms}^{-2}$	$C_w = 5.5 \times 10^{-3}$	$C_a = 1.2 \times 10^{-3}$
$f = 1.46 \times 10^{-4} \text{ s}^{-1}$	$\theta = 25^\circ$	$\phi = 25^\circ$
$\rho_i = 910 \text{ kg m}^{-3}$	$\kappa = 21 \text{ cm s}^{-2}$	
$\rho_w = 10^3 \text{ kg m}^{-3}$	$\rho_a = 1.3 \text{ kg m}^{-3}$	

3.2. Free drift

The steady state free drift solution of the momentum equation is quite straightforward. The equation reads as

$$-\rho_i h f \hat{k} \times \bar{u} + \bar{\tau}_a + \bar{\tau}_w + \bar{F}_g = 0 . \quad (3.19)$$

Employing the geostrophic balance in the ocean the tilt term can be expressed as $\bar{F}_g = \rho_i h f \hat{k} \times \bar{U}_w$. Now, it is easy to see (e.g. Hibler, 1984) that the free drift velocity is obtained from

$$-\rho_i h f \hat{k} \times \bar{u}_r + \bar{\tau}_w(\bar{u}_r) + \bar{\tau}_a = 0, \quad (3.20.a)$$

$$\bar{u} = \bar{u}_r + \bar{U}_w, \quad (3.20.b)$$

where \bar{u}_r is the velocity of ice relative to the geostrophic current and the notation $\bar{\tau}_w(\bar{u}_r)$ means that $\bar{u} - \bar{U}_w$ is replaced by \bar{u}_r in the water stress expression.

First we take the linear water stress law (Eq.3.8). Eq.(3.20.a) becomes in matrix form

$$\left\{ \rho_w \sqrt{\kappa f} \begin{pmatrix} \cos \theta & -\sin \theta \\ \sin \theta & \cos \theta \end{pmatrix} + \rho_i h f \begin{pmatrix} 0 & -1 \\ 1 & 0 \end{pmatrix} \right\} \bar{u}_r = \bar{\tau}_a. \quad (3.21)$$

This can be written as

$$\begin{pmatrix} c_1 & 0 \\ 0 & c_1 \end{pmatrix} \begin{pmatrix} \cos \beta_1 & -\sin \beta_1 \\ \sin \beta_1 & \cos \beta_1 \end{pmatrix} \begin{pmatrix} u_r \\ v_r \end{pmatrix} = \quad (3.22)$$

$$\rho_a C_a |\bar{U}_a| \begin{pmatrix} \cos \phi & -\sin \phi \\ \sin \phi & \cos \phi \end{pmatrix} \begin{pmatrix} U_a \\ V_a \end{pmatrix},$$

where

$$\beta_1 = \arccos \left\{ \left[1 + \left(\tan \theta + \frac{\rho_i h f}{\rho_w \sqrt{\kappa f} \cos \theta} \right)^2 \right]^{-1/2} \right\}, \quad (3.23.a)$$

$$c_1 = \rho_w \sqrt{\kappa f} \cos \theta \cos \beta_1. \quad (3.23.b)$$

Through inverting the matrixes on the left hand side of Eq. (3.22) we see that in the linear free drift solution the wind velocity is contracted by $\rho_a C_a |\bar{U}_a| / c_1$ and rotated by $\phi - \beta_1$.

The case of quadratic water stress is more difficult and does not give an explicit solution. Lepparanta (1981b) multiplied

Eq. (3.20.a) scalarly with itself and with \bar{u}_r , which led to a pair of nonlinear equations for the dimensionless speed $|\bar{u}_r|/|\bar{U}_a|$ and the deviations angle between the ice and wind velocities, β . The solution depends on the boundary layer angles and two dimensionless products which were chosen as

$$Na = \left[\frac{\rho_a C_a}{\rho_w C_w} \right]^{1/2}, \quad R = \frac{\rho_i h f}{|\bar{U}_a| \sqrt{\rho_a C_a \rho_w C_w}}. \quad (3.24)$$

Then,

$$|\bar{u}_r|/|\bar{U}_a| = Na \cdot F(R, \theta), \quad (3.25.a)$$

$$\cos(\phi + \beta) = \cos \theta \cdot F^2(R, \theta), \quad (3.25.b)$$

where the function F is defined by

$$F^2 + 2 \sin \theta R F^3 + R^2 F^2 - 1 = 0. \quad (3.26)$$

For a fixed oceanic boundary layer angle θ , F decreases monotonically from 1 to 0 as R goes from zero to infinity (Fig.16). Note that F is only weakly dependent on θ .

The basic qualitative difference between the linear and quadratic cases is in the wind dependency of the solution. The linear case states that the ice speed is proportional to the squared wind speed whereas in the quadratic case ice speed increases only slightly stronger than in direct proportion to the wind speed. The deviation angle depends naturally on the atmospheric boundary layer angle but in the quadratic case it also decreases with increasing wind stress. Both cases give qualitatively similar role to the ice thickness h: as h increases, the ratio of ice speed to wind speed decreases and the deviation angle increases.

The free drift approximation is reasonable when the compactness of ice is less than about 0.8 and it is hence useful for studying the edge dispersion. Even this simple law leaves much freedom to variability of ice motion through forcing, boundary layer parameters and the thickness of ice. Here we concentrate on the last of these factors since its variability is rather well known; e.g.

during MIZEX-83 it was noted that the Greenland Sea MIZ is a mixture of first-year and multiyear ice floes with thicknesses ranging from 1 to 4 m. The basic idea of the thickness effect dates back to Zubov(1945) and has been recently applied for the MIZ by Lepparanta and Hibler (1984a).

The thickness variations may have three dynamically important consequences: 1) Mixing of ice floes as they drift with different speeds; 2) Clustering of floes as light floes catch up with heavy floes in some places and drift apart from them in others; 3) Dispersion as light floes drift fast away from the MIZ. It is anticipated that a variable form drag of floes might lead to qualitatively similar results but it is not known how the form drag varies.

To understand the thickness effect quantitatively some free drift solutions are shown in Fig.17 in vector form. Since 1 cm/s approximately equals 1 km/day it is seen that neighboring first-year and multiyear ice floes can drift apart several kilometers in one day due to the thickness difference only. Such a phenomenon was in fact observed in MIZEX-83. In particular, after several days of off-ice winds, two originally adjacent floes that had been marked were relocated and found to be about 2 km apart.

It is also notable that floe clustering due to differential drift of floes is a substantial conceptual change from the thickness distribution concepts used in most sea-ice models (see e.g. Hibler, 1984). In conventional sea-ice models, one velocity is normally used for a variety of ice thicknesses in a region, and statistical ice thickness variations are then deduced from the gradients of this velocity field. Taking into account differential drift of different floes would require a conceptual reformulation of such theories.

To examine whether in fact such drift variations could create clusters, a Monte Carlo simulation was carried out. The results clearly support our reasoning above (Fig.18). Initially, ice floes were randomly distributed in space with random thicknesses up to 5 m. Only one drift component was simulated. The system works so that when a light floe catches a heavy floe, they stick

together and drift as a group; their mean thickness then determines the drift velocity. Floe clustering is seen for all our ice compactness values. Very similar results were obtained when the floes were initially equally rather than randomly spaced.

There is not yet sufficient data on the drift of various floes to test our theory. It is consequently recommended that field measurement relevant to this problem be made during the MIZEX-84 main experiment.

Zubov (1945) suggested that the thickness variations cause ice bands. This may not be exactly true, but possibly in the initialization of band formation they are important. Floe clustering creates openings and Wadhams (1983b) has suggested that the wave radiation pressure during off-ice winds may form bands if there are openings present near the ice edge.

3.3. Analytic linear viscous model

The steady state momentum equation of pack ice with linear viscous rheology is now applied to the MIZ model. This approach gives a possibility to obtain analytical solutions for certain interesting cases. There has been much speculation on the MIZ ice flow on the basis of the free drift law, and linear models give it a first-order correction which considers ice interaction. In the present cases there is no coupling between ice thickness and strength. Consequently, the adjusted steady state solution makes sense only when the forcing is forced so that u-velocity becomes identically zero. This is a far too specific restriction and hence the adjusted case is not considered. The results of this section are based on a recent paper of Lepparanta (1984).

The linear viscous rheology is expressed as (Glen, 1970)

$$\sigma = 2n\dot{\epsilon} + (\zeta - n)\text{tr}\dot{\epsilon} I, \quad (3.27)$$

where I is the unit tensor, and n and ζ are the shear and bulk viscosities of ice. With zero y-derivatives,

$$\nabla \cdot \sigma = \frac{d}{dx} \left[(\zeta + \eta) \frac{du}{dx}, \eta \frac{dv}{dx} \right]. \quad (3.28)$$

We take the linear water stress formula (Eq.3.8) and denote

$$c_w = \rho_w \sqrt{\kappa f}, \quad (3.29.a)$$

$$\bar{F} = \bar{\tau}_a + c_w (\cos \theta \bar{U}_w + \sin \theta \hat{k} \times \bar{U}_w) + \bar{F}_g, \quad (3.29.a)$$

Utilizing Eqs.(3.28-29), the momentum equation (Eq.3.10) can be written in component form as

$$\frac{d}{dx} \left[(\zeta + \eta) \frac{du}{dx} \right] - c_w \cos \theta u + (c_w \sin \theta + \rho_i h f) v + F_x = 0, \quad (3.30.a)$$

$$\frac{d}{dx} \left[\eta \frac{dv}{dx} \right] - c_w \cos \theta v - (c_w \sin \theta + \rho_i h f) u + F_y = 0. \quad (3.30.b)$$

The boundary conditions are now (from 3.14)

$$x = 0: \quad (\zeta + \eta) \frac{du}{dx} = \eta \frac{dv}{dx} = 0, \quad (3.31.a)$$

$$x = L: \quad u = u_L, \quad v = v_L. \quad (3.31.b)$$

a. General solution with constant viscosities

First, to shorten our notations, Eqs.(3.30.a-b) are divided by the constants $\zeta + \eta$ and η , respectively, and rewritten as

$$\frac{d^2 u}{dx^2} + \alpha_1 u + \nu_1 v + \gamma_1 = 0, \quad (3.32.a)$$

$$\frac{d^2 v}{dx^2} - \alpha_2 v - \nu_2 u + \gamma_2 = 0, \quad (3.32.b)$$

where

$$\begin{aligned}
(\zeta+\eta)\alpha_1 &= \eta\alpha_2 = c_w \cos\theta \quad , \\
(\zeta+\eta)v_1 &= \eta v_2 = c_w \sin\theta + \rho_i hf \quad , \\
(\zeta+\eta)\gamma_1 &= F_x, \quad \eta\gamma_2 = F_y \quad .
\end{aligned}
\tag{3.33}$$

Using the elimination method, Eq. (3.32) can be combined to one for u :

$$\frac{d^4 u}{dx^4} - (\alpha_1 + \alpha_2) \frac{d^2 u}{dx^2} + (\alpha_1 \alpha_2 + v_1 v_2) u - (v_1 \gamma_2 + v_2 \gamma_1) = 0 \quad . \tag{3.34}$$

Once this is solved, v is obtained directly from Eq. (3.32.a).

The characteristic polynomial of Eq. (3.34) has the roots

$$\lambda_{1,2,3,4} = \pm \left\{ \frac{\alpha_1 + \alpha_2}{2} \pm \left[\left(\frac{\alpha_1 - \alpha_2}{2} \right)^2 - v_1 v_2 \right]^{1/2} \right\}^{1/2} \tag{3.35}$$

and thus the solution is

$$u = \sum_{\ell=1}^4 C_\ell \exp(\lambda_\ell x) + u_1 \quad , \tag{3.36}$$

where u_1 is a particular integral of Eq. (3.34) and C_ℓ 's are undetermined constants. Then,

$$v = v_1^{-1} \left\{ \sum_{\ell=1}^4 (\alpha_1 - \lambda_\ell^2) C_\ell \exp(\lambda_\ell x) + \alpha_1 u_1 - \frac{d^2 u}{dx^2} - \gamma_1 \right\}. \tag{3.37}$$

Clearly, the roots λ_ℓ consist of 4 real values when the expression in brackets in Eq. (3.35) is non-negative; this is true when

$$\frac{1}{2} \frac{e}{\sqrt{1+1/e}} \geq \tan\theta + \frac{\rho_i hf}{c_w \cos\theta} \quad , \tag{3.38}$$

where $e = \zeta/\eta$. Otherwise the roots are two complex conjugate pairs. The constants C_ℓ are determined using the boundary conditions. In the general case one has to solve four simultaneous linear equations.

b. Constant viscosity and forcing

Now the free drift solution (see section 3.2)

$$\bar{u}_f = \frac{1}{c_w \cos \theta} \begin{pmatrix} 1 & -v \\ v & 1 \end{pmatrix}^{-1} \bar{F}, \quad (3.39)$$

where $v = \tan \theta + \rho_i h f / c_w \cos \theta$, is clearly a particular integral of Eq. (3.34). Thus

$$u = u_f + \sum_{\ell=1}^4 C_{\ell} \exp(\lambda_{\ell} x), \quad (3.40.a)$$

$$v = v_f + \sum_{\ell=1}^4 \frac{\alpha_{\ell} - \lambda_{\ell}^2}{v_{\ell}} C_{\ell} \exp(\lambda_{\ell} x). \quad (3.40.b)$$

Constants C_{ℓ} and the solutions (3.40) were calculated with a computer. The following parameters were held fixed:

$$h = 1.5 \text{ m}, \quad L = 100 \text{ km}, \quad u_L = 0, \quad v_L = 0.$$

Inequality (3.38) is now valid for $e \geq 2.1$. This lies in a realistic range, so both real and complex characteristic roots λ_{ℓ} are possible.

We chose the standard viscosities of $\tau = 2 \cdot 10^9 \text{ kgs}^{-1}$ and $\eta = 10^9 \text{ kgs}^{-1}$. These are one order of magnitude lower than obtained by Hibler and Tucker (1979) for Arctic summer conditions, and one order of magnitude larger than used by Lepparanta (1981a) in an ice forecasting model for the Baltic Sea. The ratio τ/η was taken as the same as the compressive - shear strength ratio in the plastic model of Hibler (1979). The forcing term was set equal to 0.2 Nm^{-2} and directed 30° to the left from the positive y-axis, i.e. 30° off-ice with ice on the right. This choice gives nearly edge-parallel solutions.

The standard case results in v-velocity about 10% less than free drift at the ice edge (Fig.19). Viscosity also slightly changes the direction from free drift and hence u-velocity is very small. In the standard case, $e=2$ and the characteristic roots λ_{ℓ} are complex. Consequently, there is an Ekman-type oscillation present in the solution. This has a small amplitude but still it

can be seen in u-velocity. For comparison, low and high strength cases were solved (Fig.19); they were defined as having one order of magnitude lower and higher viscosities than the standard values (their ratio ϵ was the same).

Removing the bulk viscosity does not change the standard case much because we consider basically an edge-parallel shear flow (Fig.20). The situation would be different if we had an on-ice forcing. With no shear viscosity v-velocity becomes larger than the free drift value and even increases towards the MIZ-interior ice boundary (Fig.20). This is easy to understand when looking at the original equations (3.30): with $\eta = 0$, v needs to satisfy a balance similar to free drift but with less retarding force through u because u is affected by bulk viscosity.

c. Constant viscosity and variable forcing

For simplicity, we neglect now the terms due to the earth's rotation, i.e. we set $\theta = 0$ and $f = 0$. In addition, the forcing is aligned with the ice edge. Then $u \equiv 0$ and v must be solved from

$$\eta \frac{d^2 v}{dx^2} - c_w v + F = 0. \quad (3.41)$$

This has a general solution

$$v = C_1 \exp(\lambda x) + C_2 \exp(-\lambda x) + v_1, \quad (3.42)$$

where C_1 and C_2 are undetermined constants, $\lambda = \sqrt{c_w/\eta}$ and v_1 a particular integral of Eq.(3.41). We take now a quadratic polynomial for F,

$$F = F_0 + F_1 x + F_2 x^2 \quad (3.43)$$

and then

$$v_1 = \frac{1}{c_w} (F_0 + 2F_2 \lambda^{-1} + F_1 x + F_2 x^2). \quad (3.44)$$

Utilizing the boundary conditions the solution becomes

$$v = v_1 - v_1(L) \cdot \frac{\cosh(\lambda x)}{\cosh(\lambda L)} + \frac{F_1}{c_w \lambda} \cdot \frac{\sinh[\lambda(L-x)]}{\cosh(\lambda L)} . \quad (3.45)$$

We fixed as earlier $L = 100$ km. For F three cases are considered: $F = F_0(1-x/L)^n$, $n = 0, 1$ and 2 , $F_0 = 0.2 \text{ Nm}^{-2}$.

The free-drift solution is shown in Fig.21c. It illustrates also the form of the forcing term since now free drift equals c_w^{-1} times the local force. A nonzero viscosity smooths the curves especially near the ice edge where the no stress condition must be satisfied (Figs. 21a-b). Let us look at the point where the speed has dropped by 20% from its value at the edge. With quadratic forcing, it is 11 km for $\eta = 0$, 20 km for $\eta = 10^8 \text{ kgs}^{-1}$ and 30 km for $\eta = 10^9 \text{ kgs}^{-1}$. Thus to produce a sharp increase in the velocity near the ice edge in a constant viscosity model, one must have a very sharp increase in forcing.

d. Variable viscosity and constant forcing

As in c., we neglect the earth's rotation and align the forcing with the ice edge. Our equation for v is thus

$$\frac{d}{dx}(\eta \frac{dv}{dx}) - c_w v + F = 0 . \quad (3.46)$$

This can be solved for some specific forms of η only. We take a quadratic function

$$\eta = \eta_L (x/L)^2 , \quad (3.47)$$

where η_L is the viscosity at the MIZ-interior ice boundary. Eq. (3.46) becomes now the Euler equation

$$x^2 \frac{d^2 v}{dx^2} + 2x \frac{dv}{dx} - \frac{c_w L^2}{\eta_L} v + \frac{L^2 F}{\eta_L} = 0 , \quad (3.48)$$

which has a general solution

$$v = C_1 x^{\mu_1} + C_2 x^{\mu_2} + F/c_w , \quad (3.49)$$

where C_1 and C_2 are undetermined constants and

$$\mu_{1,2} = \pm \sqrt{c_w L^2 / \eta_L + 1/4} - 1/2 \quad (3.50)$$

(let μ_1 take the plus sign). Using the boundary conditions we have

$$v = \frac{F}{c_w} \{1 - (x/L)^{\mu_1}\}. \quad (3.51)$$

Three cases are considered: low, standard and high strength, defined by $\eta_L = 10^8, 10^9$ and 10^{10} kgs⁻¹, respectively. The MIZ width L is as earlier (100 km) and $F = 0.2$ Nm⁻².

The curvature of the velocity distribution across the MIZ may have either sign, depending on the magnitude of the limiting viscosity η_L (Fig.22). Since the viscosity and its gradient vanish at the ice edge, the ice velocity there equals the free drift value. In the case of high strength, 20% drop in the velocity is reached at 1.6 km from the ice edge. Thus, sharp jet-like features in ice velocity can be produced by variations in the strength. Several kinds of viscosity distributions are of course possible. However, it seems reasonable to assume, as here, that the viscosity decreases to zero (or a small value) when the ice edge is approached.

3.4. General viscous plastic model

To examine how a plastic ice rheology modifies marginal ice zone dynamics we have carried out a series of simulations using the dynamic part of Hibler's (1979) model. In addition, analytic solutions for the equilibrium plastic adjustment case are constructed. This section is based on a recent paper of Lepparanta and Hibler (1984b); a more complete description will be given in a subsequent paper of theirs. Here we discuss some of the main features of the results.

The viscous plastic rheology of the Hibler model gives linear viscous creep for small strain rates and plastic flow otherwise.

While other shapes could be employed, the yield curve used here is an ellipse in the principal stress space and the plastic flow is determined according to the associated flow rule. The rheology is defined by

$$\sigma = 2\eta\dot{\epsilon} + [(\zeta - \eta)\dot{\epsilon}_I - \frac{1}{2}P] I \quad (3.52)$$

$$P = P^* h \exp[-C(1-A)] , \quad (3.53)$$

$$\zeta = \frac{1}{2} P / \max\{[\dot{\epsilon}_I^2 + \dot{\epsilon}_{II}^2 / e^2]^{1/2}, \dot{\epsilon}_0\} , \quad \eta = \zeta / e^2 . \quad (3.54)$$

Here η and ζ are the shear and bulk viscosities, P is hydrostatic pressure term, and $\dot{\epsilon}_I$ and $\dot{\epsilon}_{II}$ are the strain rate invariants equal to the sum and difference of the principal strain rates. P^* , C , e and $\dot{\epsilon}_0$ are rheological parameters: P^* is the strength constant, C is the reduction constant for opening, $\dot{\epsilon}_0$ is the maximum viscous creep rate, and e is the ratio of compressive to shear strength. Without y -derivatives the strain rate invariants are reduced to $\dot{\epsilon}_I = \partial u / \partial x$, $\dot{\epsilon}_{II} = |\partial \bar{u} / \partial x|$. As a result, the stress state can lie only in a restricted region within or on the yield curve (Fig.23). The momentum equation can now be written as

$$\frac{\partial}{\partial x} \left\{ (\zeta + \eta) \frac{\partial u}{\partial x} - \frac{P}{2} \right\} + \rho_i h f v + \tau_{wx} + \tau_{ax} = 0 , \quad (3.55.a)$$

$$\frac{\partial}{\partial x} \left\{ \eta \frac{\partial v}{\partial x} \right\} - \rho_i h f u + \tau_{wy} + \tau_{ax} = 0 . \quad (3.55.b)$$

The standard rheology parameters for the present calculations are: $P^* = 10^4 \text{ Nm}^{-2}$, $C = 20$, $e = 2$, $\dot{\epsilon}_0 = 2 \cdot 10^{-7} \text{ s}^{-1}$. C and e are the same as in the original model. The constant P^* has been the main tuning parameter of the model and has ranged from $5 \cdot 10^3$ in the original model to $2.75 \cdot 10^4 \text{ Nm}^{-2}$ in a recent work of Hibler and Walsh (1982). Our creep limit $\dot{\epsilon}_0$ is one to two orders of magnitude larger than usually applied.

The numerical scheme and the computer code of the original model (Hibler, 1979, 1980a) has been employed. The grid size is 4 km and the time step half an hour. Initially, the MIZ is 60 km wide, and

the ice cover is compact and 1.5 m thick. The thickness corresponds to a characteristic MIZ value given in Wadhams et al. (1979). At time zero a constant wind starts to blow. Its speed is always 10 m/s, and in different runs its direction varies around the whole circle at 30° spacing. In the following discussion, the direction, noted by ψ_a , is defined as the wind vector direction and is counted counterclockwise from the x-axis. The interior ice is assumed motionless. The geostrophic ocean current has been neglected in our simulations, i.e. the ice is purely wind-driven.

The free drift case is a useful reference solution for considering the importance of ice interaction in ice drift. Here for a 1.5-m ice thickness, the free drift speed is 15.9 cm/s and the direction is 10.6° to the right from the direction of geostrophic wind. As the thickness decreases to zero, free drift becomes aligned with the wind and its speed increases to 16.8 cm/s.

a. Initialization of the MIZ flow

The initial velocity distribution was calculated by solving the momentum equation only. Ice thickness and compactness were therefore equal to their initial values, 1.5 m and 1.0, over the whole MIZ. The results show a plastic slip at the left-hand boundary and a nearly constant ice velocity in the MIZ (Figs. 24-25). In this "nearly constant" flow the ice creeps in a linear viscous manner and the creep limit restricts velocity differences between neighboring grid cells to less than 0.8 mm/s. As an exception, in the case $\psi_a = 330^\circ$ the yield strength is not overcome and the plastic slip is missing.

The results indicate that the free drift solution is a very good approximation if it is directed more than about 45° away from the MIZ. On the other hand, strictly on-ice forcing gives practically no motion at all. Between these two extremes there are wide regions of nearly edge-parallel flows. Comparing with the free drift it is seen that the ice interaction has a rectifying effect on these flows. It is an important feature and is not difficult to distinguish from observations. The reason for this

rectification is that ice has compressive strength. There is a slight asymmetry between northward and southward flow patterns due to the Coriolis and oceanic turning angle effects.

The basic dimensionless parameter in our problem is

$$\gamma^* = \frac{\tau_a L}{P^* h} , \quad (3.56)$$

where L is the MIZ width. First, plastic deformation is possible only for $\gamma^* \geq \gamma$, where γ depends on the mode of deformation at the left-hand boundary and on the yield ellipse elongation e . Second, in plastic flow the effect of ice interaction can be thought of as reducing the wind stress by a factor of $1 - \gamma/\gamma^*$. The values of γ for some specific cases are:

	General	Standard ($e=2$)
uniaxial extension	$\frac{1}{2}(\sqrt{1+e^{-2}} - 1)$	0.06
pure shear	$\frac{1}{2} e^{-1}$	0.25
uniaxial contraction	$\frac{1}{2}(\sqrt{1+e^{-2}} + 1)$	1.06

The present work has $\gamma^* = 0.62$, and we can see from Fig.24 that the $1 - \gamma/\gamma^*$ dependency describes the solution qualitatively well.

b. Adjustment between mass and velocity

As the MIZ flow evolves with time, the motion toward the interior ice must come to a stop. Consequently, the MIZ gets separated from the interior ice, or a strictly edge-parallel flow develops (Fig.26). The critical point seems to be whether the free drift solution is inward or outward.

When separated from the interior ice, the motion of the MIZ is approximately in the free drift state. The velocity is then not exactly a constant but is slightly modified by the Coriolis effect and the hydrostatic pressure term. The variations are less than 2 cm/s, which is about one-tenth of the average speed.

The edge-parallelity is obtained through mutual adjustment

between the ice mass distribution and velocity. On-ice forcing becomes balanced with the pressure gradient within the MIZ. After 48 hours model simulation edge-parallel flows are already well developed and have approximately constant velocities except for the last grid cell (Fig.26). The high edge velocities are partially a numerical artifact due to the fixed grid. One should, however, note that the velocity of the MIZ is generally lower than the free drift velocity. Introducing perturbations at the ice edge would give a free-drifting ice edge and, hence, a sharp increase in ice velocity close to the edge. The form of the compactness profile is very sharp (Fig.27). For along-edge winds, the compactness drops from 0.8 to 0 in 8 km (two grid cells).

We can gain a perspective on the numerical solution by analytically examining the steady state adjustment case. In steady edge-parallel flow, the u-velocity must be identically zero. The continuity equation is then automatically satisfied (see section 3.1) and the momentum equation becomes

$$-\frac{1}{2} \frac{dP}{dx} + \rho_i h f v + \rho_w C_w \sin \theta |v|v + \tau_{ax} = 0, \quad (3.57.a)$$

$$\frac{d}{dx} \left\{ \eta \frac{dv}{dx} \right\} - \rho_w C_w \cos \theta |v|v + \tau_{ay} = 0, \quad (3.57.b)$$

and now

$$\eta = P / \{ 2e^2 \max(\dot{\epsilon}_0, e^{-1} \left| \frac{dv}{dx} \right|) \}. \quad (3.58)$$

Since $P = P(h,A)$, our problem contains three unknowns: ice thickness, compactness and velocity. We have only two equations (3.57). The results, however, depend weakly on the thickness and, hence, we take it as constant in the following considerations.

Without shear strength ice velocity must be constant, with the absolute value $\{ |\tau_{ay}| / \rho_w C_w \cos \theta \}^{1/2}$. For finite shear strength, the ideal plastic case is approached as $\dot{\epsilon}_0 \rightarrow 0$. Then, in plastic deformation

$$\eta \frac{dv}{dx} = \frac{P}{2e} \operatorname{sgn}\left(\frac{dv}{dx}\right) \quad (3.59)$$

and the pressure gradient can be easily eliminated from Eq. (3.57). Then we have a simple quadratic equation for v , and the solution is

$$|v| = \sqrt{\frac{|\tau|}{C_*} + \left(\frac{r}{C_*}\right)^2} - \frac{r}{C_*} \quad , \quad (3.60)$$

where

$$|\tau| = |\tau_{ay}| - e^{-1} |\tau_{ax}| \quad , \quad (3.61.a)$$

$$C_* = \rho_w C_w (\cos\theta \pm e^{-1} \sin\theta) \quad , \quad (3.61.b)$$

$$r = \pm e^{-1} \rho_i h f \quad , \quad (3.61.c)$$

and in \pm pairs, $+$ is for southward flow and $-$ is for northward flow. For a given spatially constant wind stress the solution is constant. Thus plastic slip occurs at the left-hand boundary, and in the MIZ ice velocity is the given constant while the stress state remains indeterminate.

Next, since v is constant, it follows directly from Eq. (3.57.a) that P is linear:

$$P = b(x - L_0) \quad , \quad (3.62)$$

where L_0 is the location of the ice edge after adjustment and

$$b = \tau_{ax} + \rho_w C_w \sin\theta |v|v + \rho_i h f v \quad . \quad (3.63)$$

Naturally, for the solution to be valid b must be positive. Through Eq. (3.53) we can obtain the compactness profile:

$$A = 1 + C_*^{-1} \log\left\{\frac{b}{P_* h} (x - L_0)\right\} \quad . \quad (3.64)$$

This analytic form gives a very sharp profile (Fig.27). For example,

if $b = 0.05 \text{ Nm}^{-2}$ then $A = 0.78$ at 4 km from the edge.

The model calculations at 48 hours agree rather well with the ideal plastic steady state. In some cases the model solution has not yet fully developed to the steady state. The applied creep limit is so small that the results should really approximate well the ideal plastic flow. On the other hand, if the creep limit is increased, linear viscous law is approached. Then the viscosity would be spatially varying and, as shown in section 3.3, it would be possible to obtain sharp changes in ice velocity close to the ice edge.

4. FIELD STUDY ON MIZ ICE KINEMATICS

4.1 MIZEX-83 experiment in the Greenland Sea

The marginal ice zone in the Greenland Sea has been selected as the region of main field effort of the MIZEX-program (Wadhams et al., 1981; Johannessen et al., 1983a). The first experiment took there place in the summer 1983 and was named as "MIZEX Greenland Sea Summer Pilot Study"; here it is briefly called "MIZEX-83." The experiment lasted about two months. Three research vessels were used and remote sensing studies were carried through from satellites and aircraft. Further general information of MIZEX-83 is given in Johannessen et al. (1983a).

The present writers participated in MIZEX-83 during June 9 to July 12 on the Norwegian research vessel Polarbjorn. During the experiment the Arctic sea ice edge lay about zero meridian west of Svalbard and between the latitudes of 80°N and 81°N north of Svalbard (Fig. 13). Oceanographic instruments were first deployed in the Fram Strait and then the research area was selected for the so-called drift phase when our ice kinematics measurements were to be made. During this phase the ship was moored to an ice floe thus drifting with the ice; it began at 0800Z on June 28 and ended at 1200Z on July 8. In the beginning the floe was situated at 81° 03'N 6°E, about 20 km from the ice edge (Fig. 13).

In the presentation that follows time is generally counted as a MIZEX day which has the zero point at 27 June, 00Z. Thus MIZEX day transforms to Julian day by adding 178.

The ice conditions were almost ideal for our study. Ice concentration was seven to nine tenths around the research area and down to the ice edge, with some patchiness close to the edge. Horizontally the ice cover was very uniform and floe diameters were typically around 50 meters. In our measurement scale, 5 km, the pack well resembled a two-dimensional granular

media (Fig. 28). The ice floes were a mixture of first-year and multiyear ice with mean thickness close to 2 m. During the drift phase Polarbjorn drifted about 50 nautical miles northeast which is opposite to the long term mean flow in this region (Fig. 29).

Our ice kinematics measurements were made using the Del Norte microwave trisponder system. It has been used earlier by CRREL scientists off the north coast of Alaska (Tucker et al., 1980), and a similar method has also been used for ice deformation studies in the Baltic Sea (Lepparanta, 1981b). The system determines distances between its stations by measuring the time the microwave signal (frequency about 9.5 GHz) needs to travel. The absolute accuracy is, according to the manufacturer, three meters.

Our system configuration consisted of a master station (two master units), slave station and four remote stations (Fig. 30). The direct distances from the master to the remotes and the range loops master-slave-remote-master were measured. One remote station was located at the same site as the slave station in order to get the baseline (master-slave) length which is needed for triangulation. As can be seen from Fig. 30, the three measurements (d_0 , d_i , s_i) for each remote give their positions in the coordinate system aligned with the baseline and the master station as the origin (the master was located at Polarbjorn). That is, the Del Norte system does not provide information of the location and orientation of our measurement array in the earth coordinate system. The latter was measured less accurately using radar reflectors on the remote sites and the ship's gyrocompass but the former is not so important to us since we are studying differential motion in the ice pack. The location was, however, routinely determined in MIZEX-83 with the ship's satellite navigation system.

Differential motion can be derived from position time series. It was initially planned to make Del Norte measurements

every hour, but once data began to be acquired it became obvious that shorter time intervals would be necessary to resolve all motion occurring. Accordingly the acquisition computer was reprogrammed to automatically acquire data at 3 min intervals. This operational mode was employed throughout the experiment. The orientation was measured initially every two hours but approximately at half-way of the drift phase the interval was changed to one hour.

In terms of the overall field operation there were no major problems and the system operated much better than expected. There are a few short gaps in the data mainly due to delays in changing batteries in the remote stations when the weather was so foggy that the helicopters could not fly. Battery lifetimes were about 4 days, but varied with different types of transponders. Gaps appeared also due to polar bear problems and interference from Motorola radar transponders. After about 5 days one master unit began malfunctioning but fortunately we had a backup for this particular unit and it was replaced.

The stations on the ice were mounted on the top of 3m (remotes) or 4.5 m (slave) long pipes which stood with the help of rigid supports. These tripods, designed at CRREL, turned out to be very good on soft summer ice. The Del Norte system requires a line of sight between the stations where the signal needs to travel. Under normal atmospheric refraction conditions the length of this line in km equals about $4 \cdot \sqrt{H}$, where H is the sum of the heights of the two particular stations in m. However, the shadowing effect of ridges reduces the effective tripod height. We had one minor problem in that the tripod height was a bit low for the initial slave site C. To correct this the slave unit was moved to site D.

Overall the automated nature of the system together with its high accuracy proved most valuable. These features allowed the acquisition of by far the most detailed and temporally dense ice deformation measurements in existence to date. The data is presented in a report of Hibler and Lepparanta (1984).

4.2. General features of MIZ ice kinematics

We are concerned here with two coordinate system, Del Norte and north-east, which are illustrated in Fig. 31. Their orientations differ by the angle of β which is a function of time. Angles are always given here counterclockwise from x-axis. Since kinematic quantities basically deal with changes of positions the accuracy of measuring displacements (but not absolute positions) is the most relevant.

The Del Norte measurement triple (d_0 , d_i , s_i) for a given station (Figs. 30-31) is transformed to Cartesian or polar form through

$$x_i = d_i + (s_i/d_0)[s_i/2 - d_i - d_0] , \quad (4.1.a)$$

$$y_i = \pm \sqrt{d_i^2 - x_i^2} , \quad (4.1.b)$$

$$r_i = d_i , \quad (4.2.a)$$

$$\phi_i = \arccos(x_i/d_i) . \quad (4.2.b)$$

Note that there are two solutions which is clear for symmetric reasons (Fig. 31). Hence the sign of y-coordinate must be known. This causes problems if a station gets close to the x-axis. Then the triangulation error also becomes large and in fact using a radar reflector the ship's radar gives a more accurate position than the Del Norte system when the direction of the site is within 5 degrees from the x-axis.

The displacement accuracy of the Del Norte system was tested in the field on several occasions by repeating the measurements 4-5 times within a few seconds. In such short time the real displacement is expected to be very small. The statistics of these data give the relevant relative position accuracy and the displacement accuracy is then obtained by multiplying the position accuracy by $\sqrt{2}$. The accuracy is here defined as twice the standard deviation. The result was that both the direct distance and the range loop have 1-m accuracy.

This value was then used to generate the accuracy of the Cartesian and polar coordinates through Monte Carlo simulation (Table 2). The site J gives the worst readings because its direction makes the smallest angle with the x-axis.

Table 2. The position accuracy (twice the standard deviation) of the Del Norte Measurements.

<u>Site</u>	<u>D</u>	<u>O</u>	<u>C</u>	<u>J</u>
δx (m)	1	8	8	14
δy (m)	-	10	3	22
δr (m)	1	1	1	1
$\delta \phi$ (deg)	-	0.14	0.11	0.3

Radar reflectors were located on sites O, C and J. For them the Del Norte system measures the angle ϕ whereas the radar gives the angle $\phi + \beta$ (Fig. 31). Thus the average difference between the Del Norte and radar angles is a good estimator of β . Considering that the accuracy of the radar is about one degree, the averaging gives us the north-east orientation of the Del Norte array, β , to an accuracy of 0.5 deg. Again, Monte Carlo simulation was applied to have the accuracies of the Cartesian and polar coordinates in the north-east system (Table 3).

Table 3. The position accuracy (twice the standard deviation) in the north-east coordinate system; Del Norte and ship's radar data combined.

<u>Site</u>	<u>D</u>	<u>O</u>	<u>C</u>	<u>J</u>
δx (m)	6	12	30	31
δy (m)	20	44	22	41
δr (m)	1	1	1	1
$\delta \phi$ (deg)	0.6	0.6	0.6	0.6

The raw data is basically a time-series with slightly varying interval (within a few seconds from three minutes) and with gaps about 10% of the total length. It was first linearly interpolated to an equally spaced 3-minute time series. Then a low-pass symmetric filter with a sharp frequency cutoff designed by Hibler (1972) was applied followed by resampling. Filtering necessitates the loss of n end points from each end if the number of weights is $2n+1$. For the filtered time series below a filter with 241 weights and the transition band of 48 to 60 minutes has been used.

The array configuration at approximately beginning, middle and end of the drift phase is shown in Fig. 32. A major shearing and rotation occurred during the later period. There was an overall convergence through the drift phase consistent with the generally north eastward drift which would tend to push the ice edge back into the main pack (Fig. 29). Note, however, that there are fluctuations on top of this trend. There is some indication that the shearing is greater than the convergence.

The direct distances had large fluctuations in the very beginning and towards the end of the experiment (Fig. 33). The distance to the site D was about one third of the other distances and thus it is seen that the amplitude of the fluctuations scales approximately linearly with length. Fig. 34 shows the filtered area of the triangle OCJ at $\frac{1}{2}$ hr. intervals over the drift phase. The area change shows a rapid opening and closing early in the experiment followed by a gradual convergence and then a major closing-opening-closing cycle during the last several days of the experiment. This last event is accompanied by a major shearing of the triangle (Fig. 32).

The triangle area in Fig. 34 is our best time series of the changes in ice compactness. They are so large over a long period that the local deformation theory based on the first-order derivatives of displacement does not necessarily yield accurate results. The local theory is, however, good when studying the time rate of change of the deformation. Note

that the triangle area is independent of the rotation and thus provided by the Del Norte data only. We can only present changes in ice compactness. Knowing the absolute value at at least one time point would give a reference value with which the scale on the left in Fig. 34 could easily be changed to the compactness values. This should come true when the aircraft remote sensing data gets processed. The minimum and maximum triangle areas are about 26 and 36 km². If the former corresponds to compactness 1, then the latter would correspond to the compactness of 0.72.

With regard to orientation, the baseline rotated about 20 degrees during the drift phase (Fig. 35). This caused a relative motion in the array comparable to the strain motion measured with the Del Norte system. At the distance of 5 km, 20-degree arc is 1.75 km long. Also is shown in Fig. 35 the rotation of Polarbjorn measured with her gyrocompass. The large bump in the day 6 is man-caused because of the necessity to change the ship's mooring. The two rotation curves show similar behaviour but the high frequency fluctuations are much higher for Polarbjorn.

Analysis of finer time scale data shows there are a large variety of significant fluctuations superimposed on the overall trends. Fig. 36 presents a sample of raw measured distances at 3 minute intervals showing fluctuations over half hour intervals. Filtered distances are given in Fig. 37 and large variations on time scales of a few hours are seen. The fluctuations in these figures are undoubtedly related to floe bumping as well as randomness in the forcing fields. However, it is also possible that they are due to more organized floe interactions which manifest themselves as kinematic waves propagating across the array (see Hibler et al., 1983). A simple example of such wave is the propagation of collisions, after pushing in one end, through a series of initially equally separated billiard balls.

An interesting feature in the recordings was that occasionally there was a sudden slip of the order of tens of meters. Probably due to an overshooting phenomenon in ice stress the distance changes rapidly and then remains approximately at a constant level. An example is shown in Fig. 38 where a sample of the distance d_0 has been plotted. In the days 3 and 4 four such slips occurred.

4.3 Velocity fluctuations

In the scale of the triangle the relative velocity fluctuations seemed to be typically of the order of 1 cm/s. E. g., for a one-hour cycle the displacement amplitude is only of the order of 20m and thus a very good measurement accuracy is needed to study high frequency fluctuations. An illustrative example is given in Fig. 39 which shows the stretch speeds (rate of change of distance) for the lines ship-site O and ship-site J. They have been obtained through first central differencing the time series of the interpolated distances and then filtering with our standard low-pass filter (transition band 48 to 60-minute periods). It is seen that fluctuations up to 8 cm/s occur. The total variance of the stretch speed was highest in the site J (Table 4).

Table 4. The variance of stretch speed (cm^2s^{-2}).

<u>Site</u>	<u>D</u>	<u>O</u>	<u>C</u>	<u>J</u>
Variance	0.56	1.95	1.64	5.48

During the days 7 and 8 the Del Norte system had a higher measurement noise due to an unknown reason and this period cannot be used to study frequencies higher than about one cycle per hour. The data is thus split into two parts which correspond to different flow regimes (Fig. 33): the early part (day 3.00 to day 7.25) was relatively quiet whereas large variations occurred during the late part (day 8.5 to day 11.5). First we shall study the high frequency part with these separate records and then go to lower frequencies with combined filtered data.

The method of spectral analysis is used below. The program used follows Hibler and LeSchack (1972). Briefly, the spectral density function $p(\lambda)$ of a discrete real valued time series is the Fourier transform of the covariance sequence

c_n ,

$$p(\lambda) = c_0 + \sum_{n=1}^{\infty} c_n \cos(2\pi\lambda n) , \quad |\lambda| \leq 1/2 \quad (4.3)$$

where λ is the frequency in cycles per time interval. The spectral density was here estimated using the weighted covariance method with Parzen window (e.g. Koopmans, 1974). Our distance measurement error can be considered as white noise for which $p(\lambda) = \sigma^2$, where σ^2 is the noise variance. For the Del Norte system $\sigma^2 \approx (0.5\text{m})^2$ (Table 1). It is easy to see that estimating the stretch speed u_n by central differencing,

$$u_n(t) = [d(t+\Delta t) - d(t-\Delta t)] / (2\Delta t) , \quad (4.4)$$

leads to the so-called "blue noise" spectrum for the stretch speed measurement noise,

$$p_e = 1/2 (\sigma/\Delta t)^2 \{1 - \cos(4\pi\lambda)\} . \quad (4.5)$$

The maximum of p_e occurs at $\lambda=1/4$ and then $p_e = (\sigma/\Delta t)^2$

The spectra of the interpolated 3-minute time series is shown in Fig. 40 together with the measurement noise. The high frequency end falls off together with the noise. The signal equals noise at the point where the measured spectrum is $10 \log_2 \approx 0.3$ above the noise level. In all cases that point is at a frequency higher than 50 cycles per day (about half-hour period). In the frequency band from about 10 to 50 cycles per day the spectral density falls smoothly with no identifiable peak or change in character.

The data was then smoothed with our standard low pass filter and the spectra was calculated for the whole time series record (Fig. 41). There is some indication of a peak near the inertial frequency (2.0 cycles per day at our location) but the inertial motion is not so clearly distinguishable in ice deformation as it is in translatory ice movement (cf. McPhee, 1978; Fig. 29 in this work). The slope of the spectral

density fall-off seems to change at about 12 cycles per day. A possible explanation is that at higher frequencies the randomness of floe-floe interactions determines the spectra whereas at lower frequencies variations in the external forcing fields begin to dominate the variations of ice deformation.

Small scale mechanics of pack ice should be tried to approach from a stochastic point of view. These spectra serve as a good verification data for such studies.

4.4 Rate of deformation in the MIZ

In the length scale covering a number of floes the mechanical behavior of pack ice is commonly approximated with the frame of a two-dimensional continuum. This approach is also used here. Note that the classical pack ice rheologies are based on the continuum approximation. Pack ice has no preferred reference configuration but it has a memory which enters the rheological law through the thickness distribution function (see Eq. 3.3). In the MIZ short term changes in the thickness distribution are essentially those in the compactness which was already discussed in section 4.2. Thus this section considers the rate of deformation, the second independent variable in the rheological law.

The rate of deformation is actually the velocity gradient tensor,

$$\nabla \bar{u} = \begin{pmatrix} \partial u / \partial x & \partial u / \partial y \\ \partial v / \partial x & \partial v / \partial y \end{pmatrix}, \quad (4.6)$$

This is decomposed into symmetric and anti-symmetric parts as

$$\dot{\epsilon} = \begin{pmatrix} \partial u / \partial x & (\partial v / \partial x + \partial u / \partial y) / 2 \\ (\partial v / \partial x + \partial u / \partial y) / 2 & \partial v / \partial y \end{pmatrix}, \quad (4.7.a)$$

$$\dot{\omega} = \begin{pmatrix} 0 & -(\partial v / \partial x - \partial u / \partial y) / 2 \\ (\partial v / \partial x - \partial u / \partial y) / 2 & 0 \end{pmatrix}, \quad (4.7.b)$$

respectively. The tensor $\dot{\epsilon}$ is the strain rate tensor and $\dot{\omega}$ is the vorticity tensor which has only one independent component. Strain rate corresponds to physical deformation, i.e. changes of distances between the particles, whereas vorticity corresponds to rigid body rotation. The former only affects the ice rheology (see Eq. 3.3). Two useful invariants of the strain rate tensor are

$$\dot{\epsilon}_I = \text{trace}(\dot{\epsilon}) \quad , \quad (4.8.a)$$

$$\dot{\epsilon}_{II} = \sqrt{(\dot{\epsilon}_{xx} - \dot{\epsilon}_{yy})^2 + 4\dot{\epsilon}_{xy}^2} \quad . \quad (4.8.b)$$

The first invariant represents the rate of change of area (i.e. the velocity divergence) and the second twice the maximum shear strain rate.

It is easy to understand that the Del Norte array, moving with the material, measures the physical deformation, i.e. strain, exactly. Thus the strain rate invariants can be calculated using the Del Norte data only. The individual components of the strain rate tensor have then no relevance since the data does not tell where the coordinate axes point to. To transform the strain rate tensor to the north-east system and to obtain the vorticity one must combine the Del Norte data with the orientation observations. Such analysis becomes important when studying the coherence between ice kinematics and the velocity fields in the atmosphere and the ocean, and that will be the next step in our work after the present report. Note that the rotation of the baseline (Fig. 35) does not give the vorticity directly since it is also affected by shear.

The Del Norte data consist of very accurate distance measurements and somewhat less accurate angles (Table 2). The natural method to process the strain rate tensor from such data is a certain kind of stretch distribution method used much in glaciology and applied for sea ice by Hibler et al. (1973). The method is based on the equation of the

normal strain rate $\dot{\epsilon}_n$ (i.e. stretch speed divided with the length of the stretching line) in different directions ϕ :

$$\dot{\epsilon}_n(\phi) = \cos^2\phi \dot{\epsilon}_{xx} + 2\sin\phi\cos\phi \dot{\epsilon}_{xy} + \sin^2\phi \dot{\epsilon}_{yy} \quad (4.9)$$

Thus three normal strain rate measurements in known directions give an exact solution for the strain rate components. If additional data exist, the linear regression can be applied.

We used the sites O, C and J to obtain the strain rate tensor since they correspond to the same space scale. The values of $\dot{\epsilon}_n$ were obtained through central differencing the interpolated distances:

$$\dot{\epsilon}_n(t) = [d(t+\Delta t) - d(t-\Delta t)]/[2\Delta t \cdot d(t)] \quad (4.10)$$

and the angles ϕ were obtained as shown in Eq. (4.2b). Then $\dot{\epsilon}_n$ and ϕ were smoothed with our standard low-pass filter and the filtered time series was resampled every half hour. The strain rate tensor was calculated from the smoothed record.

Clearly the maximum shear rate fluctuates with much higher amplitude than the divergence (Fig. 42). In both series there is an order of magnitude difference between the relatively quiet and the more active period. Strain rates of a few percent per hour were typical which is one order of magnitude greater than observed in the Central Arctic (Hibler et al., 1974) or in a compact ice cover in a closed subarctic basin (Lepparanta, 1981b).

Spectral analysis gives a good illustration of the difference in shear and divergence (Fig. 43). The second invariant shows 6-8 times larger variability than the first invariant for frequencies higher than the inertial frequency. During the active period the inertial peak did not appear in the maximum shear rate and low frequency variations were very high.

5. Discussion

In this work the dynamics of sea ice in the marginal ice zone has been considered. Modeling studies have been carried through with various types of ice rheologies and field data on ice kinematics obtained in MIZEX-83 Greenland Sea experiment are presented and analyzed.

It is recognized that the MIZ flow has certain specific features under different conditions: 1) Edge dispersion; 2) Banding; 3) Edge compaction; 4) Little ridging; 5) Ice edge jet; 6) Forcing of upwelling in the ocean near the ice edge. The first and second features occur in connection with diverging ice edge and are not much affected by ice interaction. To understand and model the rest of these phenomena a proper formulation of ice rheology is required. It may be possible that the MIZ has viscous or plastic behaviour depending on the flow conditions.

Ice edge dispersion was studied using the free drift (no ice stress) approximation. The variability of ice thickness, such as in Greenland Sea, was shown to be able to cause quite notable differential drift. In particular, the thickness effect can lead to floe clustering which was found to be typical in the Greenland Sea MIZ in MIZEX-83. This may be an important initialization mechanism to the diffusion of MIZ and banding.

Linear viscous rheology was applied to the MIZ flow. It is considered as a rather crude approximation of ice rheology but, however, it is much more realistic than the free drift and gives an insight into how the ice interaction may modify the velocity distribution. Especially, it is possible to obtain analytical solutions for the MIZ flow for certain interesting cases. With constant viscosity and forcing, ice velocity does not vary much closer than 30-40 km to the ice edge. The velocity at the ice edge was 10% lower than the free drift for our

standard viscosity value. The solution may contain a small Ekman-type spiral. Monotonically varying forcing did not have a large effect because the integral of forcing and not the local force is most significant. (Free drift must follow the local force exactly). On the other hand, variable viscosity may produce quite different forms of the velocity distribution. Especially, a very sharp change near the ice edge is possible.

As a more advanced rheology, Hibler's (1979) viscous plastic model was applied to the MIZ. This model predicts a nearly constant MIZ flow under constant forcing. If the free drift solution is directed toward the open water the MIZ will lose contact with the interior ice and goes to the free drift state. Otherwise there is generally a plastic slip at the boundary and the ice creeps elsewhere. The ice velocity is naturally less than the free drift if the ice compactness is allowed to equilibrate in response to a given wind field. The profile of ice compactness is sharp close to the edge. One overall feature of the model results is that in the absence of wind nothing happens, since with a plastic rheology the ice will not flow unless forced. This is in contrast to Roed and O'Brien's (1981) results where their simple pressure term will cause the ice to flow and undergo geostrophic adjustment in the absence of wind. Results also show that divergence of ice near the ice margin is caused by ice interaction. Hence, divergence of ice cannot be used alone as an argument for the absence of ice interaction.

Recently a considerable discussion has been devoted to the so-called "ice edge jet." Its existence has been indicated by the observations of Johannessen et al. (1983b) but its nature is not known. It is clear that if the MIZ is loose it has no strength and obeys the free drift law; the jet may then be caused by the forcing distribution only. For compact MIZ, the present results show that a jet-like feature can be present as a perturbation in an ideal plastic model or in a linear viscous model with variable viscosity.

For future modeling work, two points are recognized to need a deep consideration: transient cases and stochastic modeling. It is not certain how the velocity distribution of ice behaves during the adjustment process in the viscous plastic model which may take a day or so. Probably this can be solved using a Lagrangian grid only. We are modeling ice flow in a rather small scale where the random component in the velocity is large in reality. Hence, it would be important to know how different rheologies react to stochastic forcing.

It is considered that more data is needed on ice edge dispersion and ice edge jet, a recommendation to the MIZEX-84 experiment. In particular, it would be relatively easy to track the drift of floes of different thicknesses and see if the thickness effect is indeed significant. The nature of the ice edge jet should be shown: is it transient or steady, forced or caused by ice interaction.

Ice kinematics measurements were made with the Del Norte microwave trisponder system in MIZEX-83. The study area (about 30km^2) located northwest of Svalbard about 20km from the edge. Ice compactness was seven to nine tenths around the area and down to the ice edge. Horizontally the ice cover was very uniform. Floe diameters were typically around 50 m and the thickness of ice ranged from 1 to 4 m.

Our system configuration consisted of four stations on the ice around the base, R/V Polarbjorn moored to an ice floe. The Del Norte system measures positions of the station relative to the base and thus can be used to derive differential motion in the ice pack. Our raw data consists of the relative positions at about three-minute intervals. The accuracy of the system is very good. Distances are determined to one-meter accuracy, and the position accuracy is somewhat worse depending on the triangulation angles. The system is the best all weather method available to study small scale (order of kilometers)

ice kinematics.

There was an overall convergence of almost 30% during the measurement period. Towards the end a major shear occurred in the direction of the ice edge and was accompanied by large closing-opening cycles in the area of the measurement array. On several occasions a rapid slip occurred in the distance series probably due to an overshooting phenomenon in ice stress.

In the length scale of about 5 km ice velocity fluctuations are of the order of 1 cm/s. The spectra of velocity fluctuations showed a peak at the inertial frequency but it was not so notable than generally in translatory ice drift. For frequencies higher than the inertial frequency the spectra had a red noise character down to about half-hour period where the measurement noise became nearly as large as the signal. These were the first published high frequency spectra of ice motion and are considered useful for stochastic modeling studies.

The strain rate in the MIZ turned out to be of the order of a few per cent per hour when the ice was active. This is about one order of magnitude greater than is known to be in the Central Arctic. In frequencies higher than the inertial frequency the variance in the maximum shear rate was about twice as large as that in divergence. At lower frequencies the shear rate varied much more than the divergence.

The large deformation rates observed in the ice pack are probably of the same order of magnitude than those in the ocean currents. Thus it is necessary to measure ice deformation very accurately in order to study current fields with instruments attached to ice floes.

It is considered very valuable to carry through ice deformation measurements with the Del Norte system also in the MIZEX-84 Greenland Sea experiment. The configuration used in MIZEX-83 is applicable, but if two more units are available studies could be made for two different length scales. The

field program of MIZEX-84 will last six weeks, and the observations will likely cover a larger variety of processes than in MIZEX-83. In particular, in MIZEX-83 the very active ice deformation period lasted only three days, and it would be useful to obtain more such data.

Overall the present data set represents a unique set of measurements of the deformation field of a series of interacting floes floating in the ocean. Because of the fine temporal resolution, accuracy of the measurements, and coincidence of spatial current measurements, this data should greatly aid in sorting out the physics of marginal ice zone dynamics and kinematics. Such efforts are currently in progress.

6. Acknowledgements

This work was made possible by support from the Office of Naval Research.

The first author of this report is supported by the U.S. Army Research, Development and Standardization Group, U.K., Contract No. DAJA45-83-C-0034, via a reimbursable ONR Grant through the U.S. Army Cold Regions Research and Engineering Laboratory. The first author is permanently positioned at the Institute of Marine Research, Finland, and we want to express our gratitude to the acting director of the Institute, Dr. Pentti Malkki, for his continuous support of this work.

7. References

- Bauer, J. and S. Martin, 1980: Field observations of the Bering Sea ice edge properties during March 1979. Mon.Wea.Rev., 108(12), 2045-2056.
- Buckley, J.R., T. Gammelsrod, A. Johannessen, O.M. Johannessen and L.P. Roed, 1979: Upwelling: oceanic structure at the edge of the Arctic ice pack in winter. Science, 203, 165-167.
- Campbell, W.J., 1965: The wind-driven circulation of ice and water in a polar ocean. J.Geophys.Res., 70(14), 3279-3301.
- Clarke, A.J., 1978: On wind-driven quasi-geostrophic water movements near fast ice edges. Deep Sea Res., 25, 41-51.
- Coon, M.D., G.A. Maykut, R.S. Pritchard, D.A. Rothrock and A.S. Thorndike, 1974: Modeling the pack ice as an elastic-plastic material. AIDJEX Bull., 24, 1-105.
- Doronin, Yu.P., 1970: K metodike rascheta splochnosti i dreifa l'dov (On a method of calculating the compactness and drift of ice floes). Trudy Arkt. Antarkt. Inst., 291, 5-17 (Engl. transl. 1970, AIDJEX Bull. 3, 22-39).
- Glen, J.W., 1970: Thoughts on a viscous model for sea ice. AIDJEX Bull. 2, 18-27.
- Hibler, W.D., III, 1972: Design and maximum error estimation for small error low pass filters. CRREL Res. Rep. 304, 12 p. U.S. Army Cold Regions Research and Engineering Laboratory, Hanover, N.H.
- Hibler, W.D., III, 1979: A dynamic thermodynamic sea ice model. J.Phys.Oceanogr., 9(4), 815-846.
- Hibler, W.D., III, 1980a: Documentation for a two-level dynamic thermodynamic sea ice model. CRREL Special Report 80-8. U.S. Army Cold Regions Research and Engineering Laboratory, Hanover, N.H.
- Hibler, W.D., III, 1980b: Modeling a variable thickness sea ice cover. Mon.Wea.Rev., 108(12), 1943-1973.
- Hibler, W.D., III, 1984: Ice dynamics. In: Untersteiner, N.(ed.), Air-Sea-Ice Interaction, NATO Institute Proceedings, Plenum Press (in press).
- Hibler, W.D., III and M. Lepparanta, 1984: MIZEX 83 mesoscale sea ice dynamics: data report. Manuscript.
- Hibler, W.D., III and L.A. LeSchack, 1972: Power spectrum analysis of undersea and surface sea-ice profiles. J. Glaciol., 11(63), 345-355.
- Hibler, W.D., III and W.B. Tucker III, 1979: Some results from a linear-viscous model of the Arctic ice cover. J.Glaciol., 22(87), 293-304.
- Hibler, W.D., III and J.E. Walsh, 1982: On modeling seasonal and interannual fluctuations of Arctic sea ice. J.Phys.Oceanogr. 12(12), 1514-1523.

- Hibler, W.D., III, W.F. Weeks, S. Ackley, A. Kovacs and W.J. Campbell, 1973: Mesoscale strain measurements on the Beaufort Sea pack ice (AIDJEX 1971). J. Glaciol. 12(65), 187-206.
- Hibler, W.D., III, W.F. Weeks, A. Kovacs and S. Ackley, 1974: Differential sea ice drift. I. Spatial and temporal variations in sea ice deformation. J. Glaciol. 13(69), 437-455.
- Hibler, W.D., III, I. Udin and A. Ullerstig, 1983: On forecasting mesoscale ice dynamics and buildup. Annals of Glaciology, Vol.4 (in press).
- Johannessen, O.M., W.D. Hibler III, P. Wadhams, W.J. Campbell, K. Hasselmann, I. Dyer and M. Dunbar (eds.), 1983a: MIZEX. A mesoscale air-ice-ocean interaction experiments in the Arctic marginal ice zones. II. A science plan for a summer marginal ice zone experiment in the Fram Strait/Greenland Sea: 1984. CRREL Special Report 83-12, 47 p. U.S. Army Cold Regions Research and Engineering Laboratory, Hanover, N.H.
- Johannessen, O.M., J.A. Johannessen, J. Morison, B.I. Farrelly and E.A.S. Svendsen, 1983b: Oceanographic conditions in the marginal ice zone north of Svalbard in early fall 1979 with an emphasis on mesoscale processes. J. Geophys. Res. 88(C5), 2755-2769.
- Josberger, E.G., 1983: Sea ice melting in the marginal ice zone. J. Geophys. Res. 88(C5), 2841-2844.
- Koch, L., 1945: The east Greenland ice. Medd. Groenl. 130(3).
- Koopmans, L.H., 1974. The spectral analysis of time series. 366 p. Academic Press, N.Y.
- Kozo, T.L. and O.I. Diachok, 1973: Spatial variability of topside and bottomside ice roughness and its relevance to underside acoustic reflection loss. AIDJEX Bull. 19, 113-121.
- Laikhtman, D.L., 1958: O vetrovom dreife ledjanykh polei (On the wind-drift of polar ice). Trudy Leningr. Gidromet. Inst., 7, 129-137.
- Lepparanta, M., 1981a: An ice drift model for the Baltic Sea. Tellus 33(6), 583-596.
- Lepparanta, M., 1981b: On the structure and mechanics of pack ice in the Bothnia Bay. Finnish Mar. Res. 248, 3-86.
- Lepparanta, M., 1982: A case study of pack ice displacement and deformation field based on Landsat images. Geophysica 19(1), 23-31.
- Lepparanta, M., 1984: Analytic analysis of linear sea ice models with an ice margin. MIZEX Bull. (in press).
- Lepparanta, M. and W.D. Hibler, III, 1984a: A mechanism for floe clustering in the marginal ice zone. MIZEX Bull. (in press).

- Lepparanta, M. and W.D. Hibler III, 1984b: The role of ice interaction in marginal ice zone dynamics. MIZEX Bull. (in press).
- Longuet-Higgins, M.S., 1977: The mean forces exerted by waves on floating or submerged bodies with applications to sand bars and wave power machines. Proc. R. Soc. Lond., A, 352, 463-480.
- McPhee, M.G., 1978: A simulation of inertial oscillations in drifting pack ice. Dyn. Atmos. Oceans, 2, 107-122.
- McPhee, M.G., 1980: An analysis of pack ice drift in summer. In: Pritchard, R.S. (ed.), Proc. ICSI/AIDJEX Symp. on Sea Ice Processes and Models, p. 62-75. University of Washington.
- McPhee, M.G., 1983: MIZEX 83 ice drift trajectory. Data report prepared aboard R/V Polarbjorn, 10 July 1983. 6 p.
- Mandl, G. and R.F. Luque, 1970: Fully developed plastic shear flow of granular materials. Geotechnique 20(3), 277-307.
- Martin, S., P. Kauffman and C. Parkinson, 1983: The movement and decay of ice edge bands in the winter Bering Sea. J. Geophys. Res. 88(C5), 2863-2872.
- Nansen, F., 1902: The oceanography of the North Polar Basin. Norwegian North Polar Expedition 1893-1896, Scientific Results, 3, 1-427.
- Norsk Meteorologisk Institutt, 1983: Iskart nr. 26/83, den 28. juni 1983. Norwegian Meteorological Institute, Oslo.
- Overgaard, S., P. Wadhams and M. Lepparanta, 1983: Ice properties in the Greenland and Barents Seas in summer. J. Glaciol., 29(101), 142-164.
- Parmeter, R.R. and M.D. Coon, 1972: Model of pressure ridge formation in sea ice. J. Geophys. Res. 77(33), 6565-6575.
- Pritchard, R.S., 1980: A simulation of nearshore winter ice dynamics in the Beaufort Sea. In: Pritchard, R.S. (ed.), Proc. ICSI/AIDJEX Symp. on Sea Ice Processes and Models, p. 49-61. University of Washington.
- Roed, L.P. and J.J. O'Brien, 1981: Geostrophic adjustment in highly dispersive media: An application to the marginal ice zone. Geophys. Astrophys. Fluid. Dyn., 18, 263-278.
- Roed, L.P. and J.J. O'Brien, 1983: A coupled ice-ocean model of upwelling in the marginal ice zone. J. Geophys. Res. 88(C5), 2863-2872.
- Rothrock, D.A., 1975: The energetics of plastic deformation of pack ice by ridging. J. Geophys. Res. 80(33), 4514-4519.
- Shen, H. and N.L. Ackermann, 1982: Constitutive relationships for fluid-solid mixtures. Journal of the Engineering Mechanics Division, ASCE, 108(EM5), 748-763.

- Squire, V., 1983: Numerical simulation of realistic ice floes in ocean waves. Annals of Glaciology, Vol.4 (in press).
- Thorndike, A.S., D.A. Rothrock, G.A. Maykut and R. Colony, 1975: The thickness distribution of sea ice. J. Geophys. Res. 80(33), 4501-4513.
- Tucker, W.B., III, 1982: Application of a numerical sea ice model to the East Greenland area. CRREL Special Report 82-16, 41 p. U.S. Army Cold Regions Research and Engineering Laboratory, Hanover, N.H.
- Tucker, W.B., III, W.F. Weeks, A. Kovacs, and A.J. Gow, 1980: Nearshore ice motion at Prudhoe Bay, Alaska. In: Pritchard, R.S. (ed.), Proc ICSI/AIDJEX Symp. on Sea Ice Processes and Models, p. 261-272. University of Washington.
- Vinje, T.E., 1976: Sea ice conditions in the European sector of the marginal seas of the Arctic. Norsk Polarinstitutt Arbok 1975, p. 163-174.
- Vinje, T.E., 1977: Sea ice studies in the Spitsbergen - Greenland area. Landsat Report E77-10206, US Dept. of Com., NTIS, Springfield, Va.
- Vinje, T.E., 1981: Frequency distribution of sea ice in the Greenland and Barents Seas. Norsk Polarinstitutt Arbok 1980, p. 57-61.
- Vinje, T.E., M. Kristensen and N. Nergaard, 1983: Sea ice investigations in 'Fram Strait' (North Greenland Sea), July-August 1981. Polar Record 21(135), 597-600.
- Wadhams, P., 1980: Ice characteristics in the seasonal sea ice zone. Cold Regions Science and Technology, 2, 37-87.
- Wadhams, P., 1983a: A mechanism for formation of ice edge bands. J. Geophys. Res. 88(C5), 2813-2818.
- Wadhams, P., 1983b: Sea ice thickness distribution in the Fram Strait. Nature, 305, 108-111.
- Wadhams, P., 1984: The seasonal sea ice zone. In: Untersteiner, N. (ed.), Air-Sea-Ice Interaction, NATO Institute Proceedings, Plenum Press (in press).
- Wadhams, P., A.E. Gill and P.F. Linden, 1979: Transects by submarine of the East Greenland Polar Front. Deep Sea Res. 26(12A), 1311-1328.
- Wadhams, P., S. Martin, O.M. Johannessen, W.D. Hibler III and W.J. Campbell (eds.), 1981: MIZEX. A program for mesoscale air-ice-ocean interaction experiments in the Arctic marginal ice zones. I. Research Strategy. CRREL Special Report 81-19, 20 p. U.S. Army Cold Regions Research and Engineering Laboratory, Hanover, N.H.

Weeks, W.F., 1980: Overview. Cold Regions Science and Technology,
2, 1-35.

Weeks, W.F., 1982: Physical properties of the ice cover in the
Greenland Sea. CRREL Special Report 82-28, 27 p. U.S. Army
Cold Regions Research and Engineering Laboratory, Hanover, N.H.

Zubov, N.N., 1945: L'dy Arktiki (Arctic Ice). Izdatel'stvo
Glavsevmorputi, 360 p. Moscow.

Figure 1.

A schematic picture of the marginal ice zone (MIZ) in the North Atlantic on March 14, 1978. The ice edge and fast ice region are based on U.S. Navy ice charts. (Weeks, 1980)

Figure 2.

A schematic diagram of the subzones in the MIZ (Bauer and Martin, 1980).

Figure 3.

The mean and extreme ice draft profiles across East Greenland Polar Front, October 1976. (Wadhams et al., 1979)

Figure 4.

Frequencies of keels and sails from transects across the Denmark Strait. (Kozo and Diachok, 1973)

Figure 5.

Distributions of sail height and keel depth across the Denmark Strait. (Kozo and Diachok, 1973)

Figure 6.

Ice drift in the Fram Strait based on Landsat images: (a) 21 April-7May 1976, northerly wind 5-15 m/s for most of the period; (b) 5-16 May and 1-12 June 1976, mostly calm weather. (Vinje, 1977)

Figure 7.

Daily average ice drift and surface current from ARGOS buoys, north of Svelbard, 1979. (Johannessen et al., 1983b)

Figure 8.

Daily strain of the ice cover in the northern Baltic Sea based on LANDSAT images. (Lepparanta, 1982)

Figure 9.

A schematic illustration of the three classical pack ice rheologies.

Figure 10.

A schematic illustration of the rheology of granular materials.

Figure 11.

Frequency (in tenths) of sea ice concentration above 4/10 at the end of June, 1971-1980. (Vinje, 1981)

Figure 12.

A contoured map of the mean ice draft in Fram Strait 22 April - 4 May, 1979. (Wadhams, 1983b)

Figure 13.

Ice conditions in the beginning of the drift phase of MIZEX-83 (Norsk Meteorologisk Institutt, 1983). The location of R/V Polarbjorn is shown by ■.

Figure 14.

Visual observations of the MIZ ice during one transect in MIZEX-83.

Figure 15.

The idealized MIZ for modeling studies.

Figure 16.

The function F in the free drift solution for quadratic water stress.

Figure 17.

Free drift solutions for a quadratic water stress: wind stress is aligned with the y -axis and the dots mark the tips of the ice drift vectors; ice thickness = 0, 1, 2, 4, 8, and 16m and wind speed = 5 and 10 m/s.

Figure 18.

Monte Carlo simulation of floe clustering. In each case the lines follow each other, forming a single long line. Each digit gives the thickness of an ice floe rounded in meters. The total time is 100 minutes times the floe size in meters. A uniform wind of 10 m/s was assumed.

Figure 19.

Standard, low strength and high strength solutions for constant viscosity and forcing. The symbols \blacktriangleleft on the right show free-drift values.

Figure 20.

Solutions with no shear viscosity and with no bulk viscosity compared with the standard case. Viscosity and forcing are constant. The symbols \blacktriangleleft on the right show free-drift values.

Figure 21.

Constant viscosity and variable forcing cases: (a) standard ($\eta = 10^9 \text{ kgs}^{-1}$), (b) low strength ($\eta = 10^8 \text{ kgs}^{-1}$), and (c) free drift. The symbols \blacktriangleleft on the right show free-drift values at the ice edge. The free drift case also illustrates the form of the forcing term.

Figure 22.

Variable viscosity cases. The symbol \blacktriangleleft shows free-drift value.

Figure 23.

The yield ellipse. Thick lines indicate the possible stress states in the MIZ model.

Figure 24.

The initial MIZ flow in the viscous plastic model. The degree-numbers on the right give the direction of the geostrophic wind.

Figure 25.

The stress state for the initial MIZ flow. The open circles show the stress at the left-hand boundary and the line - - - - gives the stress through the MIZ for 300°-wind case.

Figure 26.

The MIZ flow after 48 hours in the viscous plastic model. The degree-numbers in the right give the direction of the geostrophic wind.

Figure 27.

The compactness profile after 48 hours. The line - - - - gives the ideal analytic profile for along edge wind; the shape but not location is relevant.

Figure 28.

Photograph of ice floes near the center of the Del Norte array. The location of Polarbjorn is noted, which for scale is 50 m long. This photograph was taken by Dr. Vernon Squire (Scott Polar Research Institute, Cambridge, England) as a part of ice photography survey carried out by helicopters.

Figure 29.

The path of Polarbjorn during the drift phase; the numbers refer to Julian day (McPhee, 1983).

Figure 30.

Del Norte stations in MIZEX-83. The site names and measured quantities are indicated.

Figure 31.

Del Norte (x, y) and north-east (x_n , y_n) coordinate systems. The sites are also indicated.

Figure 32.

The array configuration at approximately beginning, middle and end of the experiment.

Figure 33.

Filtered (low-pass, transition band 48 to 60 minute periods) direct distances to the Del Norte sites.

Figure 34.

Filtered (low pass, transition band 48 to 60 minute periods) area of the triangle OCJ.

Figure 35.

Direction of the baseline and the ship's heading.

Figure 36.

Variation of raw measured distances to Del Norte sites at 3-minute intervals in early part of experiment. The absolute distance values at the beginning of the sample are indicated on the left.

Figure 37.

Variation of filtered (low pass, transition band 48 to 60-minute periods) distances to Del Norte sites in the late part of the experiment. The absolute values at the beginning of the sample are indicated on the left.

Figure 38.

Raw measured distance to the site D during day 2.00 to day 6.00.

Figure 39.

Rate of change of distance between Polarbjorn and site O (a) and J(b) during 30 hours in the late part of the experiment. The time series has been filtered with a low pass filter (transition band 48 to 60 minutes).

Figure 40.

The high frequency spectra of the rate of change of distance between Polarbjorn and (a) site D, (b) site O, (c) site C, and (d) site J. The measurement noise is also shown.

Figure 41.

The spectra of the rate of change of distance between Polarbjorn and sites D, C and J.

Figure 42.

The strain rate invariants in the Del Norte array estimated from filtered data (low pass, transition band 48 to 60-minute periods): a) divergence, b) twice maximum shear rate.

Figure 43.

The spectra of the strain rate invariants in the Del Norte array.

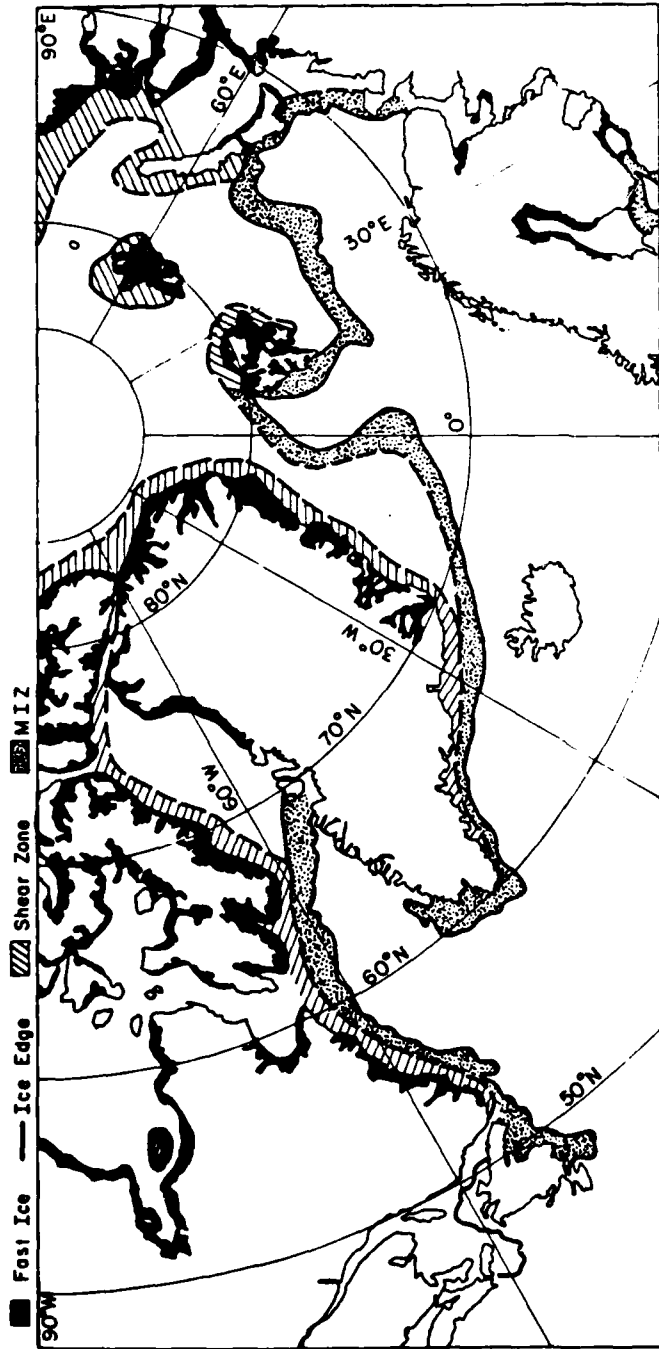


FIG. 1.

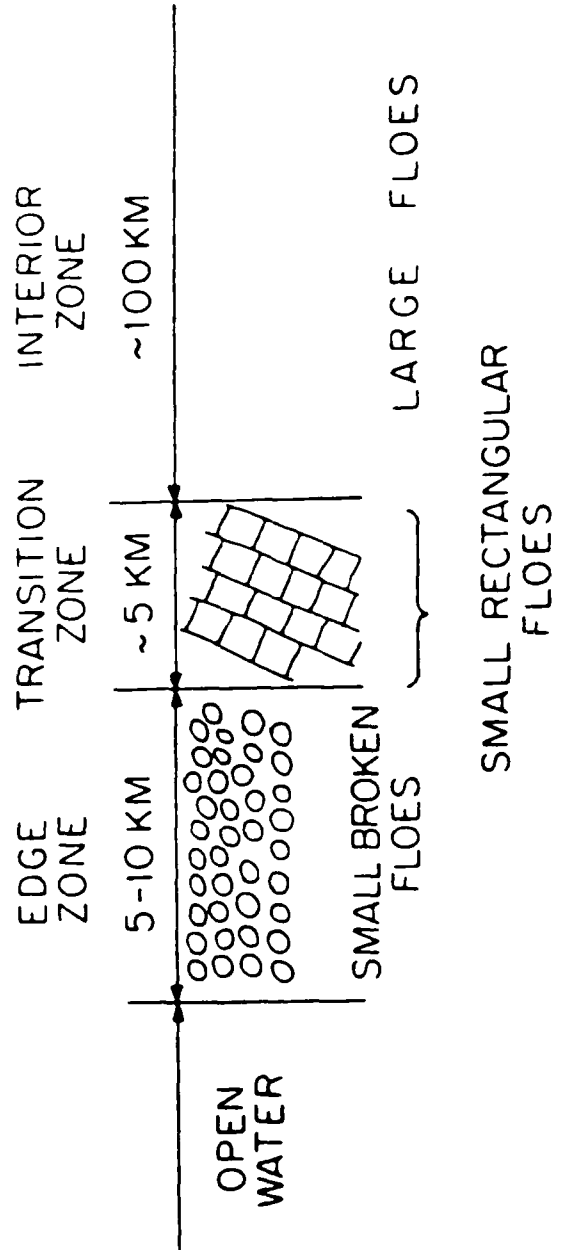


FIG. 2.

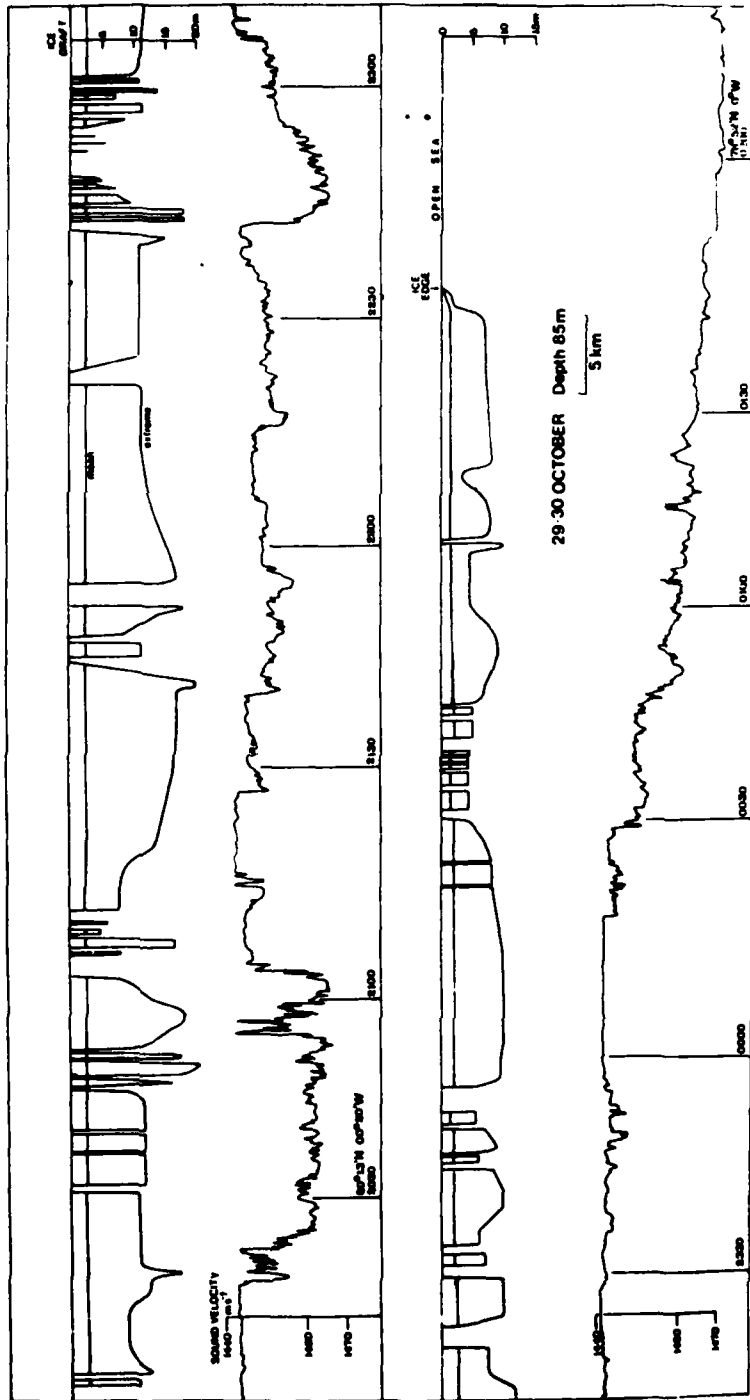


FIG. 3.

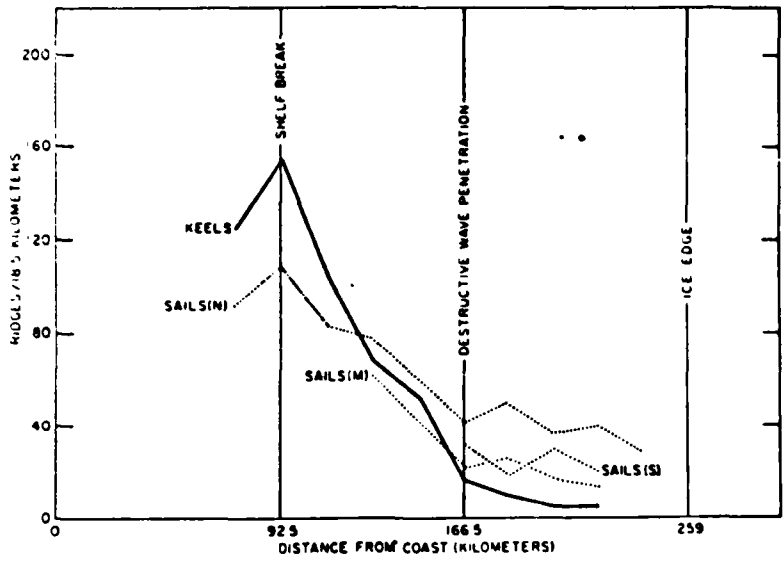


FIG. 4.

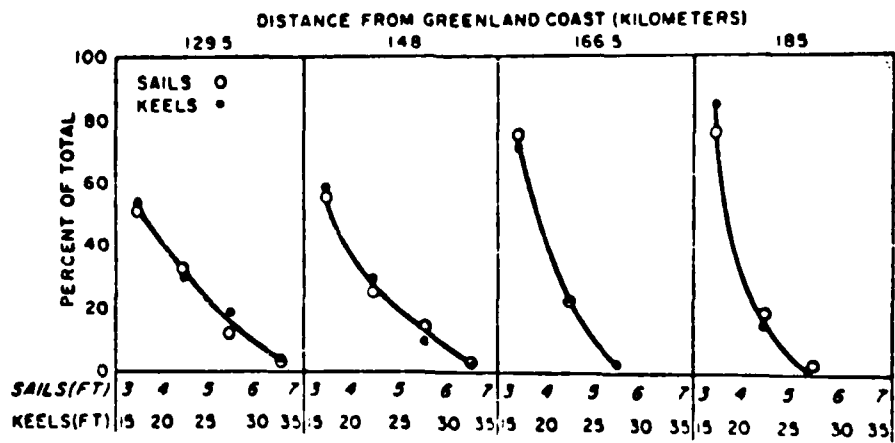


FIG. 5.

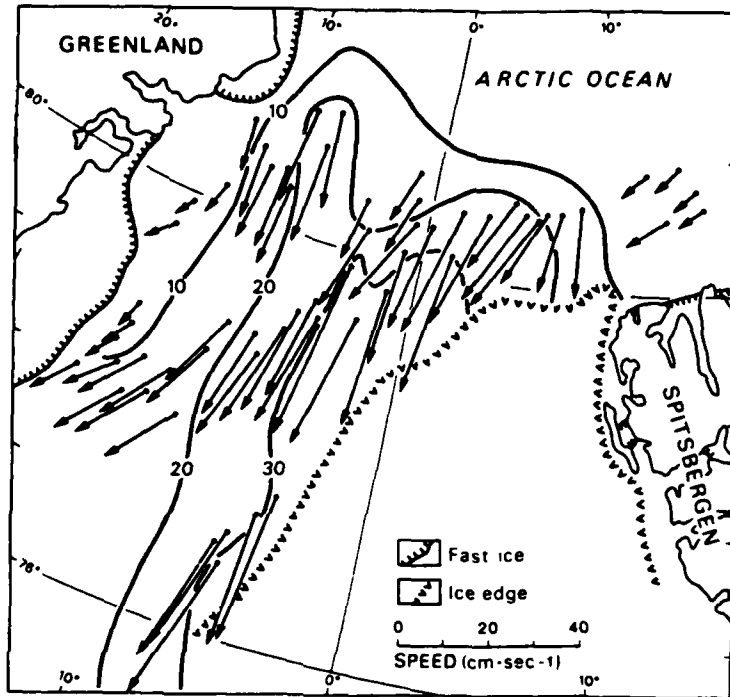


FIG. 6.a)

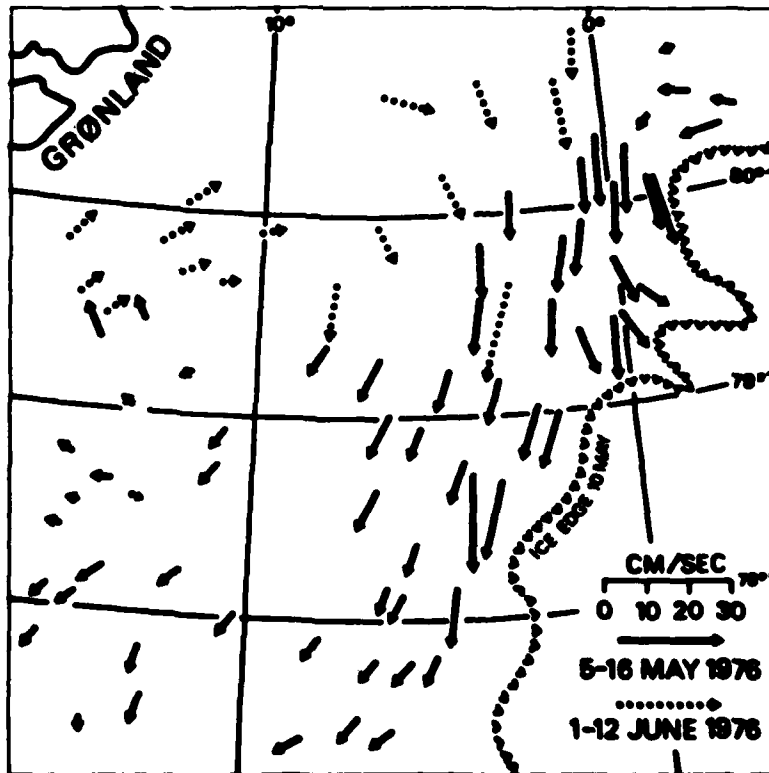


FIG 6.b)

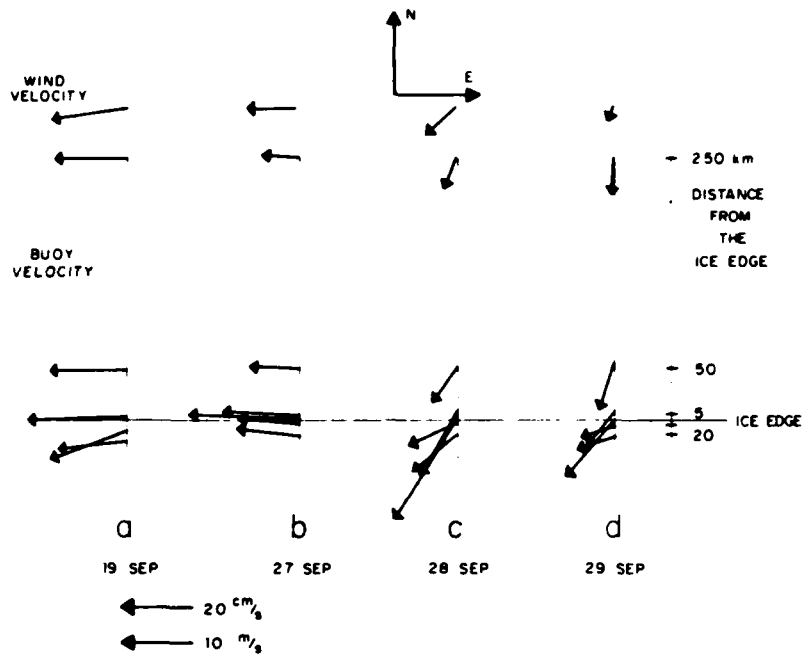


FIG. 7.

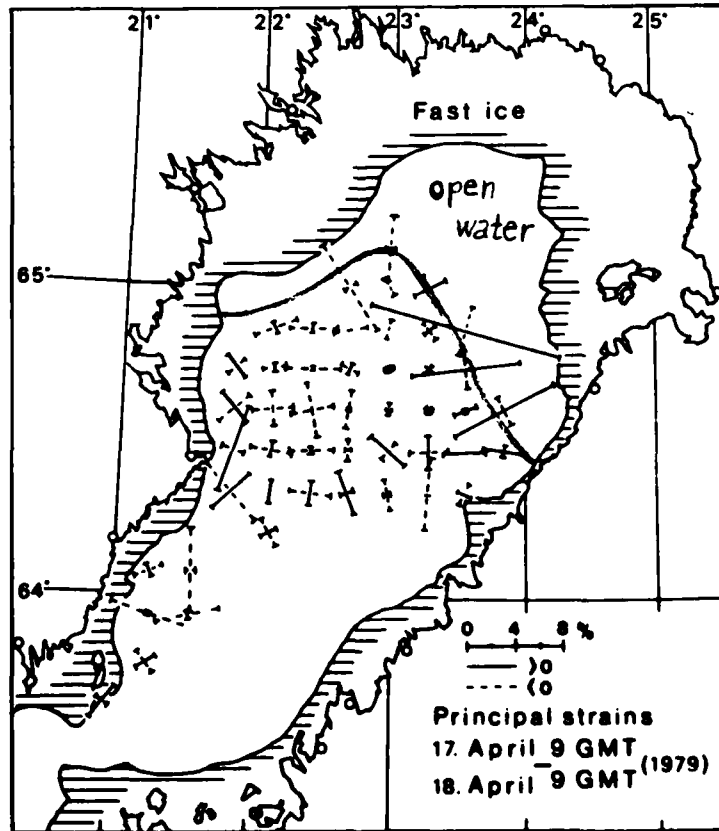


FIG. 8.

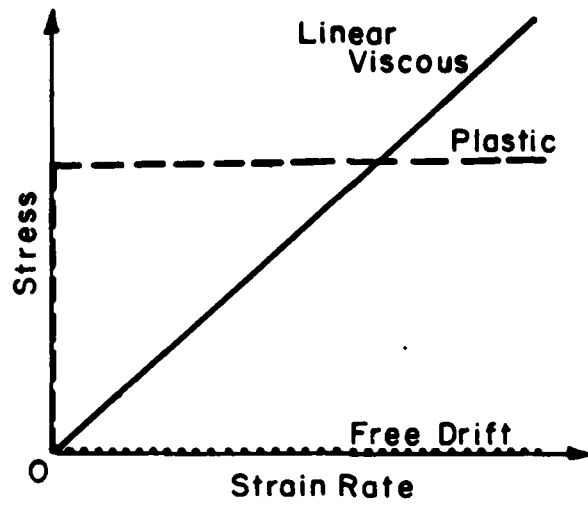


FIG. 9.

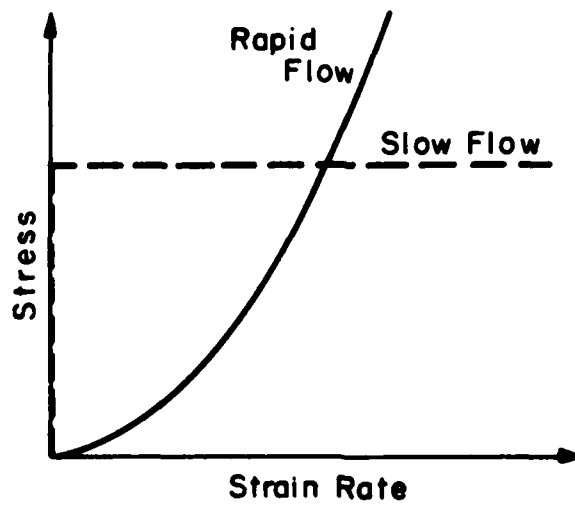


FIG. 10.

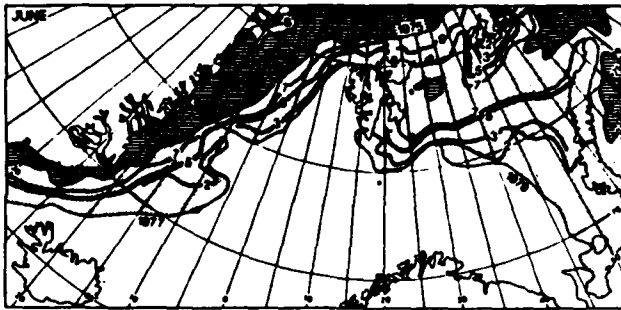


FIG. 11.

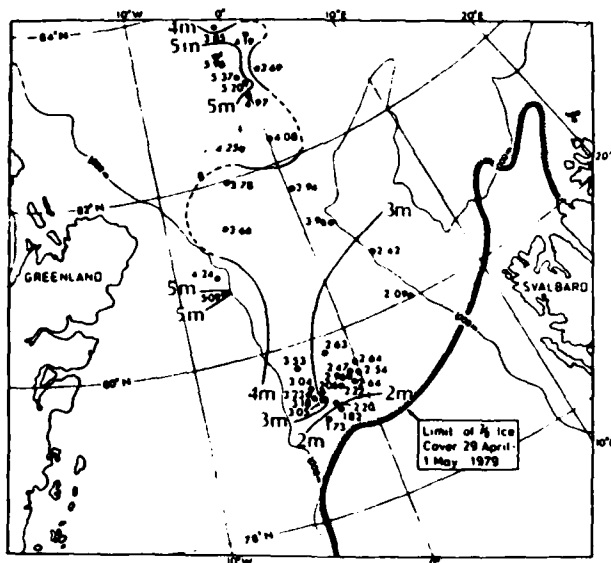


FIG. 12.

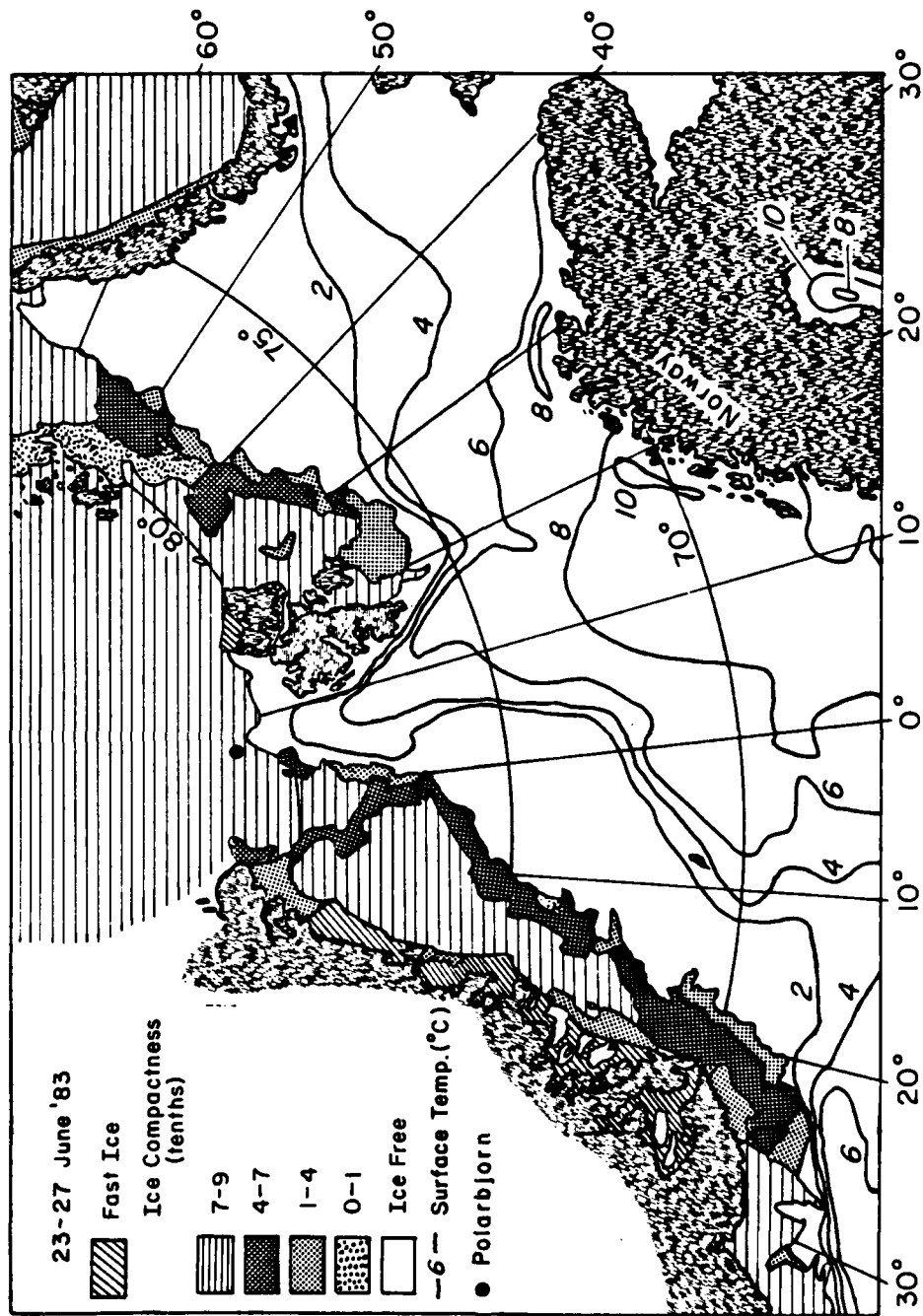


FIG. 13.

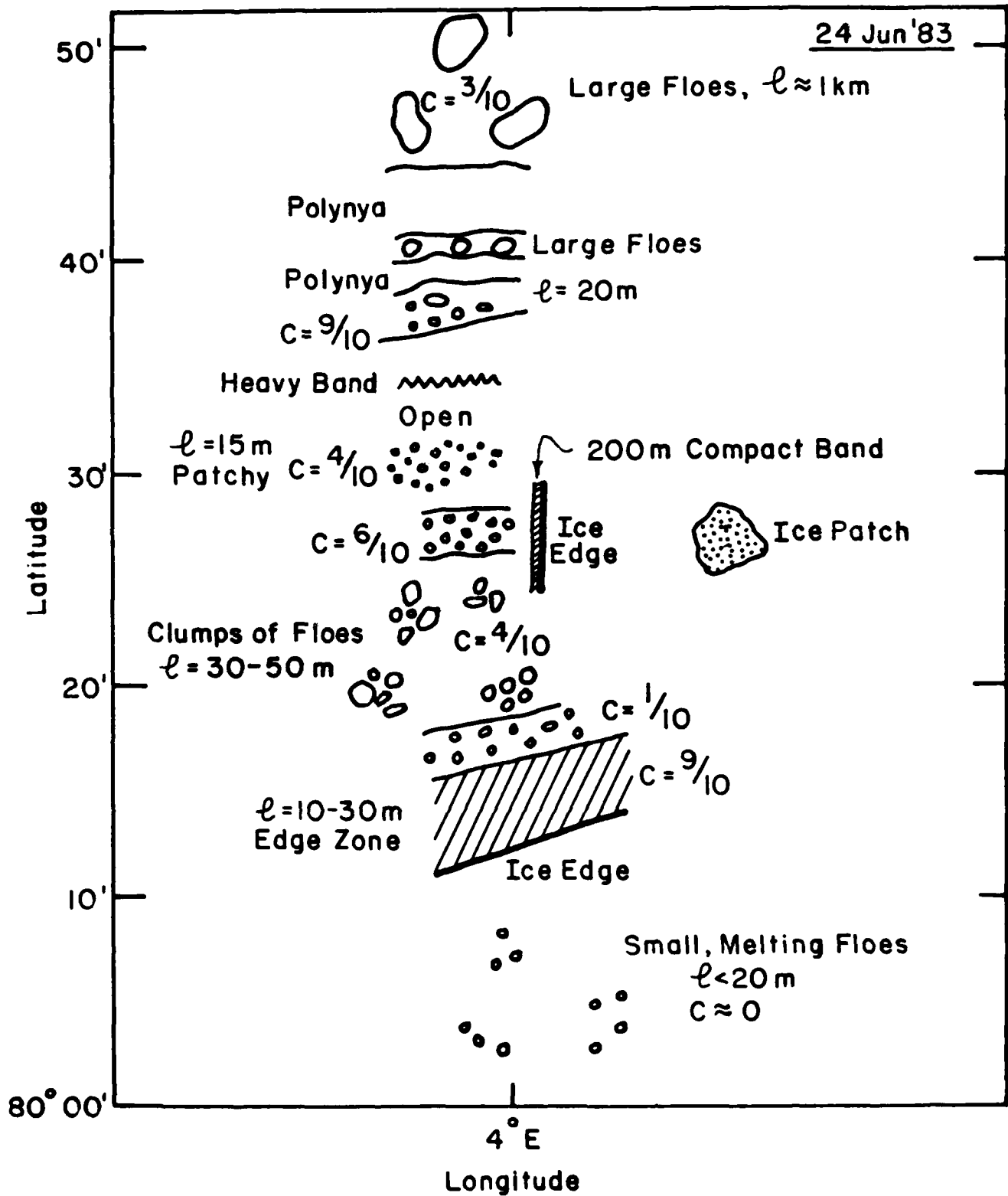


FIG. 14.

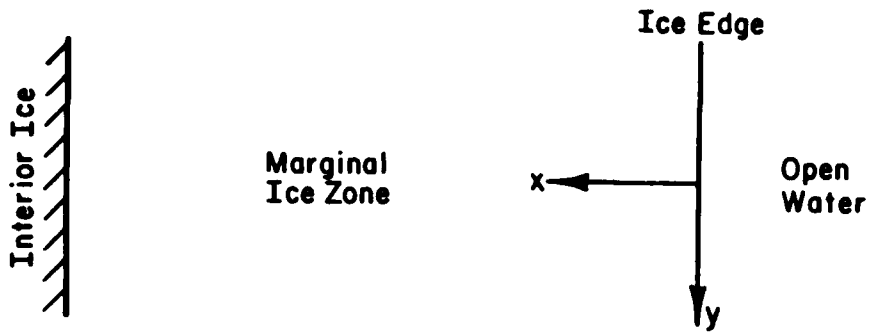


FIG. 15.

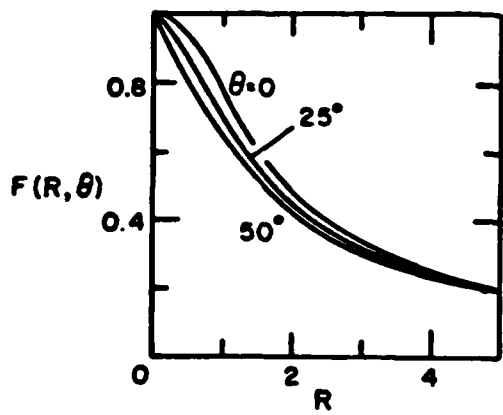


FIG. 16.

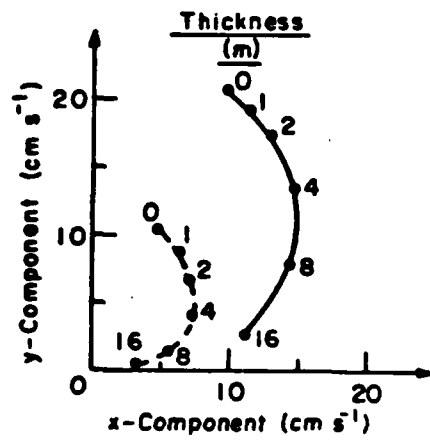


FIG. 17.

INITIAL COMPACTNESS 10.0 % SPACING RANDOM.

TIME STEP = 100. COMPACTNESS = 8.2 %.

INITIAL COMPACTNESS 50.0 % SPACING RANDOM.

TIME STEP = 100. COMPACTNESS = 47.3 %.

INITIAL COMPACTNESS 80.0 % SPACING RANDOM.

TIME STEP = 100. COMPACTNESS = 71.7 %.

INITIAL COMPACTNESS 90.0 % SPACING RANDOM.

TIME STEP = 100. COMPACTNESS = 64.3 %.

FIG. 18.

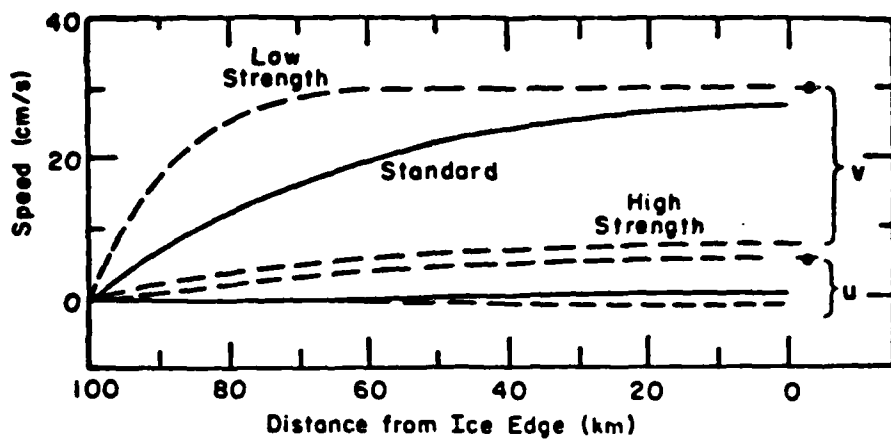


FIG. 19.

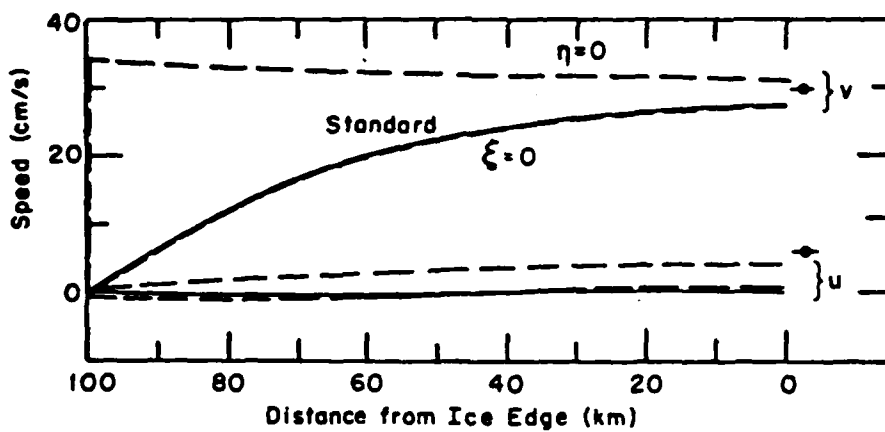


FIG. 20.

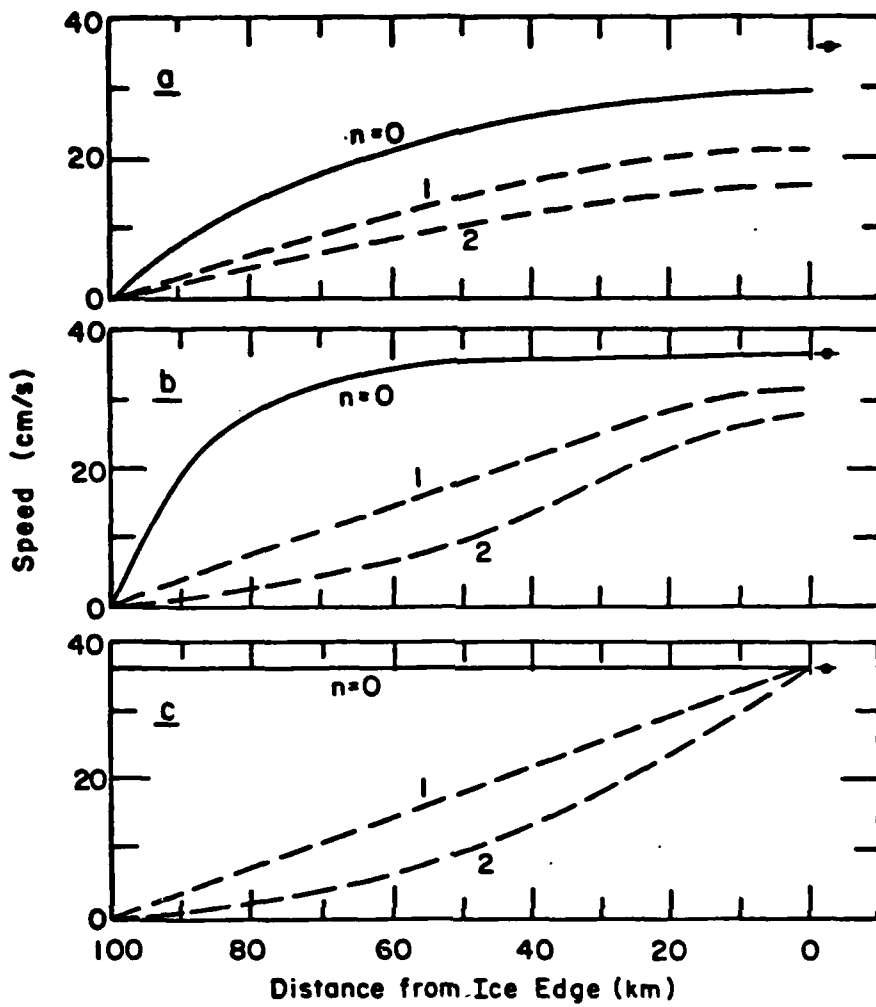


FIG. 21.

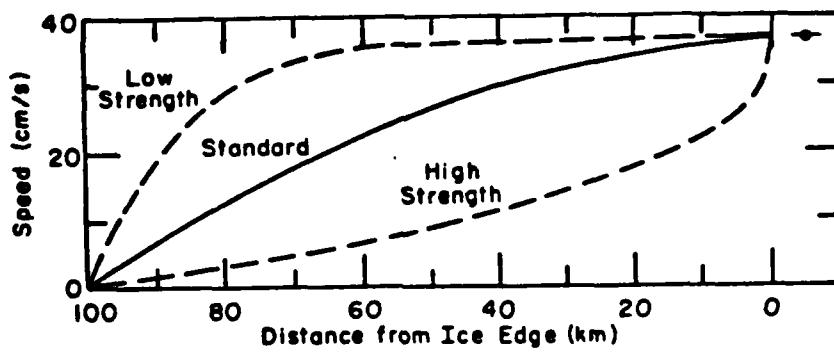


FIG. 22.

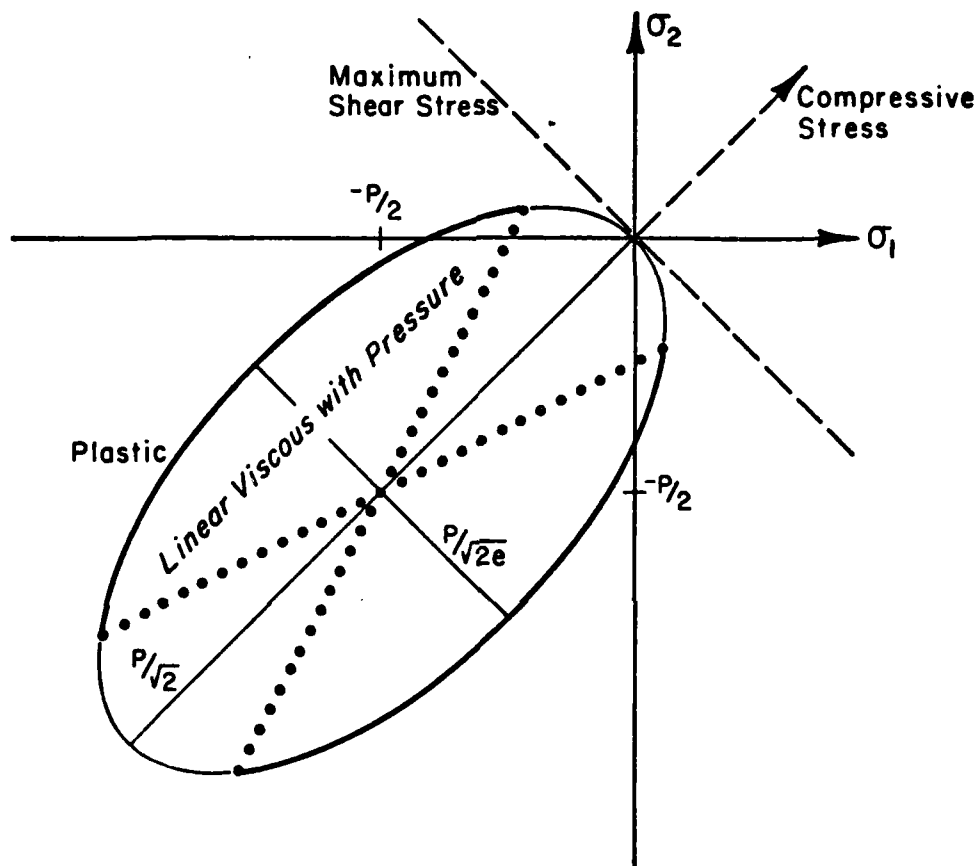


FIG. 23.

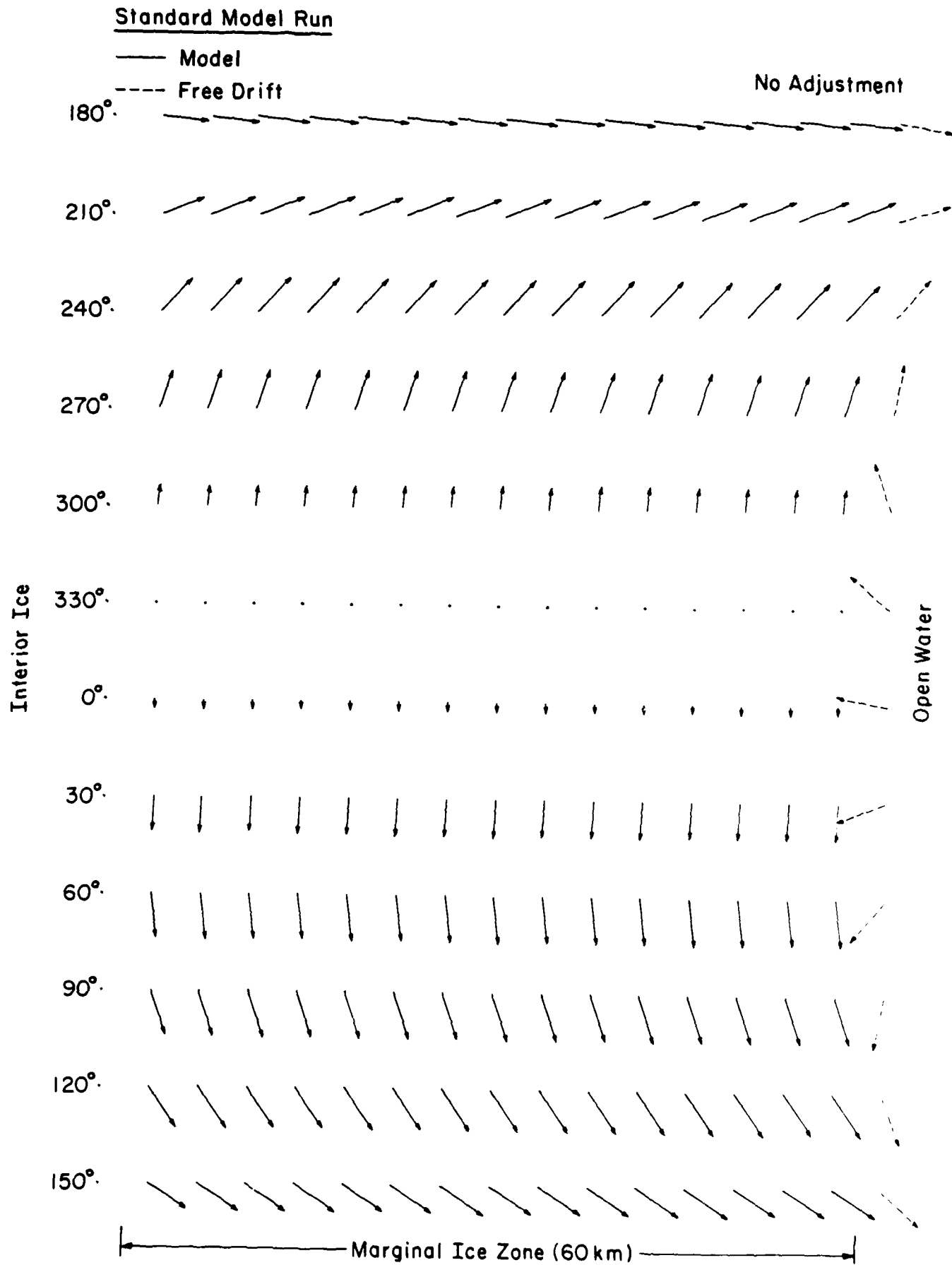


FIG. 24.

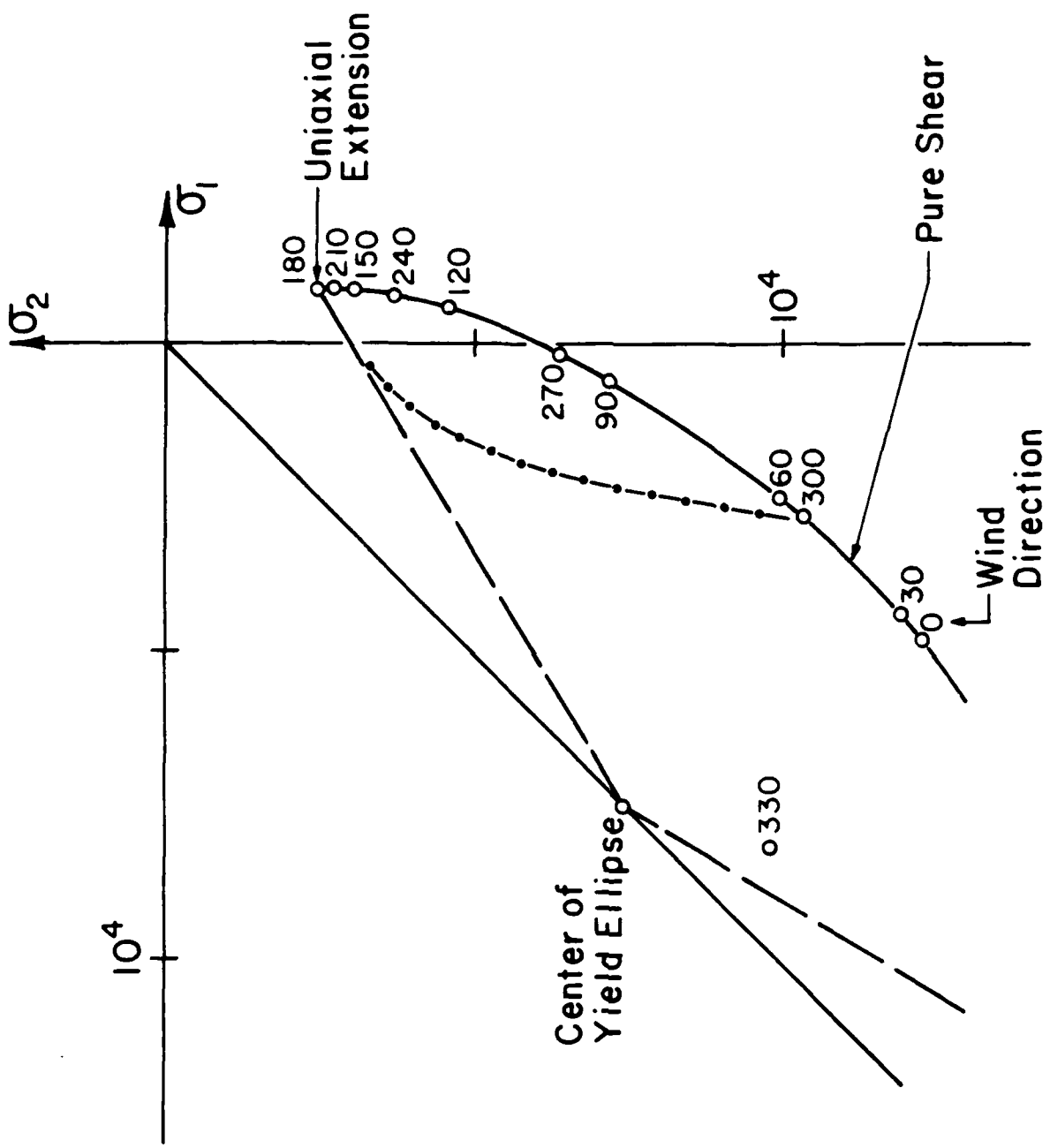


FIG. 25.

Standard Model Run

— Model
- - - Free Drift

With Adjustment (time = 48 hrs)

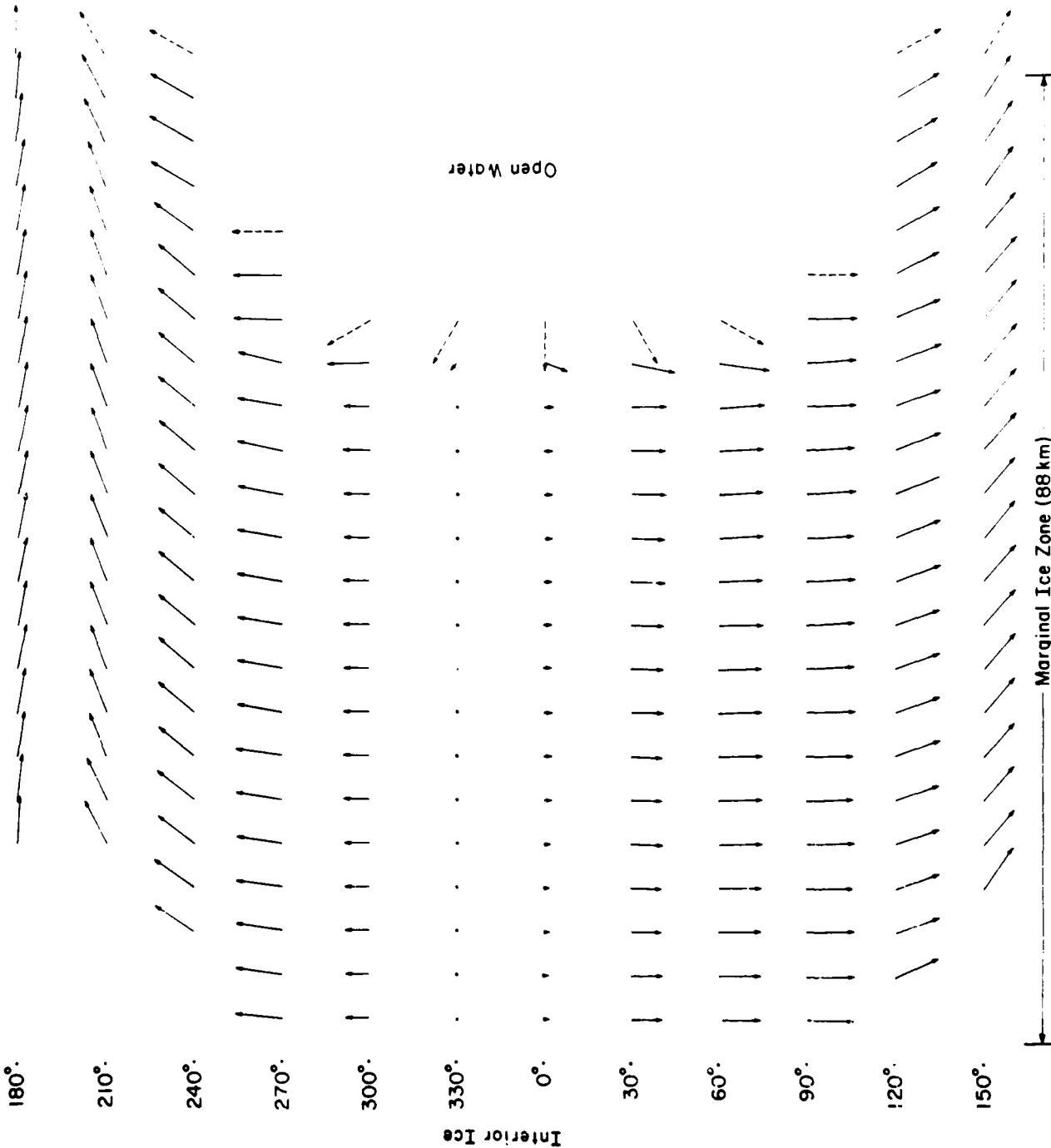


FIG. 26.

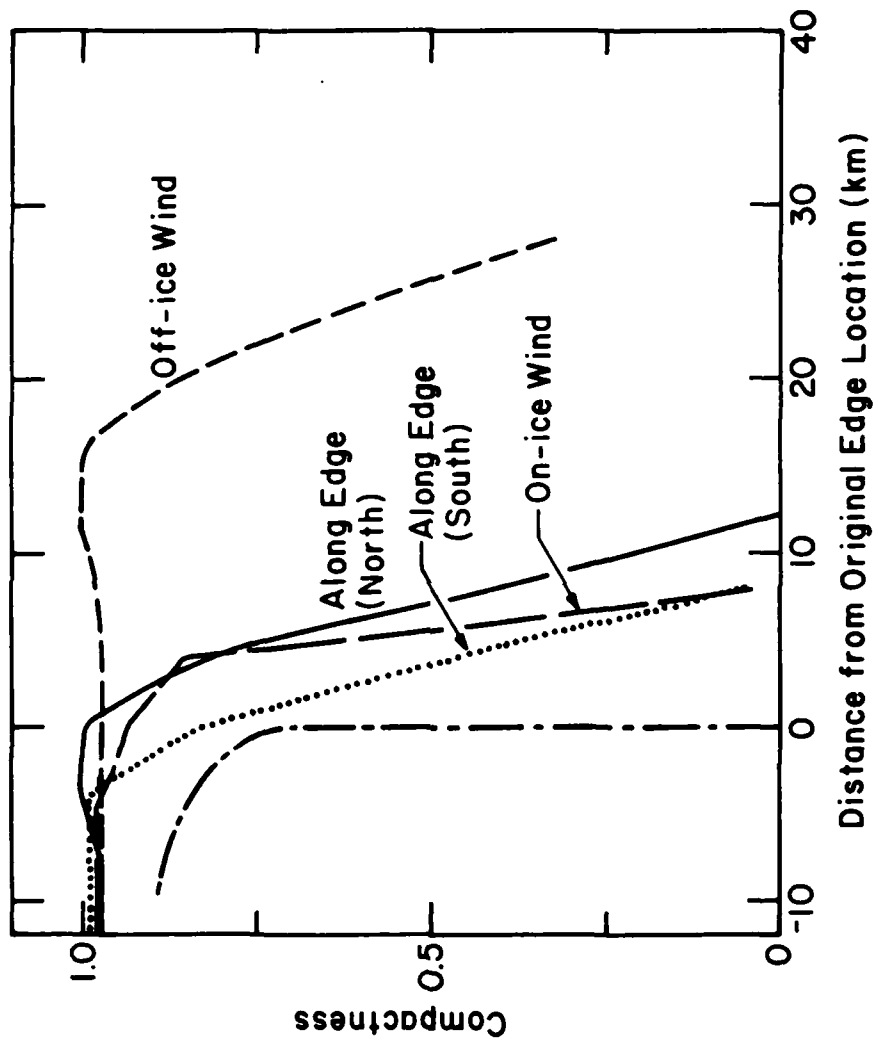


FIG. 27.

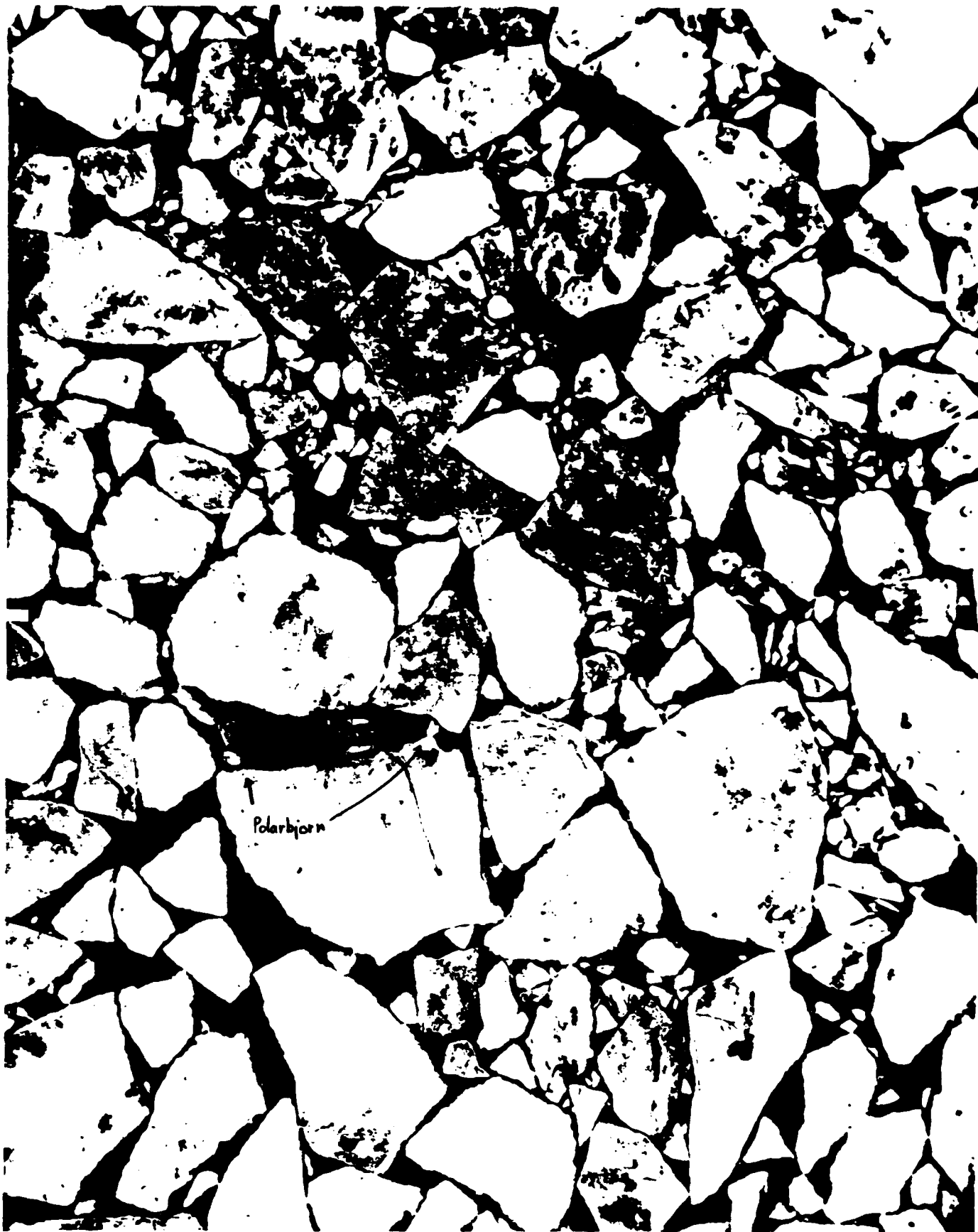


FIG. 28.

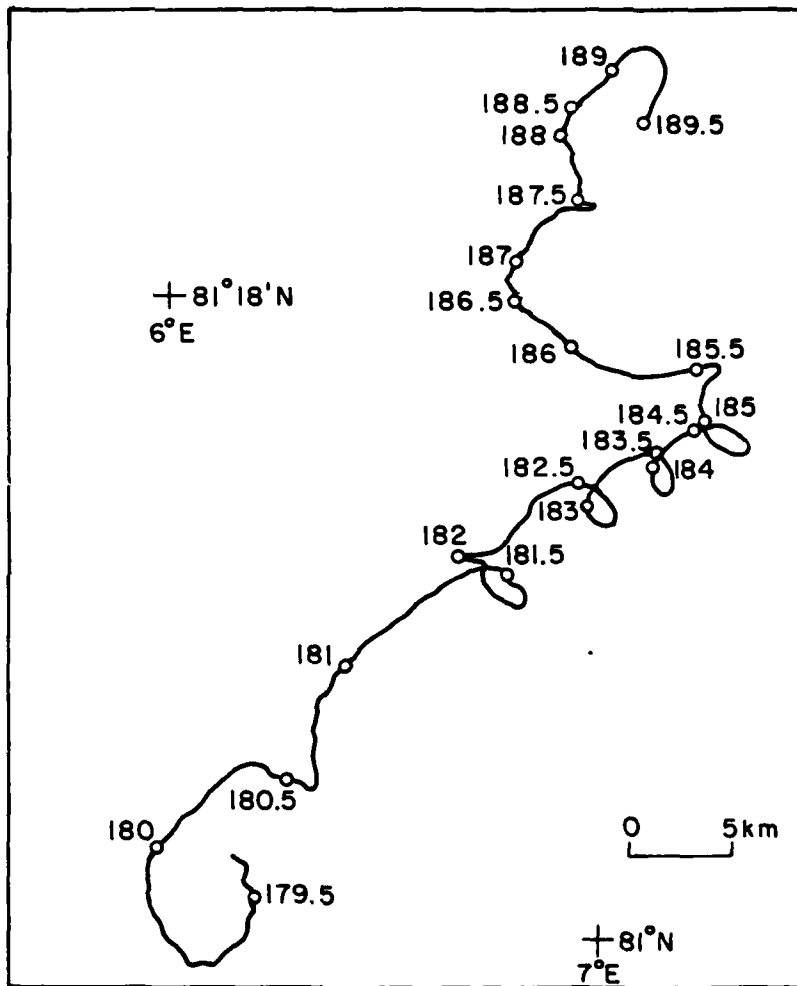


FIG. 29.

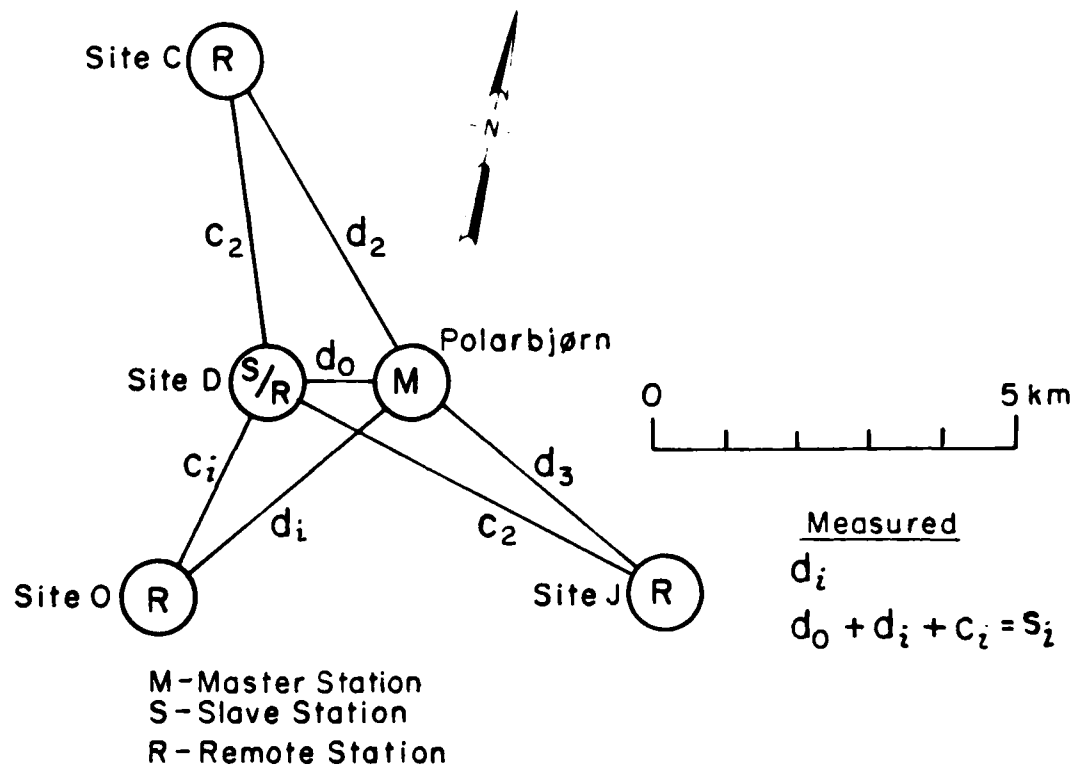


FIG. 30.

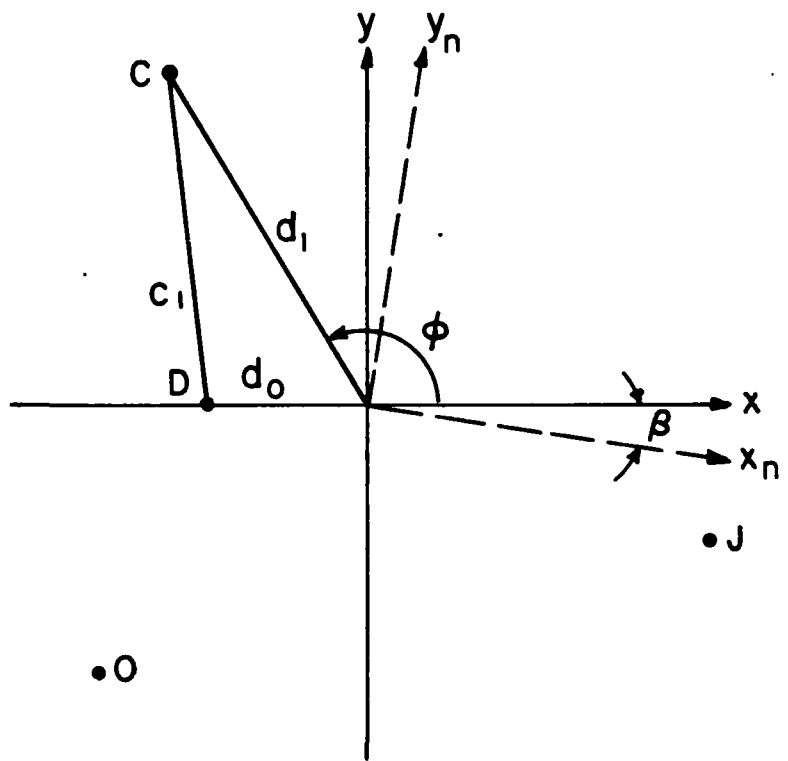


FIG. 31.

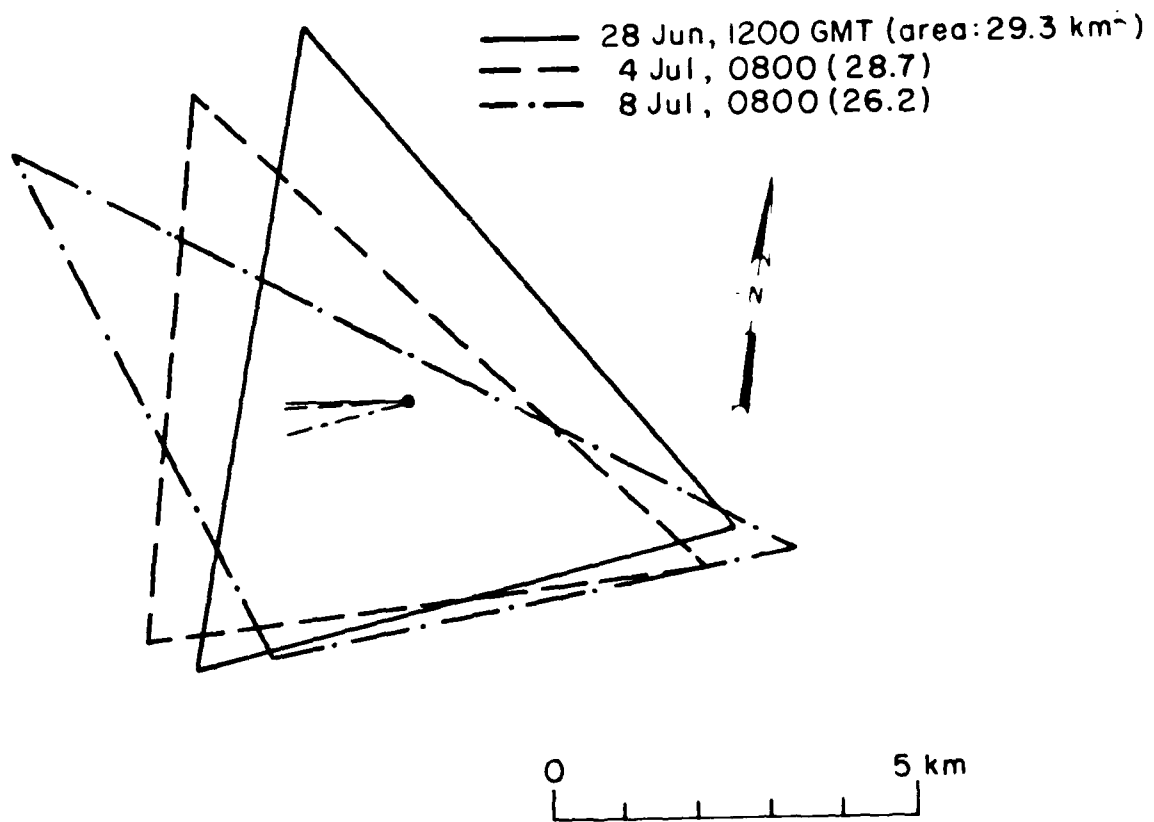


FIG. 32.

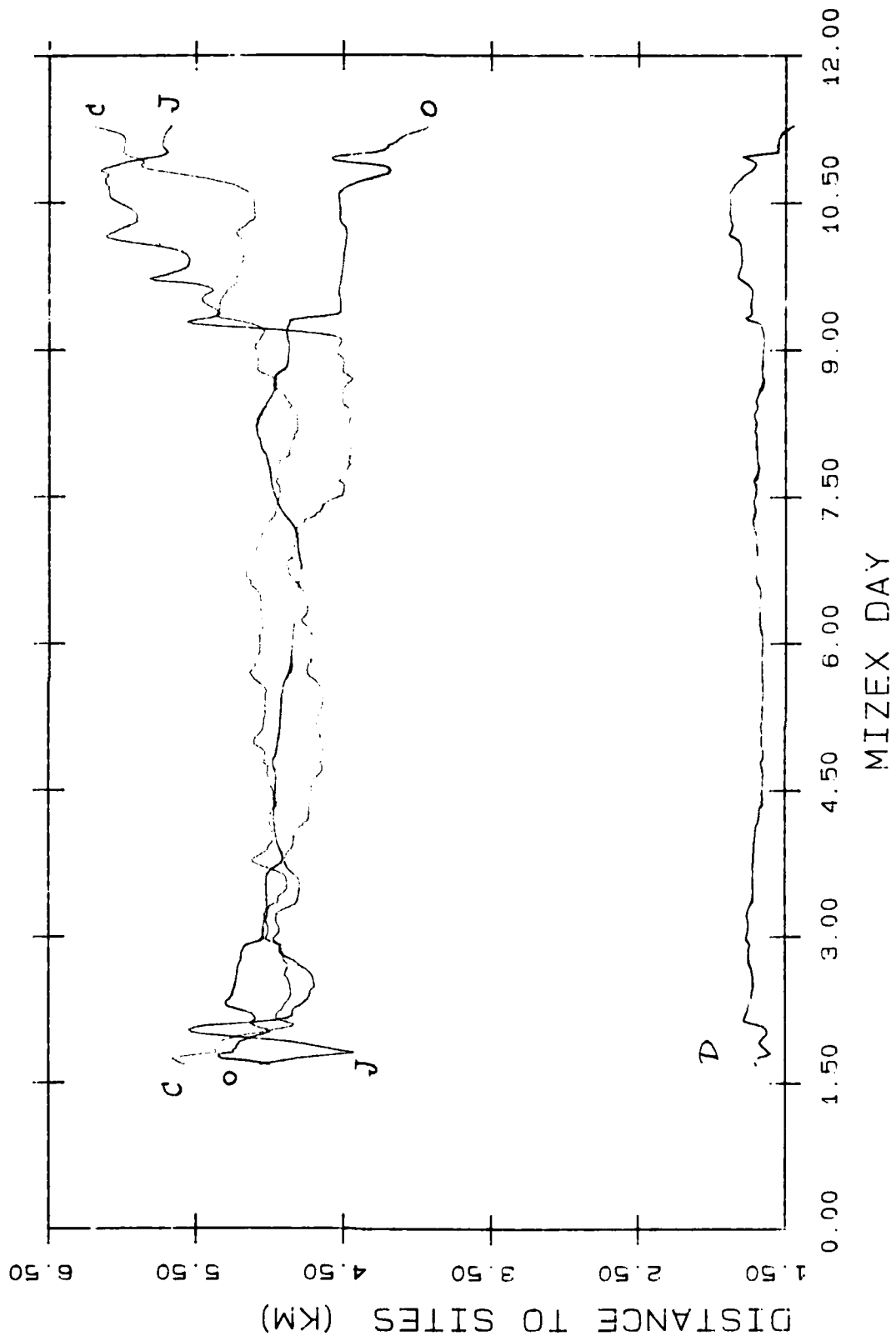


FIG. 33.

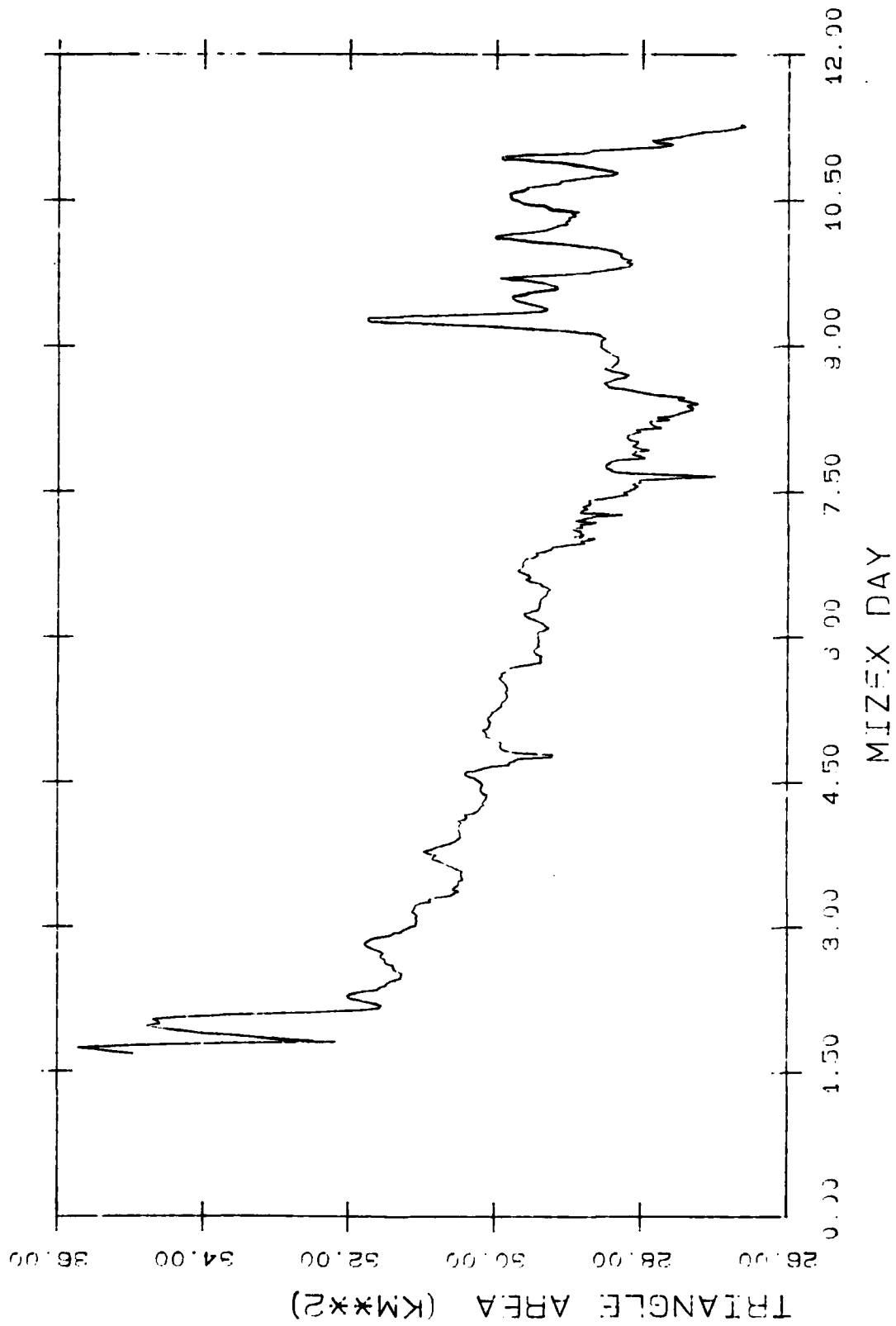


FIG. 34.

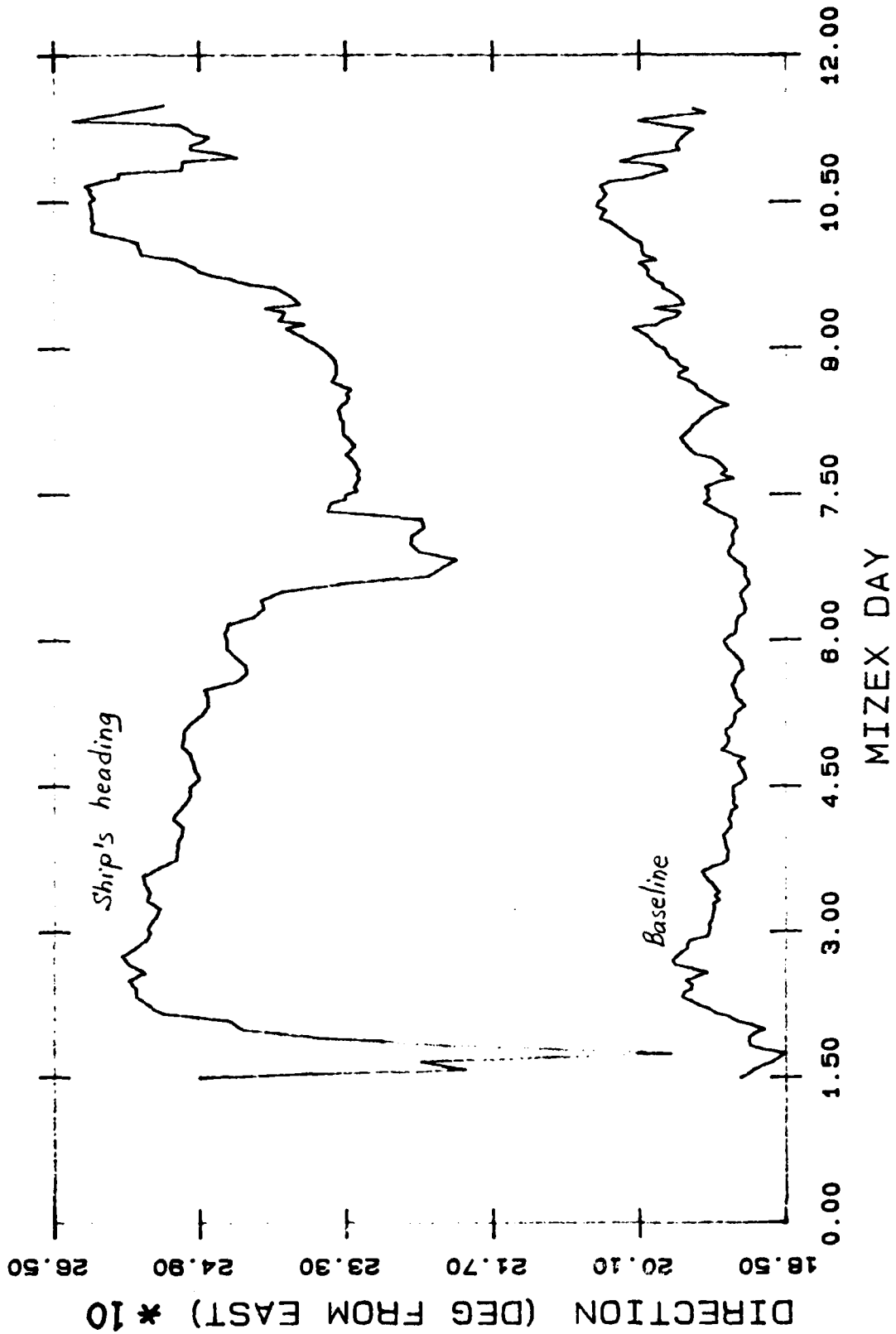


FIG. 35.

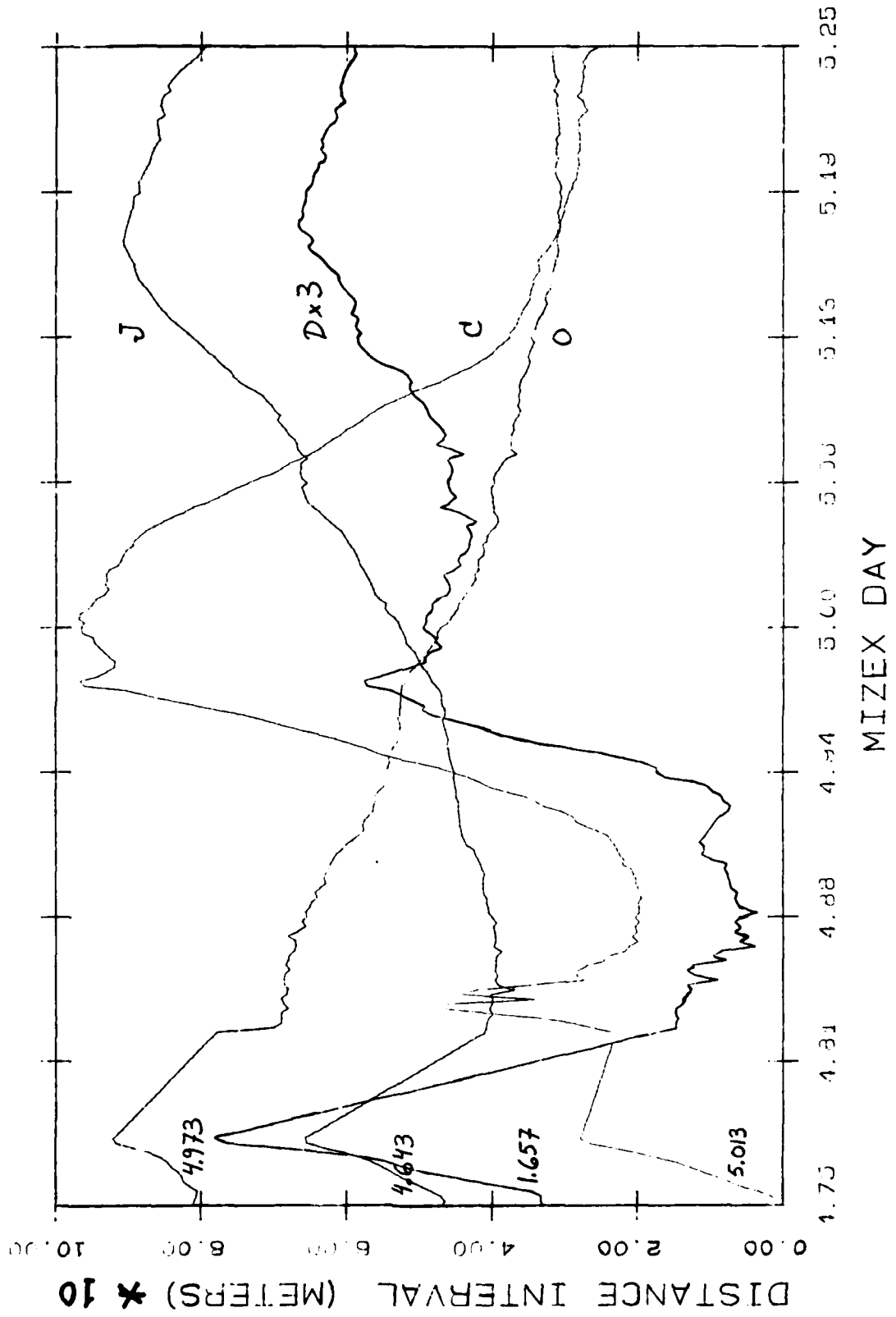


FIG. 36.

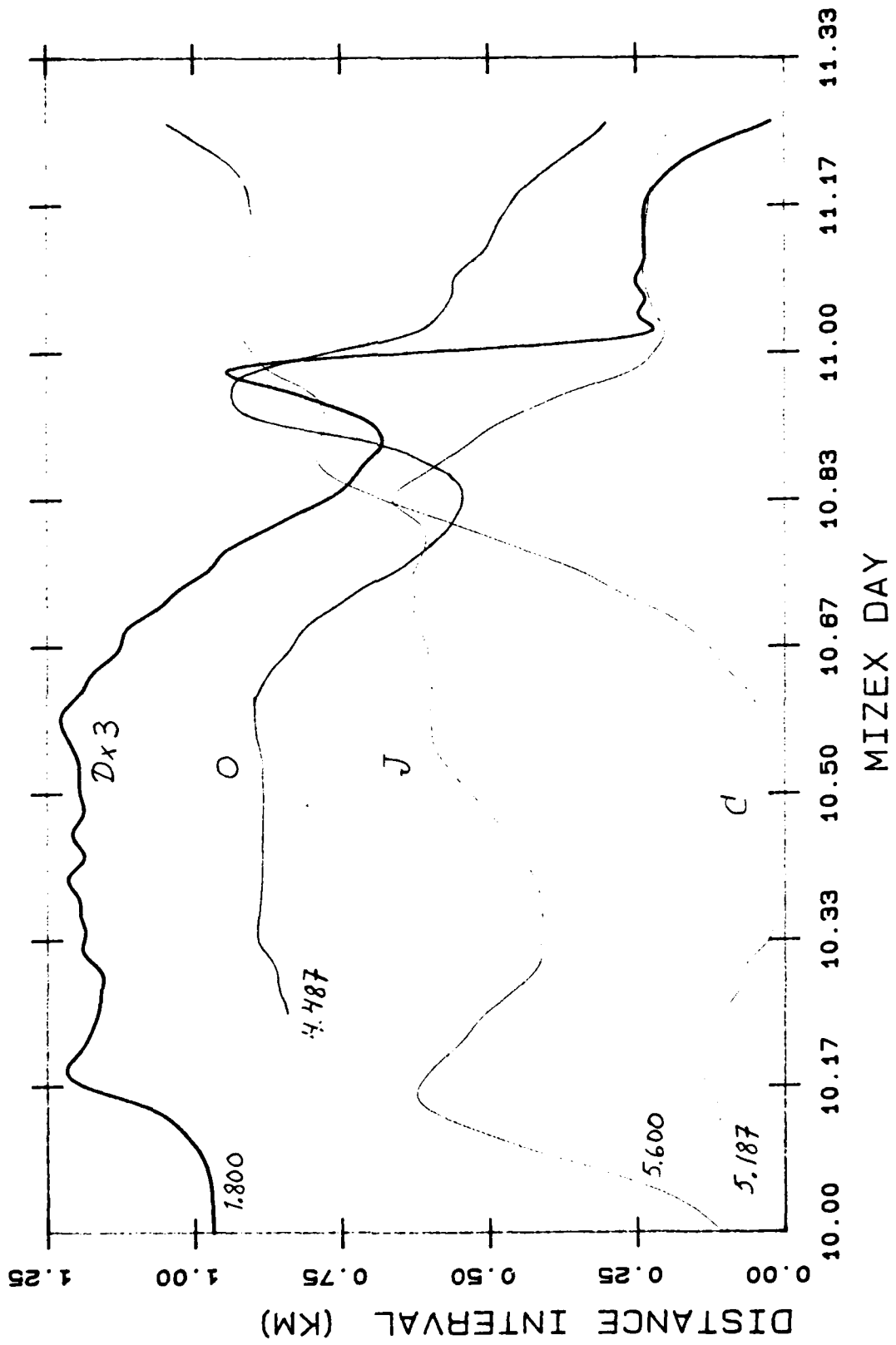


FIG. 37.

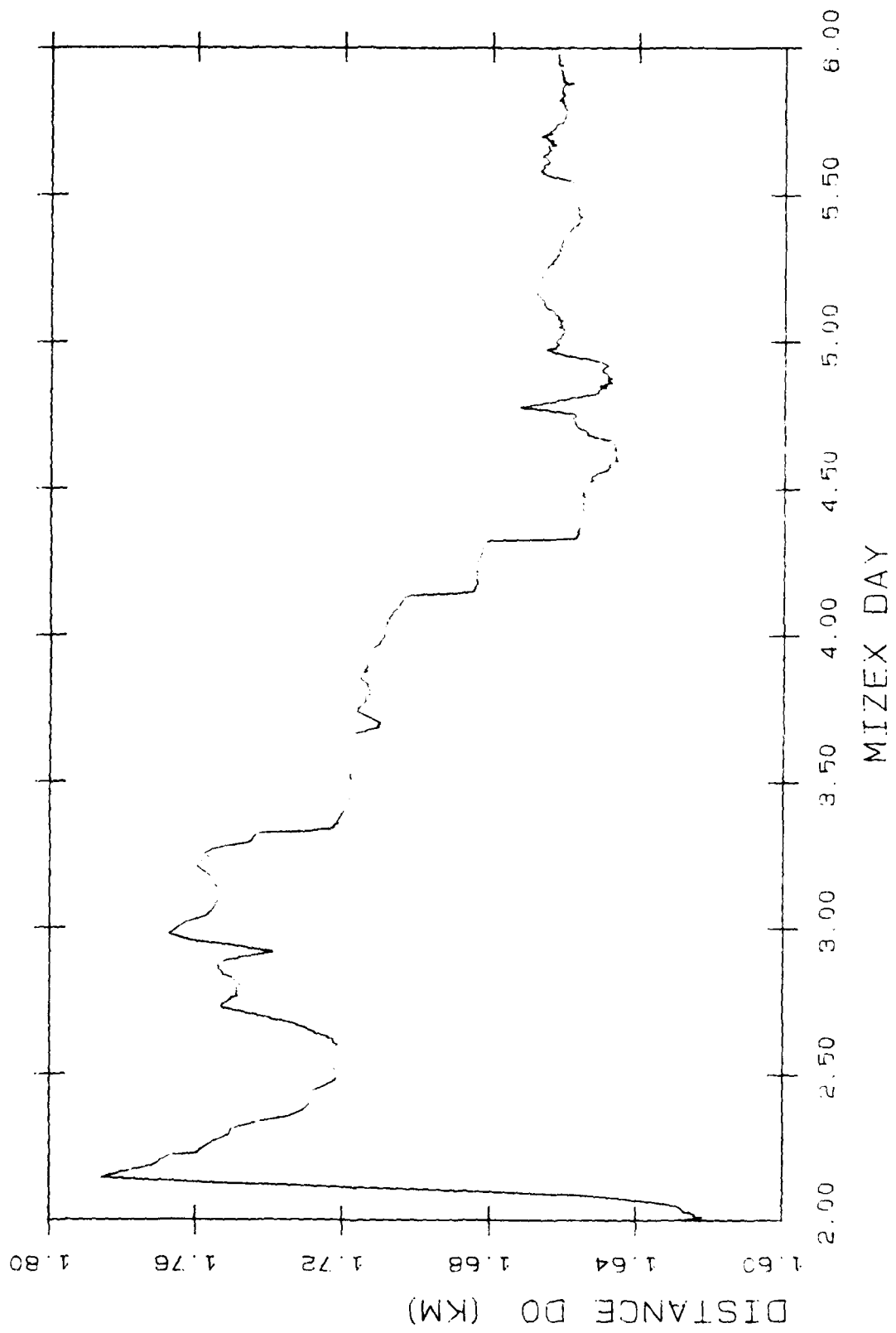


FIG. 38.

AD-A138 558

INVESTIGATION OF ICE DYNAMICS IN THE MARGINAL ZONE(U)
MARINE RESEARCH INST HELSINKI (FINLAND)
M LEPPAERANTA ET AL. DEC 83 DAJA45-B3-C-0034

2/2

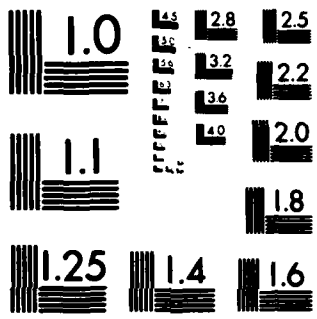
UNCLASSIFIED

F/G 8/12

NL



END
DATE
FORMED
4 84
DTIC



MICROCOPY RESOLUTION TEST CHART
NATIONAL BUREAU OF STANDARDS-1963-A

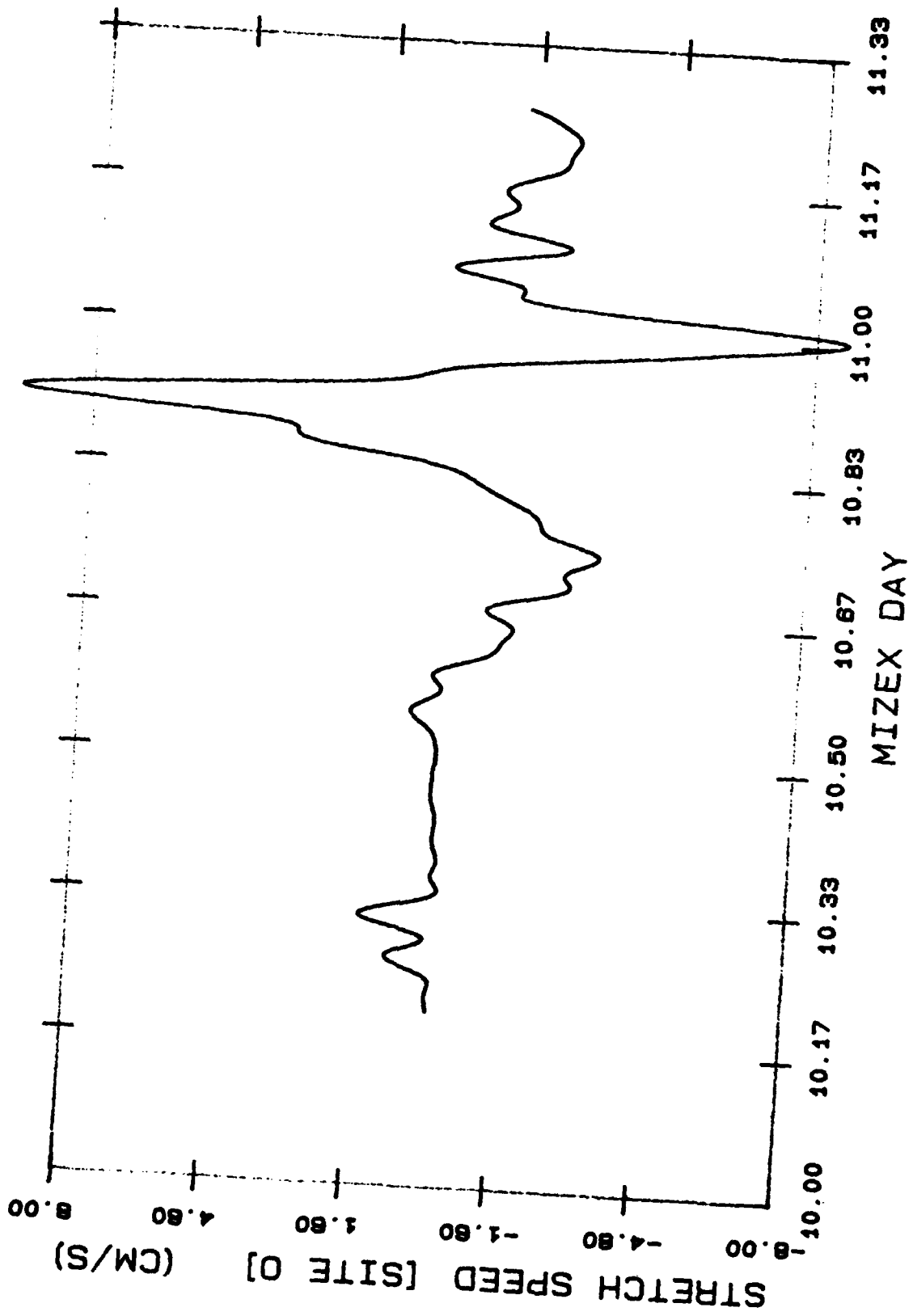


FIG. 39.a)

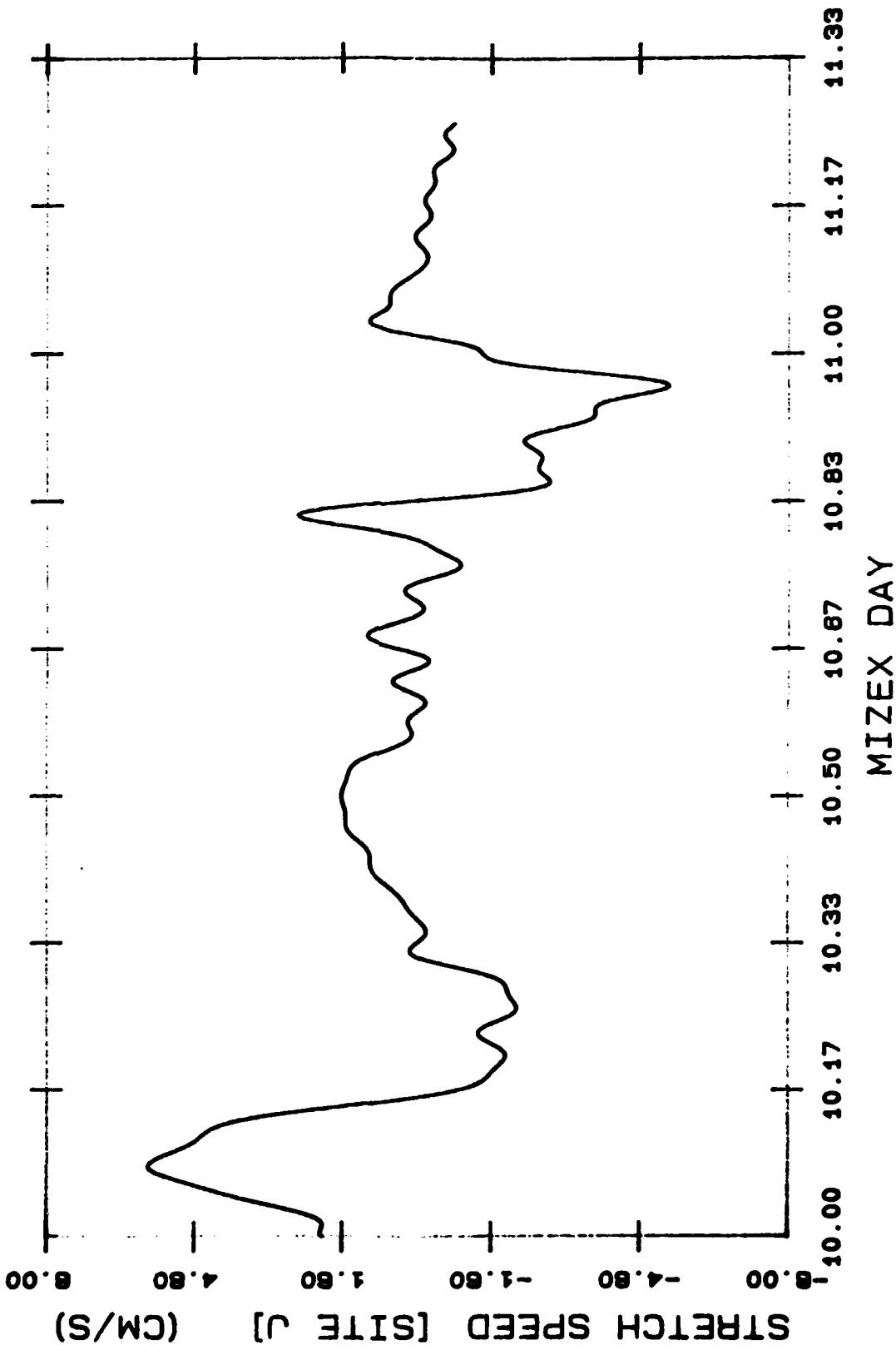
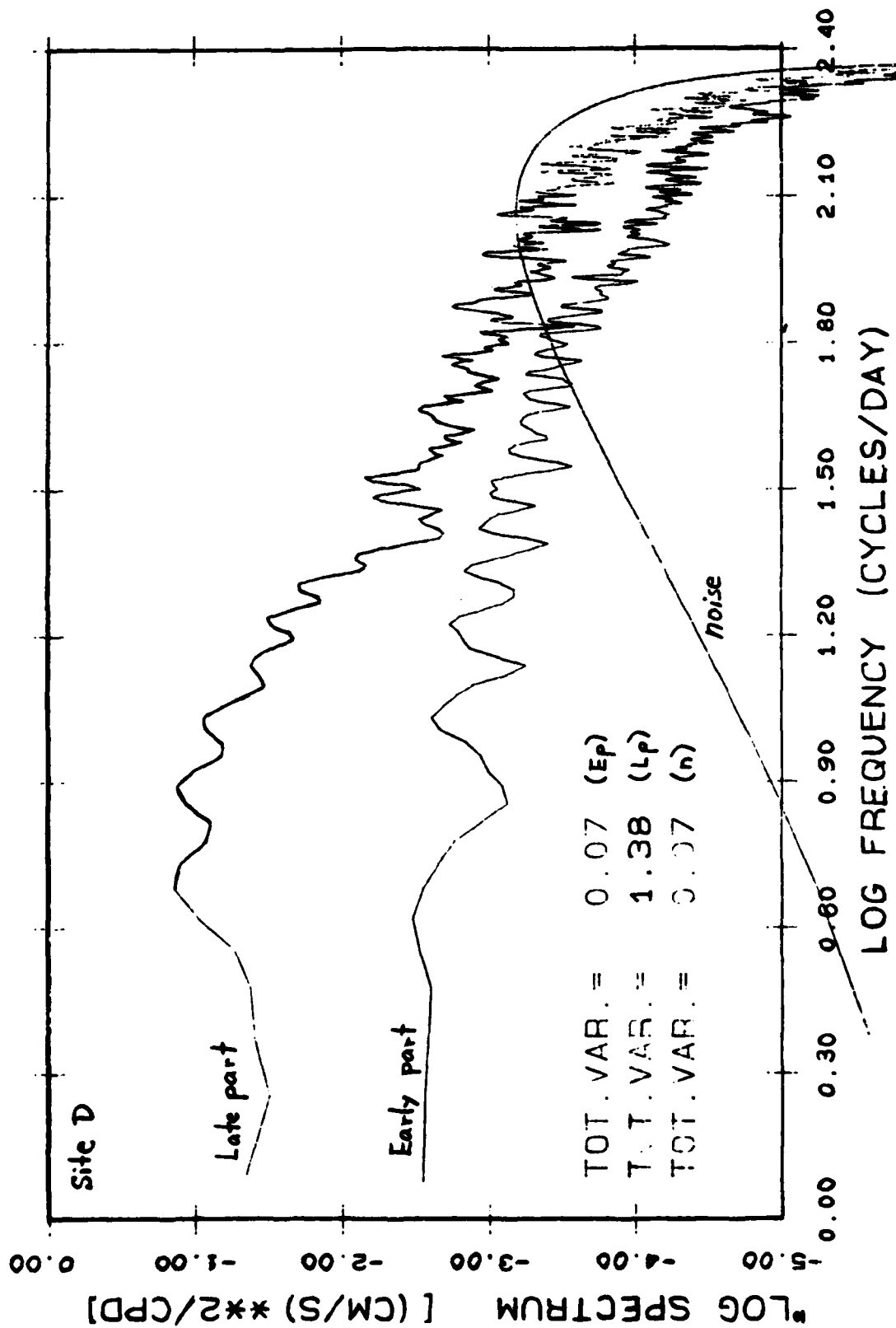


FIG. 39.6)



(a) 90.46

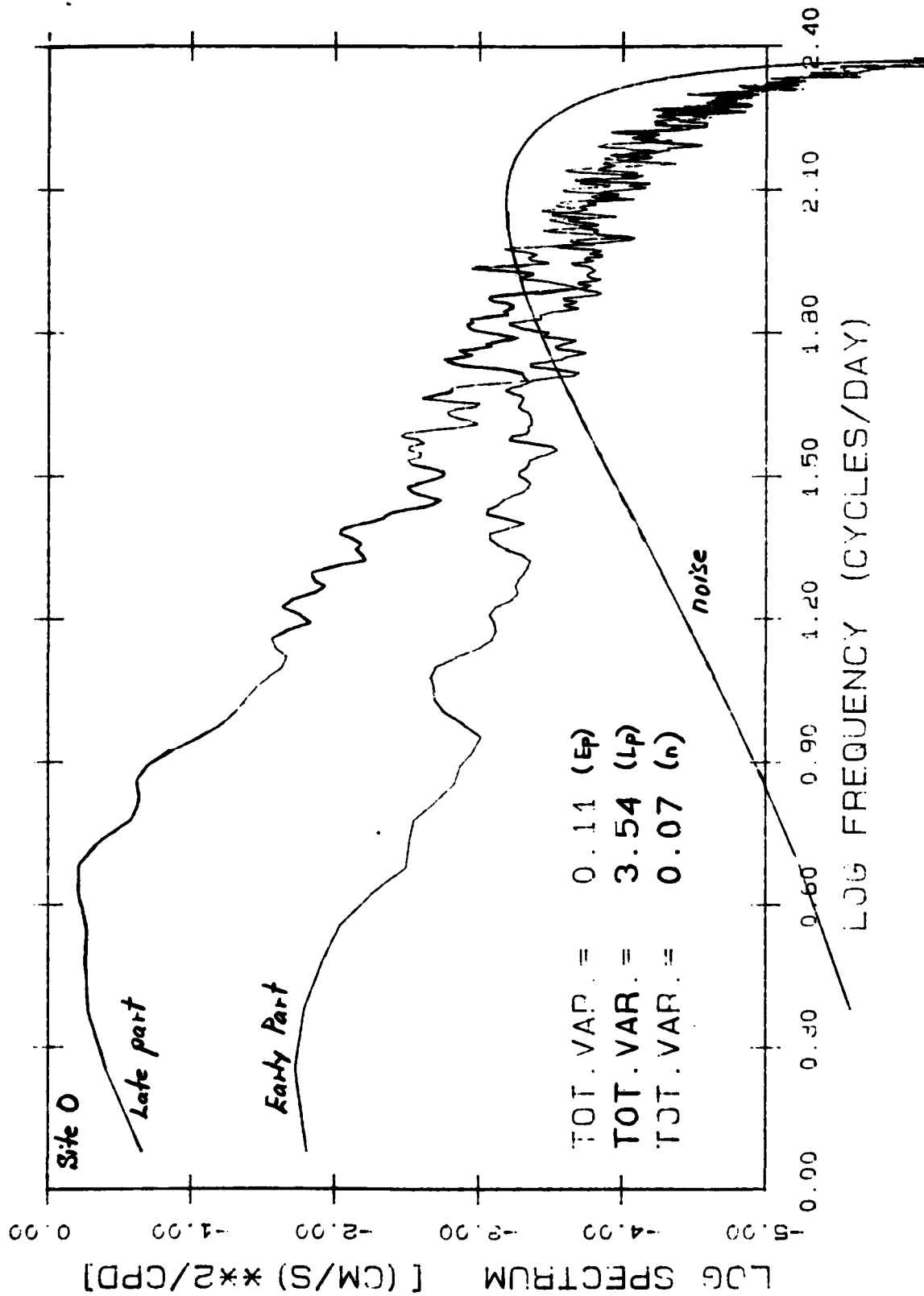


FIG 40.4

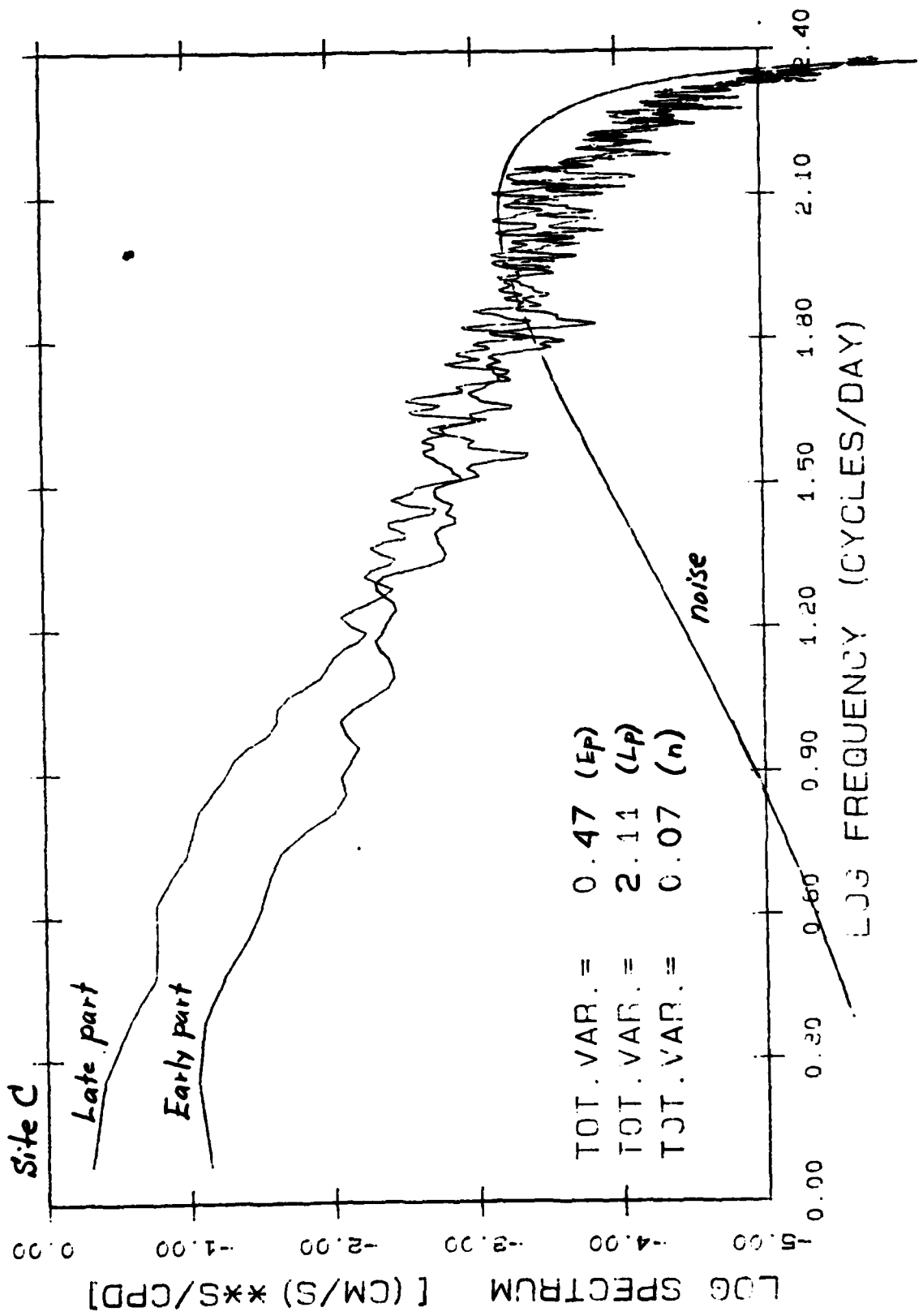


FIG. 40.4

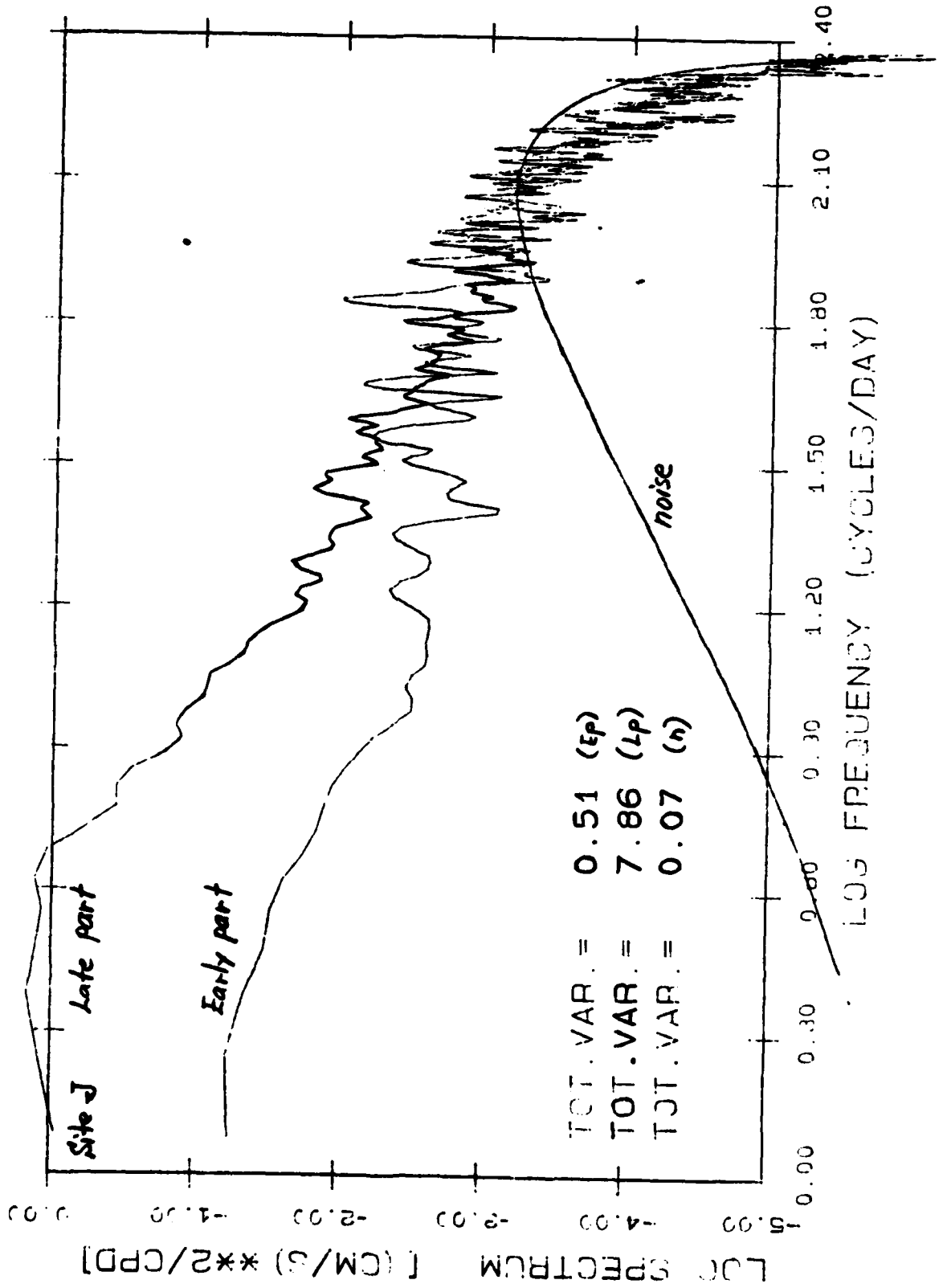


Fig. 40.4

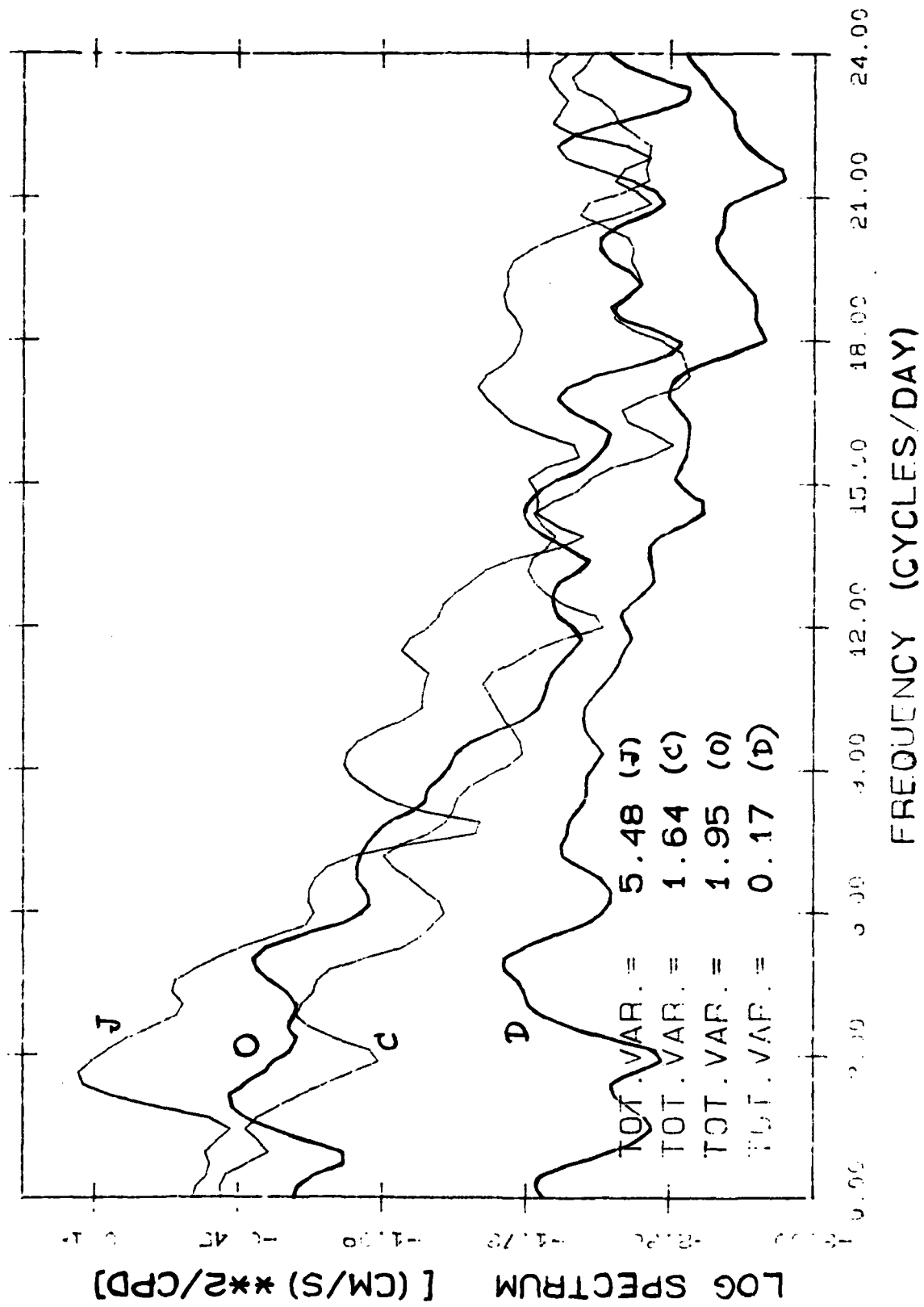


FIG. 41

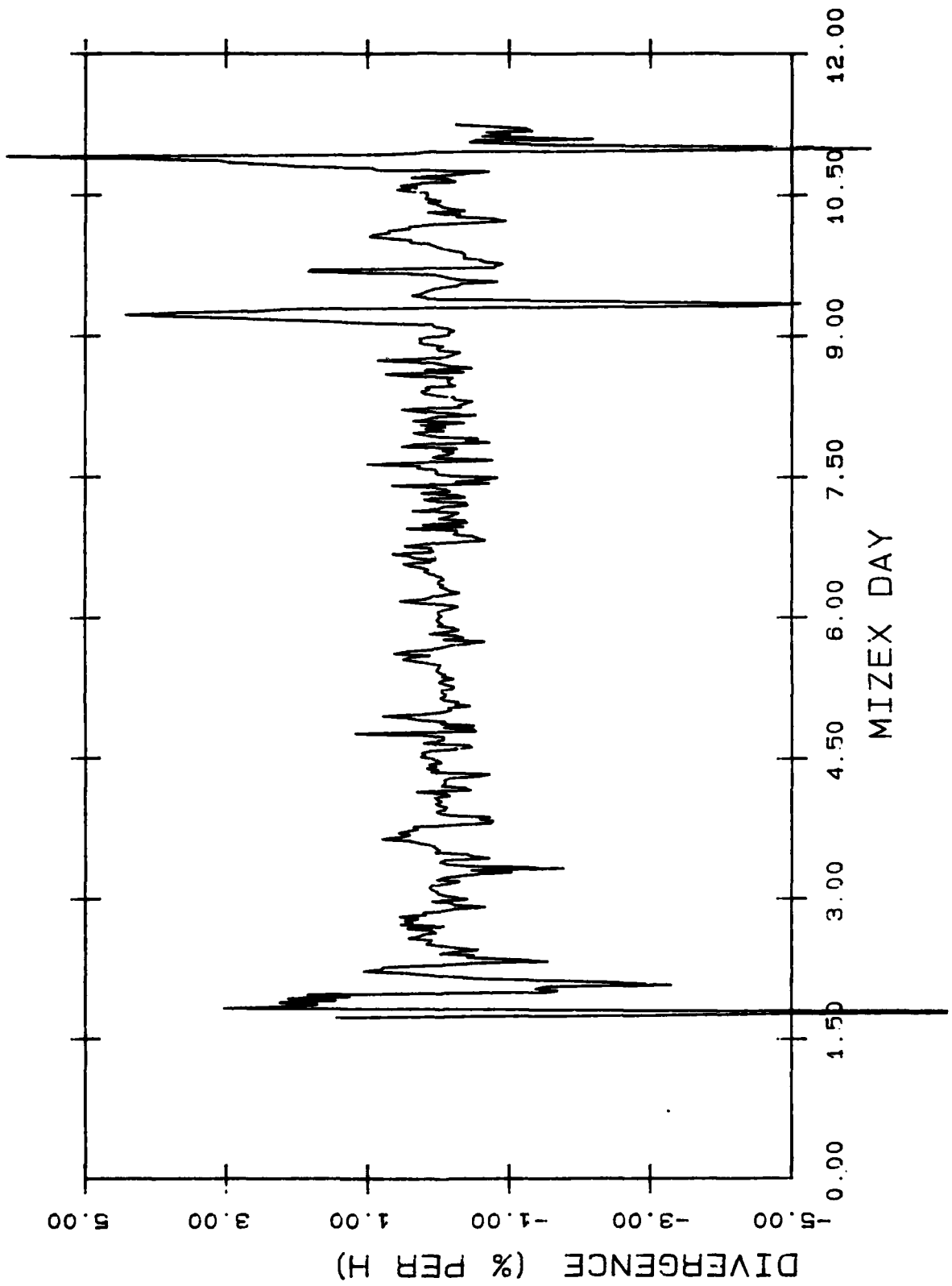


FIG. 42.a)

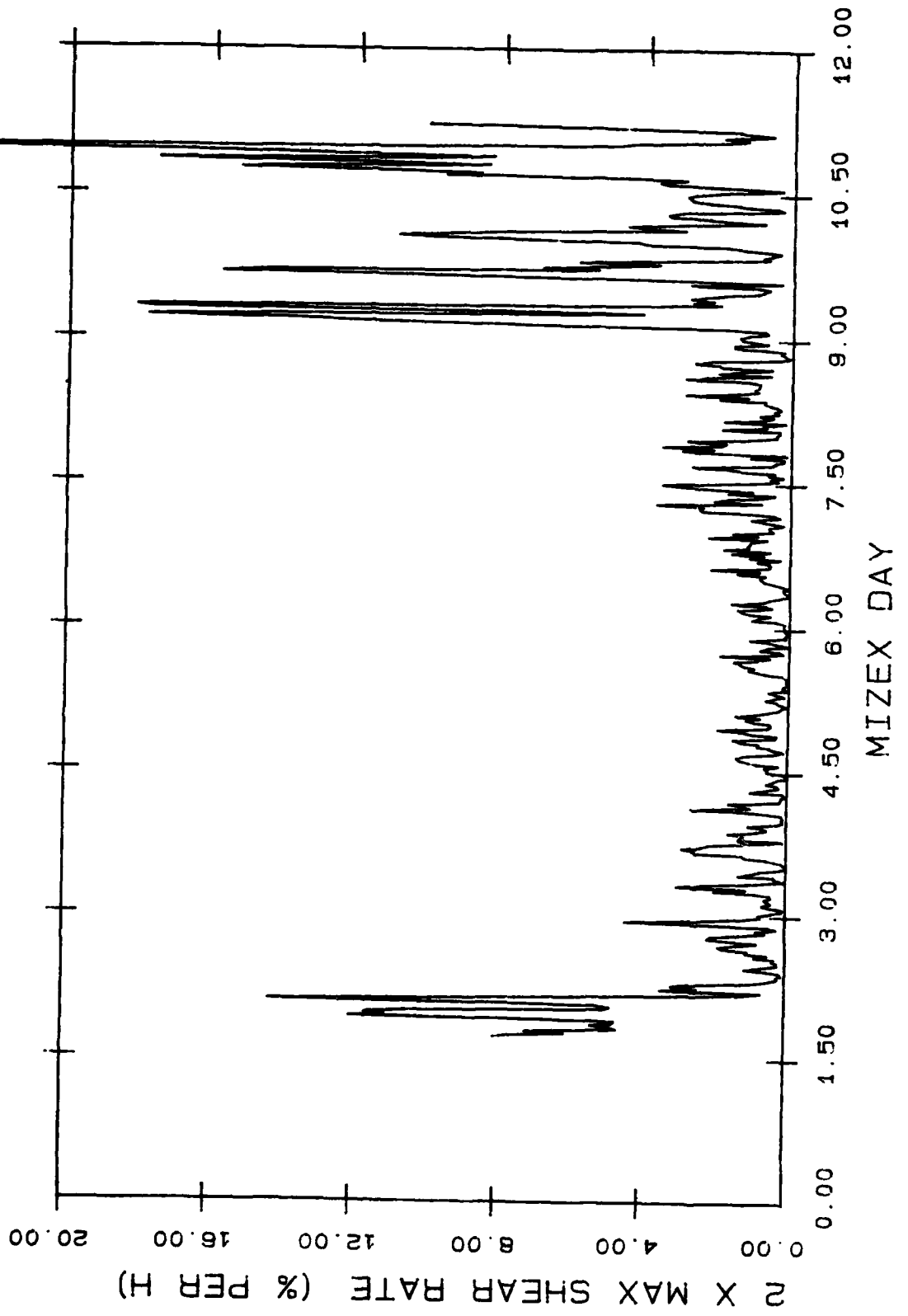


FIG. 42.6)

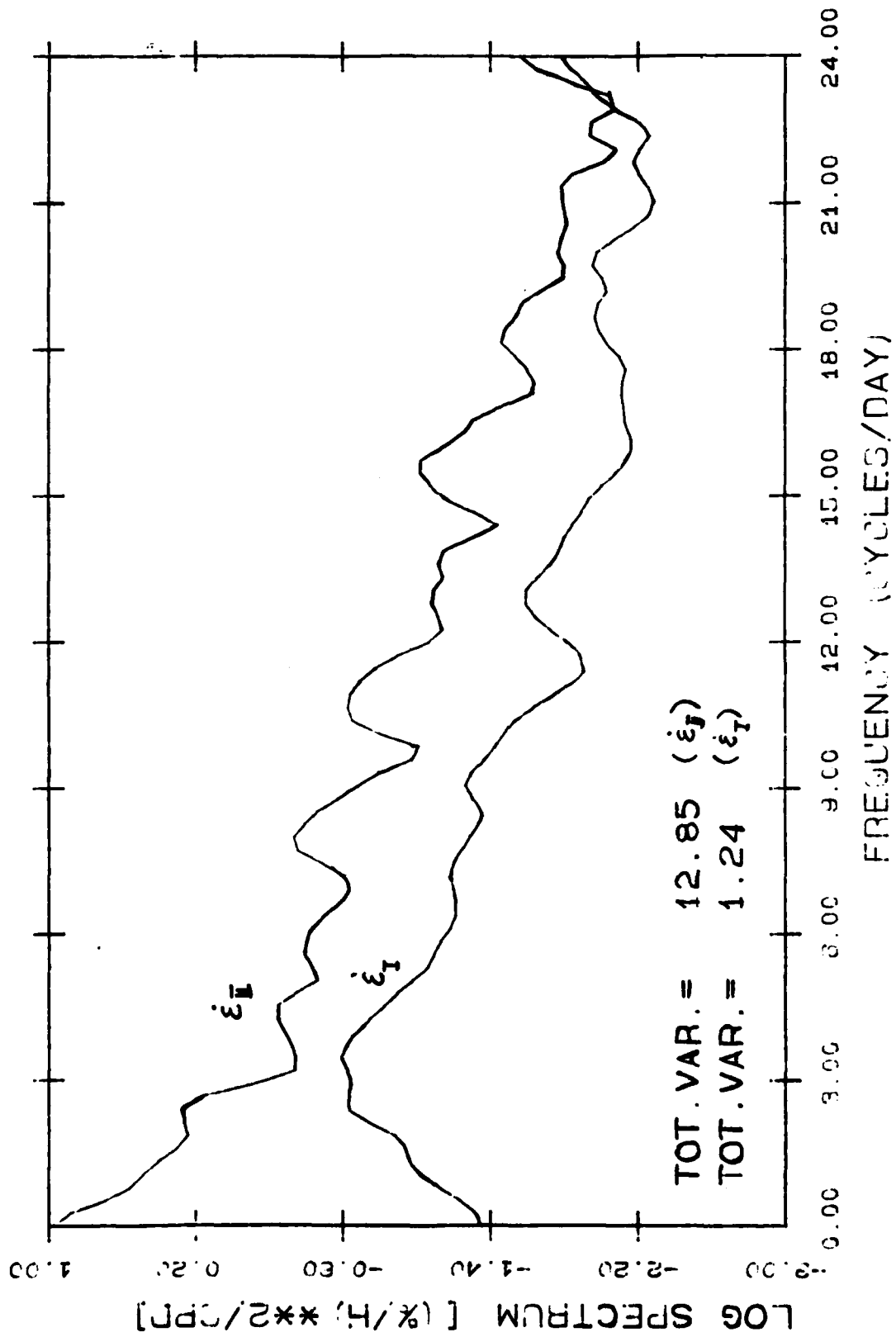


FIG. 43.

DATE
ILME